NASA TECHNICAL NOTE

NASA TN D-2867

CONVECTIVE AND EQUILIBRIUM RADIATION HEAT-TRANSFER PREDICTIONS FOR PROJECT FIRE REENTRY VEHICLE

by P. Calvin Stainback

Langley Research Center
Langley Station, Hampton, Va.

NATIONAL AERONAUTICS AND SPACE ADMINISTRATION • WASHINGTON, D. C. • JULY 1965

NASA TN D-2867

CONVECTIVE AND EQUILIBRIUM RADIATION HEAT-TRANSFER PREDICTIONS FOR PROJECT FIRE REENTRY VEHICLE

By P. Calvin Stainback

Langley Research Center
Langley Station, Hampton, Va.

NATIONAL AERONAUTICS AND SPACE ADMINISTRATION

For sale by the Clearinghouse for Federal Scientific and Technical Information
Springfield, Virginia 22151 – Price $3.00

CONVECTIVE AND EQUILIBRIUM RADIATION HEAT-TRANSFER PREDICTIONS FOR PROJECT FIRE REENTRY VEHICLE

By P. Calvin Stainback
Langley Research Center

SUMMARY

Approximate equilibrium flow fields were calculated for the forebody of the Project Fire reentry vehicle at zero angle of attack for five points along the trajectory. These flow-field calculations were based on wind-tunnel pressure and shock-shape data and the assumption of a quadratic variation of pressure and velocity across the shock layer. The results of these calculations were ultimately used to calculate the equilibrium radiation heat-transfer rate to the forebody of the vehicle. Convective heating rates were also calculated by using the wind-tunnel pressure data.

INTRODUCTION

At the present time theoretical estimates for the heat-transfer rates to vehicles reentering the atmosphere at very high velocities are subject to rather large uncertainties. These uncertainties are particularly true of the component of heating due to radiation from the hot gas in the shock layer because of the lack of accurate radiation intensity data. One purpose of Project Fire is to measure the radiation heating rate (both total and spectral) and total heating rates (convective plus radiative minus reradiative) experienced by a body reentering the atmosphere at a velocity of 37,000 feet per second.

Since basic air radiation data can be greatly influenced by foreign particle contamination, the vehicle is designed to obtain radiation and total heating rates in a "clean" atmosphere. This design is accomplished by utilizing a multiple layer construction for the forebody, which will receive the majority of the heat load. Three metal (beryllium) calorimeters are used to insure a clean atmosphere for a suitable testing time. Two ablating heat shields, which can be removed at a selected time by an explosive mechanism, are interspaced between the calorimeters to protect them until the selected testing time is reached on the trajectory.

With sufficiently extensive and accurate flight data, it should be possible to evaluate the various theories for calculating convective heating rates and the various radiation intensity data. The purpose of the present report is to present approximate equilibrium flow fields and the resultant heat-transfer

calculations for the Project Fire reentry vehicle at several points along its proposed trajectory. The results of these simplified calculations are compared with the results of more exact calculations to determine if the relatively simple analysis can provide heating estimates of usable accuracy.

SYMBOLS

A	area
a_1, a_2, a_3	constants in eq. (1)
b_1, b_2, b_3	constants in eq. (2)
c_1, c_2, c_3	constants in eq. (2)
C_D	drag coefficient
$\bar{h}$	altitude
h, k, l	coordinates of point on body in X,Y,Z coordinate system
j	specific radiation intensity
M_i	mass flow rate into shock layer
M_o	mass flow rate out of shock layer at θ
$N = n/\Delta$	
n	normal distance from body surface
$\bar{n}$	number of subdivisions in Simpson's rule
p	pressure
p_t'	stagnation pressure behind normal shock
q	heat-transfer rate
q_C	convective heat-transfer rate
q_R	radiative heat-transfer rate
R	radius
R_c	corner radius

R_{eff}	effective radius
R_n	nose spherical radius
r	cylindrical radius of body (see fig. 4)
r_{max}	maximum cylindrical radius of body
$\bar{r}$	distance between point on body and dV
s	surface distance from stagnation point
T	temperature
t	time (t = 0 at 400,000 ft)
U	velocity
V	gas cap volume
W	vehicle weight
X,Y,Z	body-axis rectangular coordinate system
x,y,z	rectangular coordinate system, origin at point P on body
γ	reentry angle
Δ	local shock standoff distance from body
$\epsilon = \left(\rho_\infty/\rho_s\right)_{\theta=0}$	
ζ	vorticity
θ	angle measured from center line of body
θ_c	angle measured from forebody-corner line of tangency to line passing through any point on corner
θ_P	angle measured from center line of body to line passing through point P
θ_S	angle measured from center line of hypothetical sphere
θ_T	angle measured from center line of body to forebody-corner line of tangency
ρ	density
ρ_{sl}	density at sea level

ϕ angle measured from body normal to flow-field velocity

ω angle measured from body normal to direction of dV

Subscripts:

b at body surface

s behind shock, or of shock

t at stagnation point

∞ free stream

FLOW-FIELD ANALYSIS

Approximate inviscid flow fields were calculated for the Project Fire reentry vehicle at the following trajectory points, which were taken from the latest trajectory analysis available at the start of the present investigation:

Altitude, ft	Velocity, ft/sec	Time, sec	Configuration
260,460	37,058	15	1
218,000	36,700	19	1
166,000	34,800	25	2
147,000	30,100	27.6	2
120,000	19,500	32	3

The initial conditions for the trajectory from which the points were taken are: U_∞ = 37,000 ft/sec; $\bar{h}$ = 400,000 ft; γ = -15°; and W/C_DA = 35 lb/ft^2. The configuration numbers represent the shapes of the various beryllium calorimeters which, with the ablation shields, form the forebody of the vehicle. (See fig. 1.) The altitude and velocity at t = 25 seconds are the approximate conditions where the peak total heating rate is expected. A schematic of the heat pulse expected for the vehicle and the periods when the beryllium calorimeter and radiation sensors are expected to obtain useful data are shown in figure 2.

The basic assumptions made during the flow-field analysis were:

(1) Equilibrium flow

(2) Pressure distribution known (based on wind-tunnel data)

(3) Shock shape known (based on wind-tunnel data)

It can be expected that nonequilibrium effects will be small except possibly at the highest altitude noted in the previous table; therefore, equilibrium flow was assumed to simplify the analysis.

Pressure distributions were obtained from low-enthalpy tunnel investigations at a Mach number of 8, and in order to apply them to flight conditions, it was necessary to assume that the pressure distribution, with respect to the stagnation-point value, was invariant with gas conditions. Because of minor changes in the final vehicle shape, some adjustment of the pressure distribution was required to account for the differences in the models and the final vehicle forebody. These adjustments were minor and should have negligible effects on the results. The actual pressure distributions used throughout the present analysis for the three beryllium calorimeters are presented in figure 3.

The shocks for configurations 1 and 2, obtained from tunnel investigations at a Mach number of 8, were concentric with the forebody to the line of tangency between the forebody and the corner. Concentricity of the shock was also found to exist for configuration 2 in a high-enthalpy expansion tube. This concentricity of the shock was assumed for the third calorimeter in lieu of a measured shock shape. With this assumption, the shock standoff distance was the only unknown required to define the shock envelope over the forebody. The shock standoff distance was obtained from the correlation presented in reference 1, which can be used to obtain a relationship between R_b and R_{eff}, and the following equation for shock standoff distance: $\Delta/R_{eff} \approx 0.8\left(\rho_\infty/\rho_s\right)$. Downstream of the conical surface defined by the forebody-corner tangency line and noted by its half-angle θ_T (see fig. 4), the shock was assumed to be described by a second-order curve given as:

$$\frac{Y}{R_n} = a_1\left(\frac{X}{R_n}\right)^2 + a_2\left(\frac{X}{R_n}\right) + a_3 \tag{1}$$

This curve was required to pass through the proper point along the line at θ_T with the correct slope and to pass through one additional point near the most rearward region that could influence the radiation heating up to and including the forebody-corner line of tangency. This latter point was obtained from the measured shock shape for configuration 2.

Since the pressure distribution along the body and the shock shape were known, the fluid conditions along the body and downstream of the shock could be determined. In order to determine the fluid properties in the inviscid shock layer, it was assumed that the pressure and velocity distributions across the layer along a normal from the surface could be expressed in terms of a second-order polynomial of the form:

$$\left.\begin{aligned}\frac{p}{p_b} &= b_1N^2 + b_2N + b_3\\ \frac{U}{U_b} &= c_1N^2 + c_2N + c_3\end{aligned}\right\} \tag{2}$$

The three unknown coefficients in each of these equations were determined from the conditions at the wall, the conditions downstream of the shock, and the gradient at the wall. The pressure gradient at the wall, obtained from the inviscid momentum equation, is:

$$\left(\frac{\partial p}{\partial n}\right)_b = \frac{U_b^2 \rho_b}{R_b} \tag{3}$$

The velocity gradient can be obtained from the expression for the vorticity of a fluid behind a shock; this equation for vorticity is given in reference 2 as:

$$\zeta_b = -\frac{(1-\epsilon)^2}{\epsilon}\left[\frac{\rho_b T_b}{(\rho_s T_s)_{\theta=0}}\right]\frac{r U_\infty}{R_s^2} \tag{4}$$

The velocity gradient normal to a streamline is:

$$\frac{\partial U}{\partial n} = -\zeta - \frac{U}{R} \tag{5}$$

Combining equations (4) and (5) gives the normal velocity gradient along the body surface as:

$$\left(\frac{\partial U}{\partial n}\right)_b = \frac{(1-\epsilon)^2}{\epsilon}\left[\frac{\rho_b T_b}{(\rho_s T_s)_{\theta=0}}\right]\frac{U_\infty r}{R_s^2} - \frac{U_b}{R_b} \tag{6}$$

The values for $\left(\frac{\partial p}{\partial n}\right)_b$, $\left(\frac{\partial U}{\partial n}\right)_b$, p_b, p_s, U_b, and U_s permit the coefficients in equations (2) to be evaluated. With the pressure and velocity known and constant total enthalpy assumed throughout the shock layer, the other equilibrium fluid properties can be obtained from suitable gas tables or charts for air. (See, for example, ref. 3.) With the local fluid properties defined, the absorption or emission coefficient can be obtained from tabulated data. For the present analysis the emission coefficients were obtained from reference 4 for $\frac{\rho}{\rho_{sl}} \geqq 10^{-4}$. For $\frac{\rho}{\rho_{sl}} < 10^{-4}$ the emission coefficients were obtained from reference 5 since values for this low-density range were not included in reference 4.

Since the equations for the pressure and velocity distributions are written in terms of a coordinate system normal to and along the body surface, it is convenient to divide the flow-field analysis into two parts, that is, flow over the forebody $(\theta \leqq \theta_T)$ and flow around the corner $(\theta > \theta_T)$. (See fig. 4.) Some consideration must be given to the value of R_b since at the line of tangency

between the forebody and corner the body radius changes and results in a discontinuous change in the normal pressure and velocity gradients at $\theta = \theta_T$. Since the flow is subsonic, it does not appear reasonable from a physical viewpoint to have this discontinuity. Therefore, in order to eliminate this discontinuity in the gradients normal to the body, an effective body radius was calculated. This calculation was made by assuming that the effective radius of the body is equal to the radius of a sphere which has the same pressure gradient along its surface at equal angles with respect to the free-stream velocity. A Newtonian pressure distribution was assumed to exist over the hypothetical sphere. With these assumptions, the effective body radius becomes:

$$\frac{R_{eff}}{R} = -\frac{2 \cos \theta_S \sin \theta_S}{\frac{d\left(p/p_t'\right)}{d(s/R)}} \tag{7}$$

where $\frac{d\left(p/p_t'\right)}{d(s/R)}$ is determined from the measured pressure data for the body. This effective radius was used throughout the analysis for R_b in equations (3) and (6). It should be noted that this definition of R_{eff} should give the same values for R_{eff} at the stagnation point as given in reference 1. A plot of R_{eff} and R_b for configuration 2 is given in figure 5 to show the difference in the two quantities. Figures 6 to 10 present the temperature, density, and specific radiation intensity calculated by the previously discussed method for both the forebody and corner flow fields. In general, the fluid properties vary fairly uniformly over the forebody and around the corner up to a value of θ_c of about 30° to 40°. For larger values of θ_c the flow-field properties appear to be somewhat erratic, and this can probably be attributed to the simplicity of the present method.

Except for the gas in the immediate vicinity of the point for which the radiation heating rate is being calculated, the irregularity of the flow-field fluid properties for large values of θ_c has little influence on the radiation heating rate to the forebody due to the distances and view angle involved. The limit of the flow field that is viewed by the forebody-corner tangency point is noted on the curves in figures 6 to 10 by the dots.

It should be pointed out that although no iterations were made during this analysis, the method employed could be revised to permit iteration on the shock location by balancing the mass flow within the shock layer. In order to obtain some quantitative evaluation of the self consistency of the calculated flow fields, a mass-flow balance was made at $\theta = 15^\circ$. The results of this balance are shown in figure 11 and indicate that based on the criterion of mass flow, the flow fields appear to be only fairly accurate.

The mass-flow balance could be influenced by three things: the calculated density and velocity distributions across the shock layer, the shock standoff distance, and the flow angularity with respect to the area over which the mass-flow balance was calculated. The variation of the flow angle with respect to the normal from the body surface was assumed to be linear between the value at

the body ($\phi = 90^{\circ}$) and the value calculated behind the shock for an oblique shock. The density and velocity distributions across the shock layer depend on the value of R_{eff}. A comparison between the mass-flow balance for $R = R_{eff}$ and $R = R_n$ in equations (3) and (6) indicates that there is little difference between the two methods. The mass-flow balance parameter $\left(1 - \frac{M_o}{M_i}\right)$ for the flow field calculated for $R = R_{eff}$ was 0.132 and for $R = R_n$ was 0.1435. Therefore, if the flow-angularity assumption is reasonable, the mass-flow deficit must be predominately due to the shock standoff distance which is too small.

RADIATION HEATING CALCULATIONS

The quantity of energy received at a point P from a surrounding radiating gas that is transparent, nonscattering, and in equilibrium can be expressed as

$$q_R = \int_V \frac{j \cos \omega \, dV}{r^2} \tag{8}$$

Equation (8) is written for a coordinate system with its origin located at the point P receiving the radiant energy. It is convenient to express this equation in a body-axis coordinate system; the details of this transformation are outlined in the appendix. Applying the resultant equation to a portion of a sphere at zero angle of attack gives:

$$q_R = 2 \iiint \frac{j \left| \left[(X - h)\cos \theta_P + (Y - k)\sin \theta_P \right] \right| dX \, dY \, dZ}{\left[(X - h)^2 + (Y - k)^2 + (Z - l)^2 \right]^{3/2}} \tag{9}$$

The limits of integration are as follows:

for Z,

$$\left.\begin{aligned} &\frac{Y}{X} \leqq \tan \theta_T \\ &0 \leqq \frac{Z}{R_n} \leqq \sqrt{\left(1 + \frac{\Delta}{R_n}\right)^2 - \left(\frac{X}{R_n}\right)^2 - \left(\frac{Y}{R_n}\right)^2} \\ &\frac{Y}{X} > \tan \theta_T \\ &0 \leqq \frac{Z}{R_n} \leqq \sqrt{\left[a_1 \left(\frac{X}{R_n}\right)^2 + a_2 \frac{X}{R_n} + a_3\right]^2 - \left(\frac{Y}{R_n}\right)^2} \end{aligned}\right\} \tag{10}$$

for Y (upper),

$$\left.\begin{aligned} &\frac{X}{R_n} < \left(1 + \frac{\Delta}{R_n}\right)\cos\theta_T \\ &\frac{Y}{R_n} = a_1\left(\frac{X}{R_n}\right)^2 + a_2\frac{X}{R_n} + a_3 \\ &\frac{X}{R_n} \geqq 1 + \frac{\Delta}{R_n}\cos\theta_T \\ &\frac{Y}{R_n} = \sqrt{\left(1 + \frac{\Delta}{R_n}\right)^2 - \left(\frac{X}{R_n}\right)^2} \end{aligned}\right\} \qquad (11)$$

for Y (lower),

$$\left.\begin{aligned} &\frac{X}{R_n} < \cos\theta_P + \sin\theta_P\sqrt{2\frac{\Delta}{R_n} + \left(\frac{\Delta}{R_n}\right)^2} \\ &\frac{Y}{R_n} = \frac{1}{\sin\theta_P} - \frac{X}{R_n}\cot\theta_P \\ &\frac{X}{R_n} \geqq \cos\theta_P + \sin\theta_P\sqrt{2\frac{\Delta}{R_n} + \left(\frac{\Delta}{R_n}\right)^2} \\ &\frac{Y}{R_n} = -\sqrt{\left(1 + \frac{\Delta}{R_n}\right)^2 - \left(\frac{X}{R_n}\right)^2} \end{aligned}\right\} \qquad (12)$$

for X (lower),

$$\left.\begin{aligned} &\theta_P > \theta_T - \cos^{-1}\frac{1}{1 + \frac{\Delta}{R_n}} \\ &\frac{X}{R_n} = -\frac{\left(a_2 + \cot\theta_P\right)}{2a_1} - \sqrt{\frac{\left(a_2 + \cot\theta_P\right)^2}{4a_1^2} - \frac{\left(a_3 - \frac{1}{\sin\theta_P}\right)}{a_1}} \\ &\theta_P \leqq \theta_T - \cos^{-1}\frac{1}{1 + \frac{\Delta}{R_n}} \\ &\frac{X}{R_n} = \cos\theta_P - \sin\theta_P\sqrt{2\frac{\Delta}{R_n} + \left(\frac{\Delta}{R_n}\right)^2} \end{aligned}\right\} \qquad (13)$$

and for X (upper),

$$\left.\begin{aligned} \cos\theta_p &< \frac{1}{1+\frac{\Delta}{R_n}} \\ \frac{X}{R_n} &= \cos\theta_p + \sin\theta_p\sqrt{2\frac{\Delta}{R_n}+\left(\frac{\Delta}{R_n}\right)^2} \\ \cos\theta_p &\geqq \frac{1}{1+\frac{\Delta}{R_n}} \\ \frac{X}{R_n} &= 1+\frac{\Delta}{R_n} \end{aligned}\right\} \qquad (14)$$

TABLE 1

θ_p, deg	$\bar{n}$
0	10
5	12
10	14
15	16
20	18
>20	20

Equation (9) was integrated by Simpson's rule where the number of subdivisions, $\bar{n}$, along the X coordinate axis was taken as given in table 1. Along the Y- and Z-axes, $\bar{n} = 100$.

An indication of the convergence of the integration to a given value as $\bar{n}$ increases is shown in figure 12 for $t = 25$ seconds; the solid curves represent the envelope of the maximum and minimum variation of the radiation heating with $\bar{n}$. If it is assumed that the correct value of q_R is the average value obtained with $\bar{n} = 100$ and $\bar{n} = 102$, the value for $\bar{n} = 100$ is in error only about 1 percent.

The number of subdivisions, $\bar{n}$, along the X-axis was varied from $\bar{n} = 10$ at $\theta_p = 0$ to $\bar{n} = 20$ for the largest value of θ_p since the absolute value of ΔX increased with increasing θ_p.

The radiation heat-transfer distribution and the stagnation-point heating rate are presented in figures 13 and 14. All the distributions are similar with the radiation heating decreasing to about 0.2 to 0.4 of the stagnation-point value at $\theta = \theta_T$. The radiation heat-transfer distribution for the semi-infinite slab approximation is also presented in figure 13. This approximation is similar to the slab approximation usually used at the stagnation point except that an average value of the specific intensity obtained from the values behind the shock and at the wall is used with the local shock standoff distance. The results indicate that this approximation gives an excellent indication of the distribution when one considers its simplicity. This result is in agreement with a more detailed slab approach made in reference 6.

The mass-flow discrepancy noted previously in the section entitled "Flow-Field Analysis" will influence the magnitude of the radiation heating since the error is believed to be predominantly due to the shock standoff distance being too small by approximately the same percentage as the mass-flow balance. If the slab approximation is considered, the absolute magnitude of the heating would increase in proportion to the mass-flow error, but the distribution would be essentially unchanged.

The stagnation-point radiative heating rates shown in figure 14 are relatively low for all points investigated except for $t = 25$ seconds where the heating rate is about 400 Btu/sec-ft^2. Also shown in figure 14 is the slab approximation for the stagnation-point heating rate.

It should be noted that the radiative heating rate is dependent on the specific-radiation-intensity data used. To date this gas property is not known to great accuracy and different values are given by different investigators. For the most part the radiation intensity data used for this investigation were taken from reference 4 since it was generally accepted that the best data available at the start of this investigation are given in this reference. Recently it has been suggested that these intensities are low. In order to show the influence of the various radiation intensity data, the stagnation-point heating rate and the forebody distribution for $t = 25$ seconds were calculated by using the data of references 4, 5, and 7. The results of these calculations are presented in figure 15. The stagnation-point heat-transfer rates range from 410 Btu/sec-ft^2, if the data of reference 4 are used, to 946 Btu/sec-ft^2, for the data from reference 7. There was no change in the radiation heating distribution obtained by using the various specific-intensity data.

The difference between the heating estimates can be partly attributed to the larger wavelength range considered for calculating the specific intensities in reference 7. The wavelength range for the data of reference 7 was from 0.05 to 10 microns whereas the range was from 0.16 to 10 microns for reference 4. It is expected that the Project Fire flight data will reduce the uncertainty in predicting the radiation heating. It should be noted, however, that most of the added energy in the wave length increment from 0.05 to 0.16 micron considered in reference 7 will not be transmitted to the vehicle radiation sensors since the quartz windows in the forebody absorb most of the radiation below about 0.18 micron. Thus, this increment in radiation heating must be, in some way, inferred from convective-heating calculations and measured total heating rates.

In addition to this complication, self absorption of radiant energy within the gas cap might become significant, particularly in the small wavelength region considered in reference 7.

CONVECTIVE HEATING

The convective heat-transfer distribution around the vehicle was calculated by using the correlations presented in reference 8. The results of the calculations of the heat-transfer distribution are presented in figure 16.

This figure shows that the heating rate is essentially constant over the forebody; the high heating rate sometimes encountered at the outer edge of blunt bodies does not occur. The variation at the outer edge of the body is never greater than ±10 percent of the stagnation-point value.

The stagnation-point heat-transfer rate was calculated from the correlated results of reference 9 for the high-enthalpy case. The results of these calculations are presented in figure 17. The maximum convective stagnation-point heating rate calculated was 740 Btu/sec-ft^2. This convective heating rate is almost twice the radiative heating rate calculated by the data of reference 4 and about 20 percent less than the radiative heating rate calculated by the data of reference 7. Thus, it is not clear whether the convective heating rate will dominate the peak stagnation-point heating to the vehicle or whether radiative and convective heating will contribute equally to the total peak heating rate. The radiative and total heating rates are also plotted in figure 17. The maximum total heating rate to the stagnation point will range from about 1150 to about 1690 Btu/sec-ft^2 depending upon the radiation data used.

COMPARISON OF PRESENT RESULTS WITH MORE EXACT ANALYSES

The present results are compared with the results of more exact calculations made by the General Electric Company, Lockheed Missiles and Space Company, and Philco Corporation under contract to the NASA Office of Advanced Research and Technology. The results of these comparisons are shown in figure 18. The figure indicates that there is considerable disagreement between the four sets of results. This is particularly true for the convective and radiative heat-transfer distributions and for the stagnation-point radiative heating rate except when the same specific radiation intensity data are used.

The stagnation-point convective heat-transfer rate of the present report compares favorably with the contractor results except for $t = 15$ seconds where the present results are about 50 percent of the highest estimate. The present estimates of the stagnation-point radiative heating rate for $t \approx 25$ seconds agree well with the other results provided the same specific radiation intensity data are used. There is a great deal of difference between the stagnation-point radiative heating rate for $t = 15$ seconds where nonequilibrium effects can influence the radiative heating rate. The present results for this case are in fair agreement with Philco's results.

It is somewhat surprising that the convective and radiation estimates of heat-transfer distributions differ by such a large amount. The present results fall between the maximum and minimum values predicted by the contractors. The present radiation distribution agrees closely with Philco's results whereas the present convective distribution agrees fairly well with General Electric's results. From an overall point of view, the simplified analysis of the present report gives results which compare favorably with the results obtained from more exact calculations.

CONCLUSIONS

Calculations of the approximate equilibrium flow fields for the forebody of the Project Fire reentry vehicle at zero angle of attack and the resulting convective and equilibrium radiation heat-transfer calculations permit the following conclusions:

1. The radiation stagnation-point heating rate is greatly influenced by the specific-radiation-intensity data used and ranged from a low of 410 Btu/sec-ft^2 to a high of 946 Btu/sec-ft^2.

2. The radiation heat-transfer rate over the forebody decreases fairly rapidly from the stagnation point to the outer diameter of the vehicle. The heating rate at the forebody-corner tangency point is only about 0.2 to 0.4 of the stagnation-point value.

3. The peak convective stagnation-point heating rate is about 740 Btu/sec-ft^2. This rate combined with the peak radiation heating results in a peak total heating rate that ranges from 1150 to 1690 Btu/sec-ft^2 depending on the radiation data used.

4. The convective heat-transfer rate over the forebody is essentially constant, never varying more than ±10 percent of the stagnation-point value.

5. For the case considered, the radiative heat-transfer distributions obtained by a simple slab approximation are in good agreement with those obtained by integrating the specific intensity over the calculated gas cap volume.

6. In general, the simplified analysis of the present report gives results which compare favorably with the results obtained from more exact calculations.

Langley Research Center,
National Aeronautics and Space Administration,
Langley Station, Hampton, Va., October 21, 1964.

APPENDIX

RADIATION HEATING EQUATION

The heat-transfer rate to a point P from a surrounding radiating gas that is transparent, nonscattering, and in equilibrium can be expressed as

$$q_R = \int_V \frac{j \cos \omega \, dV}{r^2} \tag{A1}$$

This equation is written for a coordinate system with its origin located at the point P receiving the radiant energy. It is convenient to express this equation in a body-axis coordinate system. First, expressing the equation in terms of a rectangular Cartesian coordinate system with the origin at the point P gives

$$q_R = \iiint \frac{j(|x|)dx\,dy\,dz}{(x^2 + y^2 + z^2)^{3/2}} \tag{A2}$$

where:

(1) x is perpendicular to the body surface at P.

(2) y and z lie in the tangent plane at P.

(3) y lies in plane OAPB. (See fig. 19.)

In terms of a body-axis coordinate system equation (A2) becomes:

$$q_R = \iiint \frac{j\left|\left[(X - h)\cos \alpha_1 + (Y - k)\cos \beta_1 + (Z - l)\cos \gamma_1\right]\right| dX\,dY\,dZ}{\left[A(X - h)^2 + B(Y - k)^2 + C(Z - l)^2 + 2D(X - h)(Y - k) + 2E(X - h)(Z - l) + 2F(Y - k)(Z - l)\right]^{3/2}} \tag{A3}$$

where

$$\left.\begin{aligned} A &= \cos^2\alpha_1 + \cos^2\alpha_2 + \cos^2\alpha_3 \\ B &= \cos^2\beta_1 + \cos^2\beta_2 + \cos^2\beta_3 \\ C &= \cos^2\gamma_1 + \cos^2\gamma_2 + \cos^2\gamma_3 \\ D &= \cos\alpha_1 \cos\beta_1 + \cos\alpha_2 \cos\beta_2 + \cos\alpha_3 \cos\beta_3 \\ E &= \cos\alpha_1 \cos\gamma_1 + \cos\alpha_2 \cos\gamma_2 + \cos\alpha_3 \cos\gamma_3 \\ F &= \cos\beta_1 \cos\gamma_1 + \cos\beta_2 \cos\gamma_2 + \cos\beta_3 \cos\gamma_3 \end{aligned}\right\} \tag{A4}$$

$$\cos\alpha_1 : \cos\beta_1 : \cos\gamma_1 = \frac{\frac{\partial f}{\partial X} : \frac{\partial f}{\partial Y} : \frac{\partial f}{\partial Z}}{\sqrt{\left(\frac{\partial f}{\partial X}\right)^2 + \left(\frac{\partial f}{\partial Y}\right)^2 + \left(\frac{\partial f}{\partial Z}\right)^2}} \tag{A5}$$

$$\left.\begin{aligned} \cos\alpha_2 &= -\frac{h\cos\beta_1}{\sqrt{\sigma}} \\ \cos\beta_2 &= \frac{h\cos\alpha_1 + l\cos\gamma_1}{\sqrt{\sigma}} \\ \cos\gamma_2 &= -\frac{l\cos\beta_1}{\sqrt{\sigma}} \end{aligned}\right\} \tag{A6}$$

$$\left.\begin{aligned} \cos\alpha_3 &= \frac{l\left(\cos^2\beta_1 + \cos^2\gamma_1\right) + h\cos\alpha_1\cos\gamma_1}{\sqrt{\xi}} \\ \cos\beta_3 &= \frac{\cos\beta_1\left(h\cos\gamma_1 - l\cos\alpha_1\right)}{\sqrt{\xi}} \\ \cos\gamma_3 &= -\frac{\left[h\left(\cos^2\alpha_1 + \cos^2\beta_1\right) + l\left(\cos\alpha_1\cos\gamma_1\right)\right]}{\sqrt{\xi}} \end{aligned}\right\} \tag{A7}$$

$$\sigma = \left(h^2 + l^2\right)\cos^2\beta_1 + \left(h\cos\alpha_1 + l\cos\gamma_1\right)^2 \tag{A8}$$

$$\xi = \left[l\left(\cos^2\beta_1 + \cos^2\gamma_1\right) + h\left(\cos\alpha_1\cos\gamma_1\right)\right]^2 + \cos^2\beta_1\left(h\cos\gamma_1 - l\cos\alpha_1\right)^2 + \left[h\left(\cos^2\alpha_1 + \cos^2\beta_1\right) + l\cos\alpha_1\cos\gamma_1\right]^2 \tag{A9}$$

and h, k, and l are the coordinates of the point P in the X,Y,Z coordinate system. The body surface is given by

$$f(X,Y,Z) = 0 \tag{A10}$$

For the present case, the portion of the body for which the radiation heating was calculated was a portion of a sphere and the angle of attack was zero. Therefore, $h = R_b \cos \theta_p$, $k = R_b \sin \theta_p$, and $l = 0$; and

$$\cos \alpha_1 = \cos \theta_p \qquad \cos \alpha_2 = -\sin \theta_p \qquad \cos \alpha_3 = 0$$

$$\cos \beta_1 = \sin \theta_p \qquad \cos \beta_2 = \cos \theta_p \qquad \cos \beta_3 = 0$$

$$\cos \gamma_1 = 0 \qquad \cos \gamma_2 = 0 \qquad \cos \gamma_3 = 1$$

Also, $A = B = C = 1$ and $D = E = F = 0$. Thus, the equation for q_R becomes:

$$q_R = 2 \iiint \frac{j(\rho,T) \left| \left[(X - h)\cos \theta_p + (Y - k)\sin \theta_p \right] \right| dX\, dY\, dZ}{\left[(X - h)^2 + (Y - k)^2 + (Z - l)^2 \right]^{3/2}} \qquad \text{(A11)}$$

REFERENCES

1. Boison, J. Christopher; and Curtiss, Howard A.: An Experimental Investigation of Blunt Body Stagnation Point Velocity Gradient. ARS J., vol. 29, no. 2, Feb. 1959, pp. 130-135.

2. Hayes, Wallace D.; and Probstein, Ronald F.: Hypersonic Flow Theory. Academic Press, Inc. (New York), 1959.

3. Korobkin, I.; and Hastings, S. M.: Mollier Chart for Air in Dissociated Equilibrium at Temperatures of 2000° K to 15000° K. NAVORD Rep. 4446, U.S. Naval Ord. Lab. (White Oak, Md.), May 23, 1957.

4. Riethof, T.; and Nardone, M.: Radiation Theory. Doc. No. 62SD680 (Contract AF 04-(647)-617), Missile and Space Vehicle Dept., Gen. Elec. Co., Aug. 31, 1962.

5. Kivel, B.; and Bailey, K.: Tables of Radiation From High Temperature Air. Res. Rept. 21 (Contracts AF 04(645)-18 and AF 49(638)-61), AVCO Res. Lab., Dec. 1957.

6. Bobbitt, Percy J.: Effects of Shape on Total Radiative and Convective Heat Inputs at Hyperbolic Entry Speeds. Advances in Astronautical Sci., vol. 13, Eric Burgess, ed., Western Periodicals Co. (N. Hollywood, Calif.), c.1963, pp. 290-319.

7. Nardone, M. C.; Breene, R. G.; Zeldin, S. S.; and Riethof, T. R.: Radiance of Species in High Temperature Air. Tech. Inform. Ser. R63SD3 (Contract AF 04(694)-222), Missile and Space Div., Gen. Elec. Co., June 1963. (Available from DDC as AD No. 408564.)

8. Beckwith, Ivan E.; and Cohen, Nathaniel B.: Application of Similar Solutions to Calculation of Laminar Heat Transfer on Bodies With Yaw and Large Pressure Gradient in High-Speed Flow. NASA TN D-625, 1961.

9. Cohen, Nathaniel B.: Boundary-Layer Similar Solutions and Correlation Equations for Laminar Heat-Transfer Distribution in Equilibrium Air at Velocities up to 41,100 Feet Per Second. NASA TR R-118, 1961.

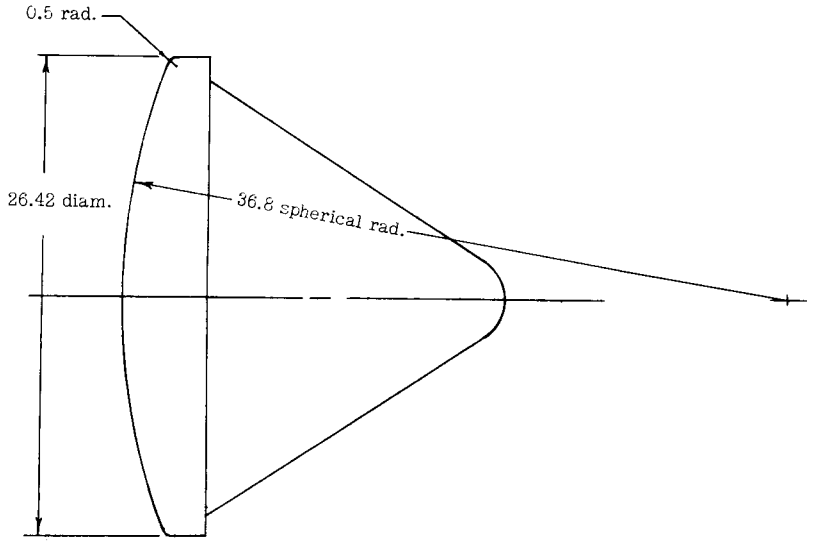

(a) Configuration 1 (first beryllium calorimeter).

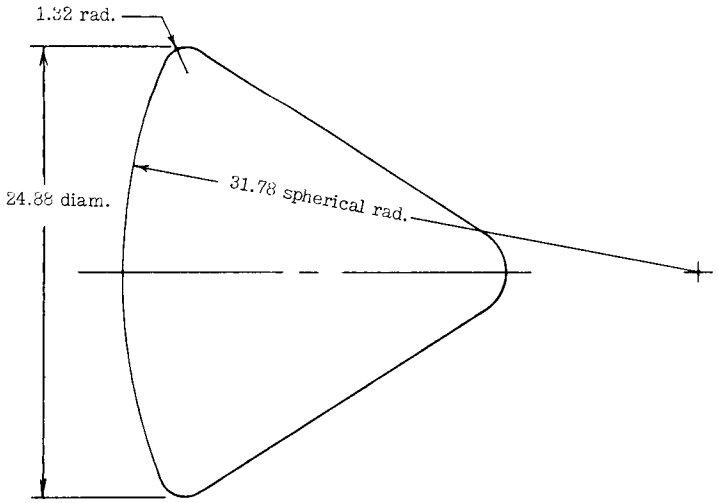

(b) Configuration 2 (second beryllium calorimeter).

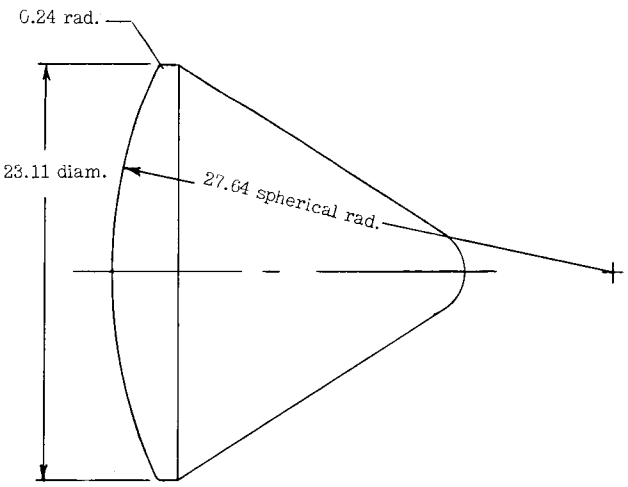

(c) Configuration 3 (third beryllium calorimeter).

Figure 1.- Forebody geometry. (All dimensions are in inches.)

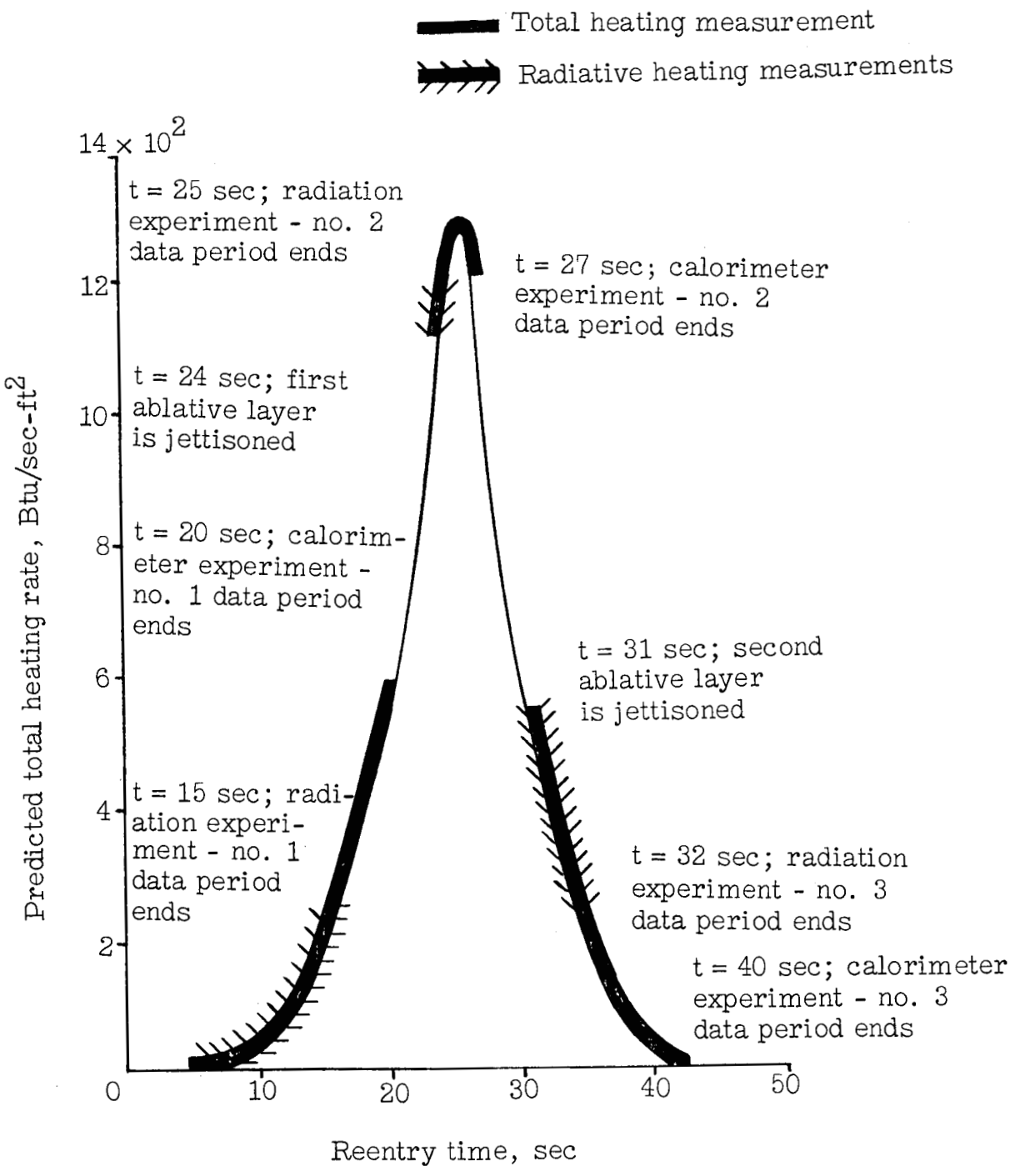

Figure 2.- Primary data periods showing total and radiative stagnation-point heating measurements. (At start of reentry, t = 0; all times are estimated.)

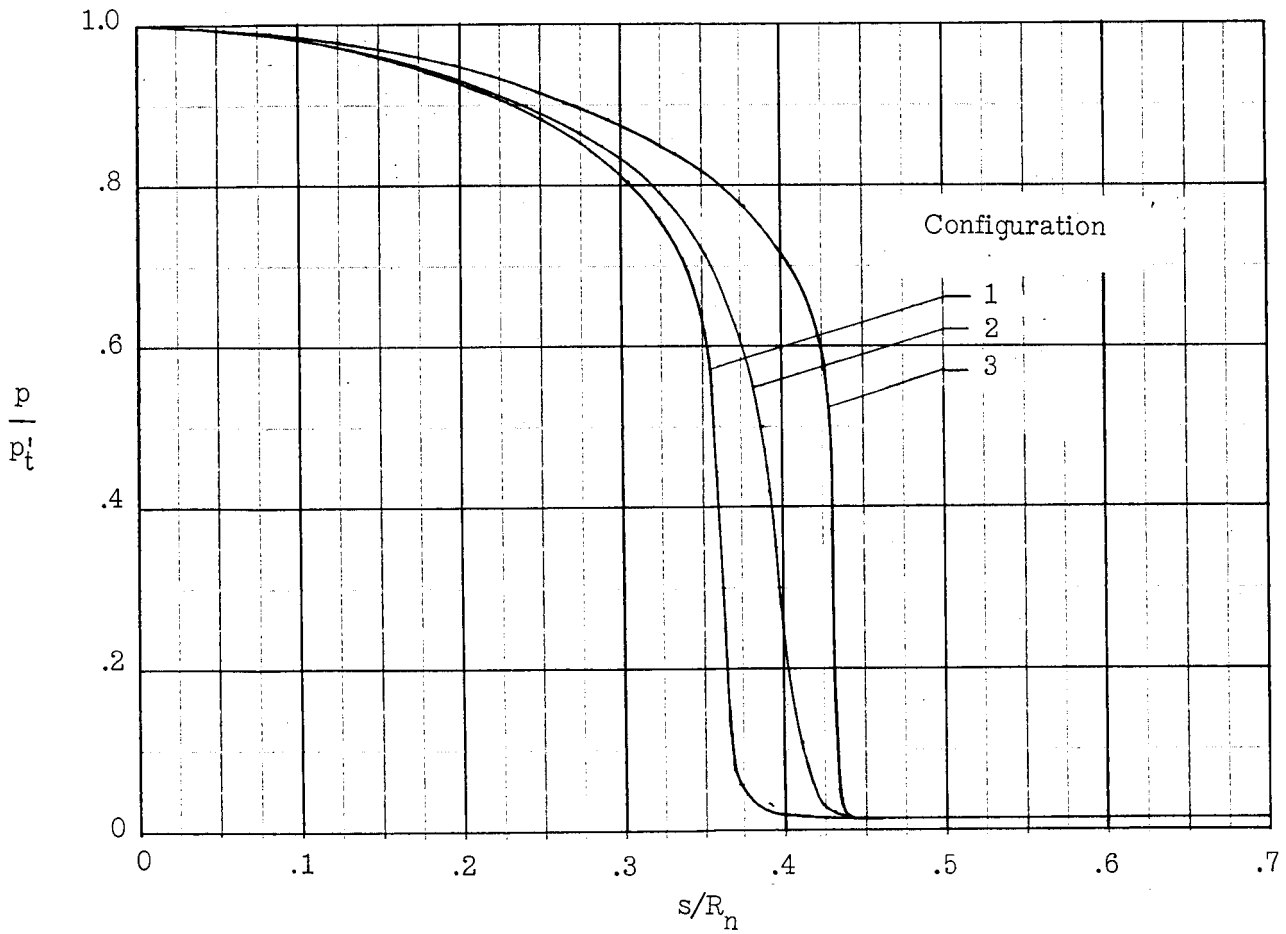

Figure 3.- Pressure distributions for the various forebody configurations.

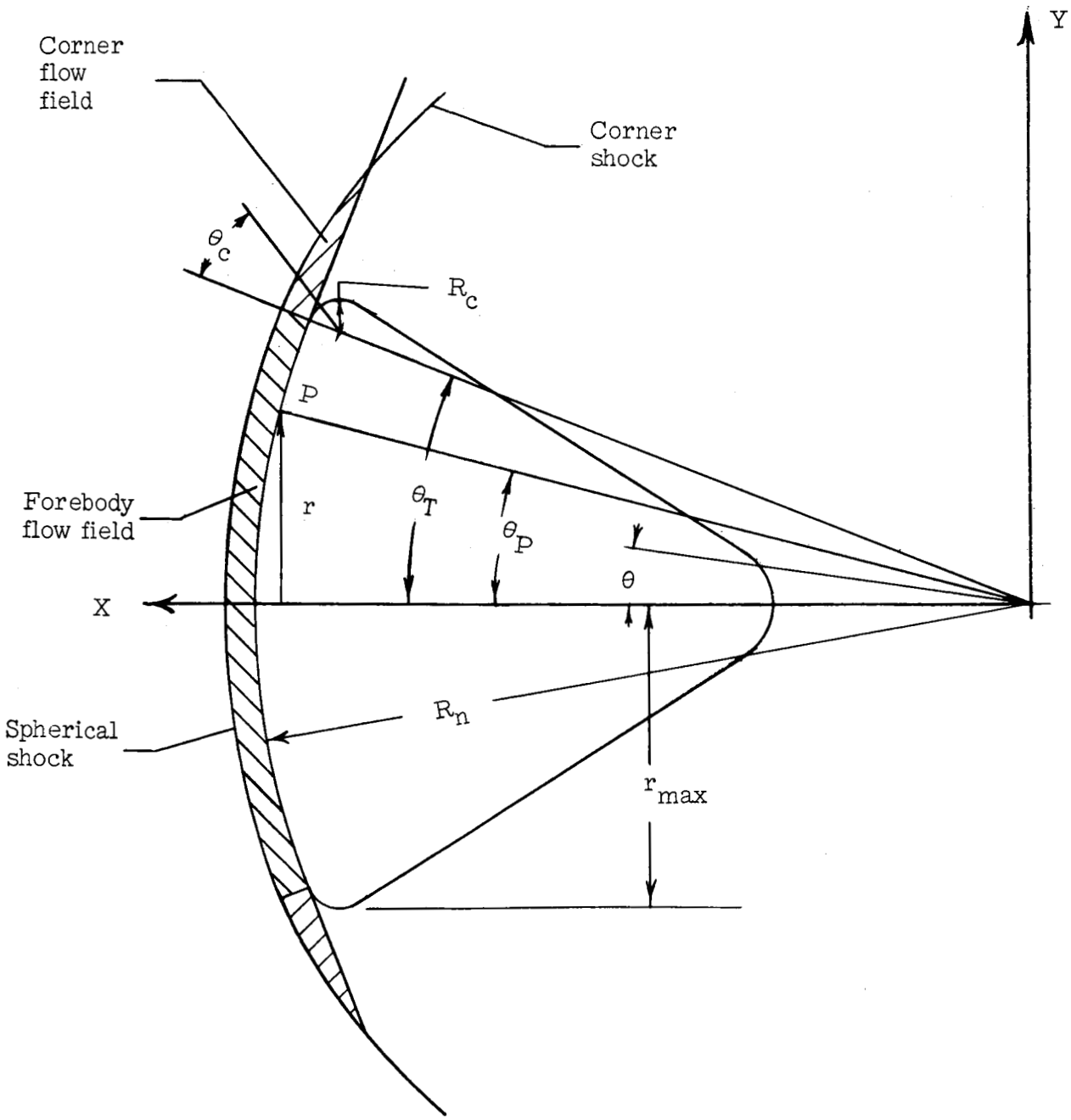

Figure 4.- Flow-field division for reentry vehicle.

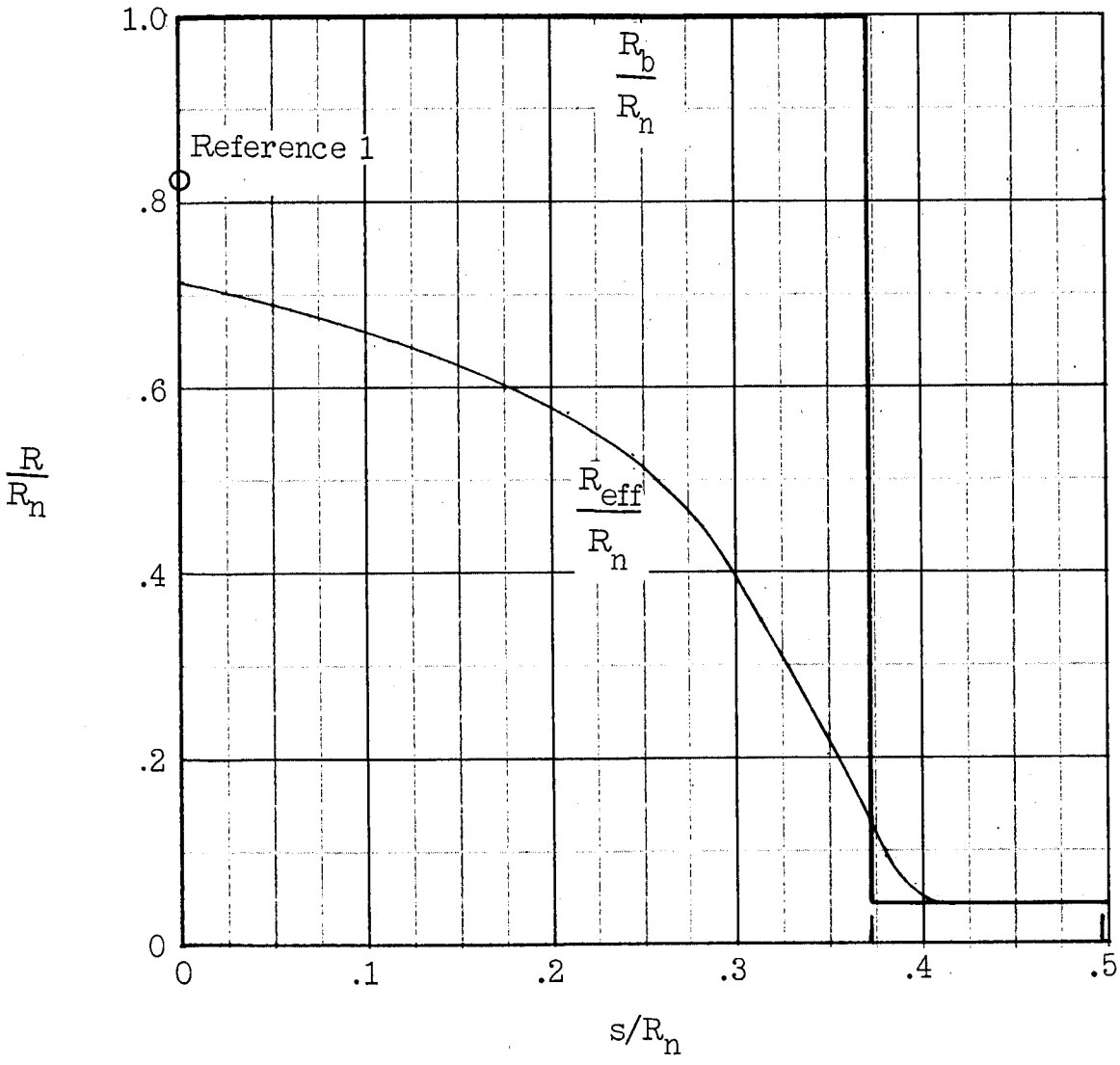

Figure 5.- Comparison of local body radius with effective radius. Configuration 2.

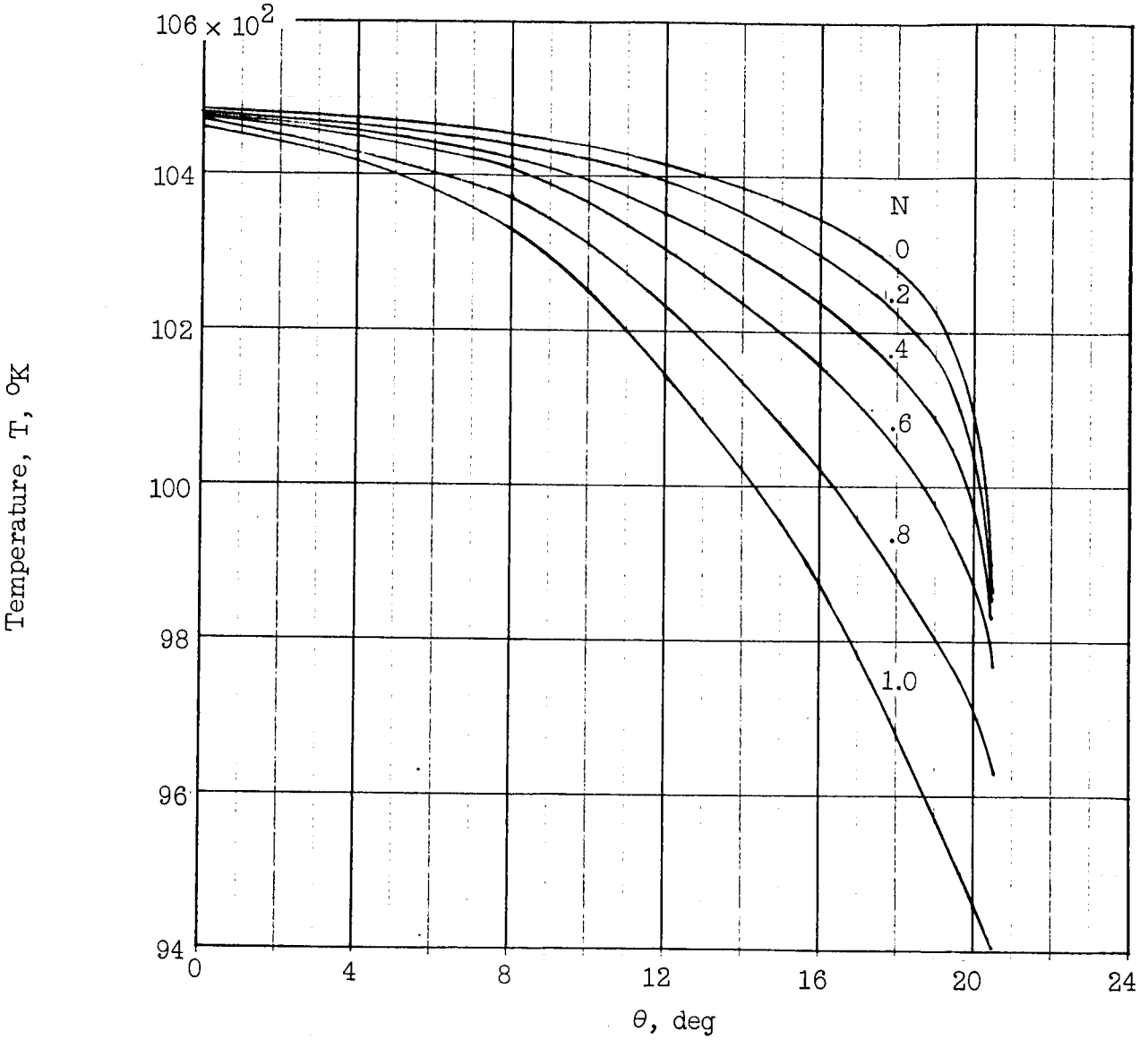

(a) Forebody temperature.

Figure 6.- Flow-field fluid properties for configuration 1. t = 15 sec; $\bar{h}$ = 260,460 ft; U_∞ = 37,058 ft/sec. (Dots denote limit of flow field viewed by forebody-corner tangency point.)

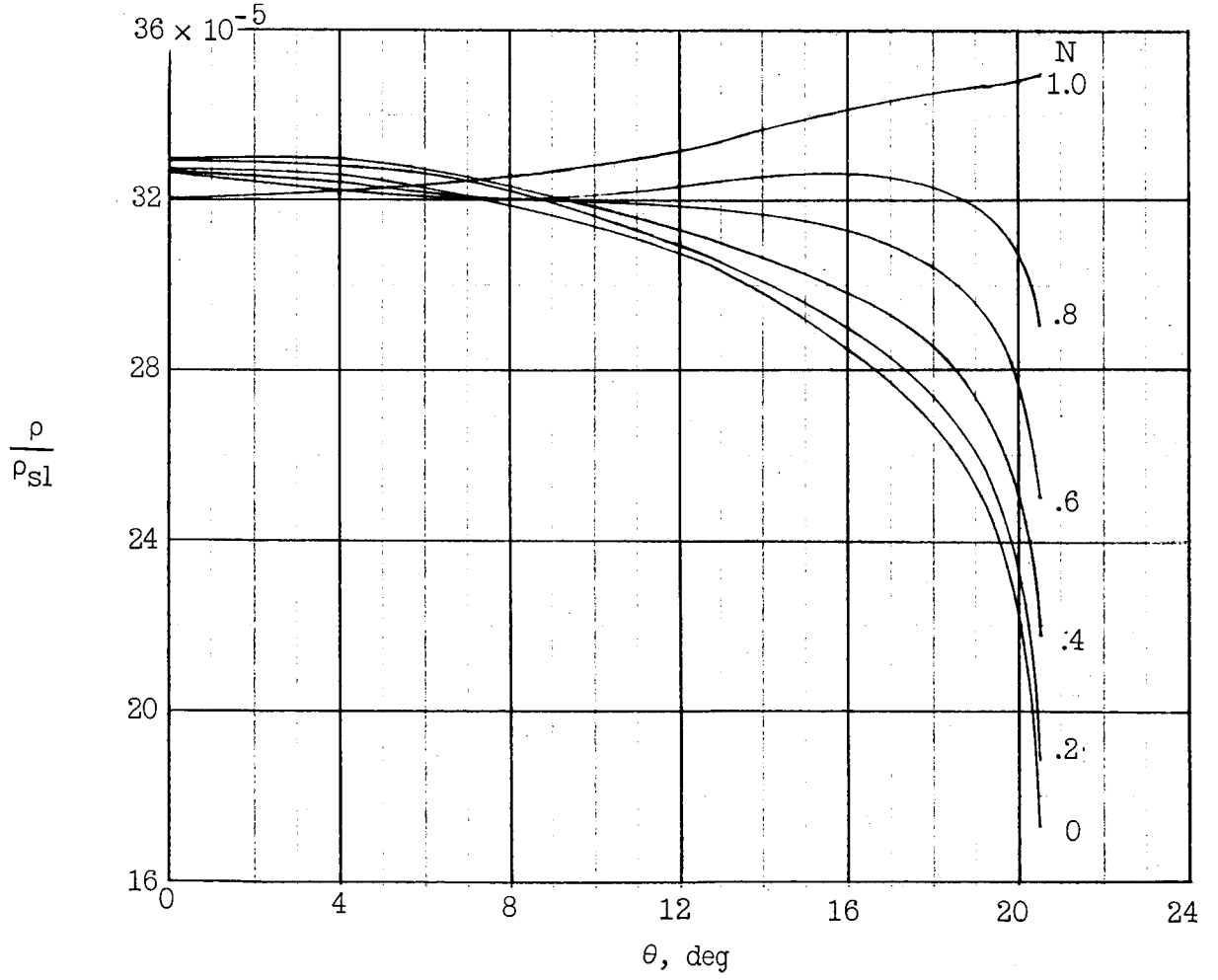

(b) Forebody density.

Figure 6.- Continued.

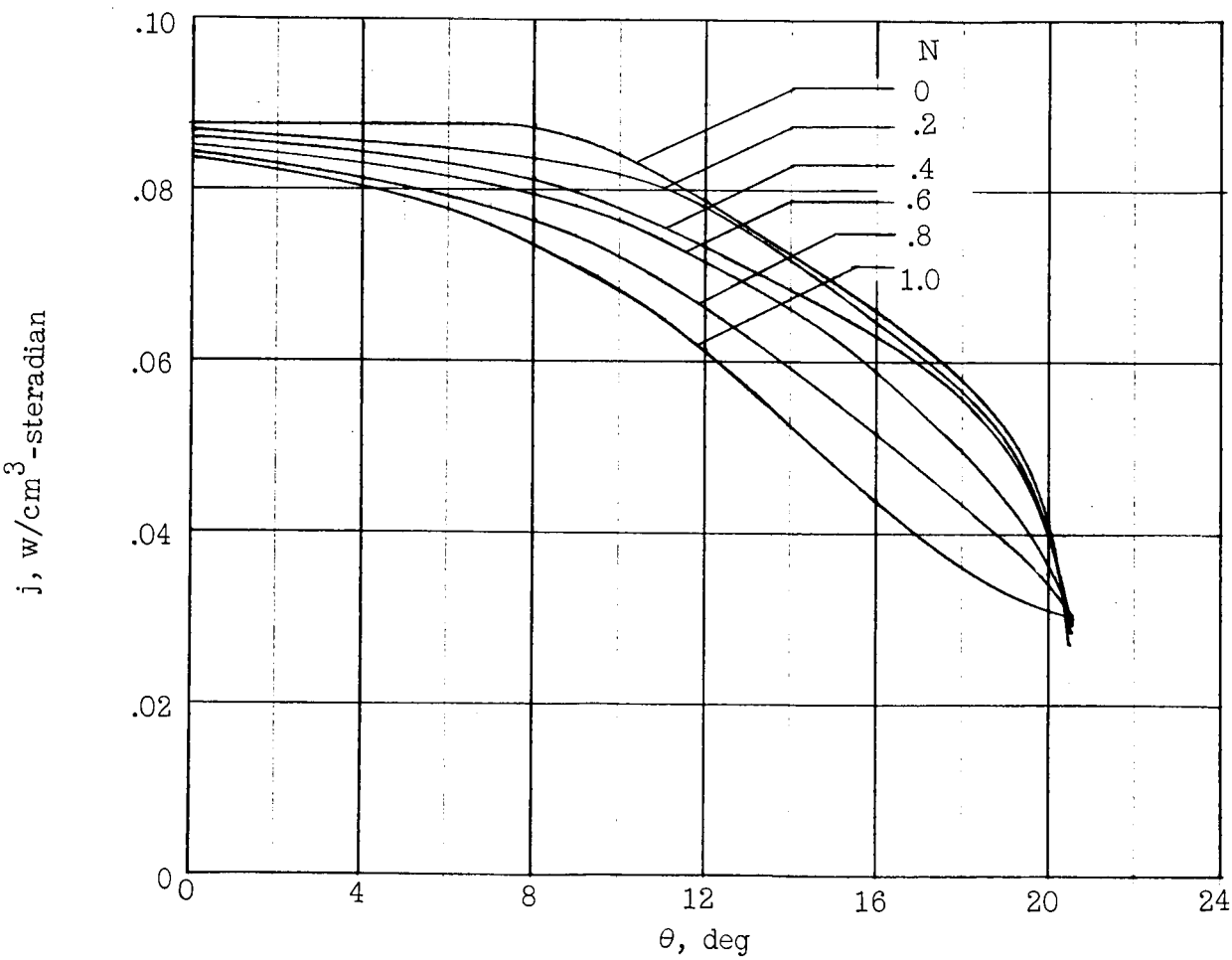

(c) Forebody specific radiation intensity.

Figure 6.- Continued.

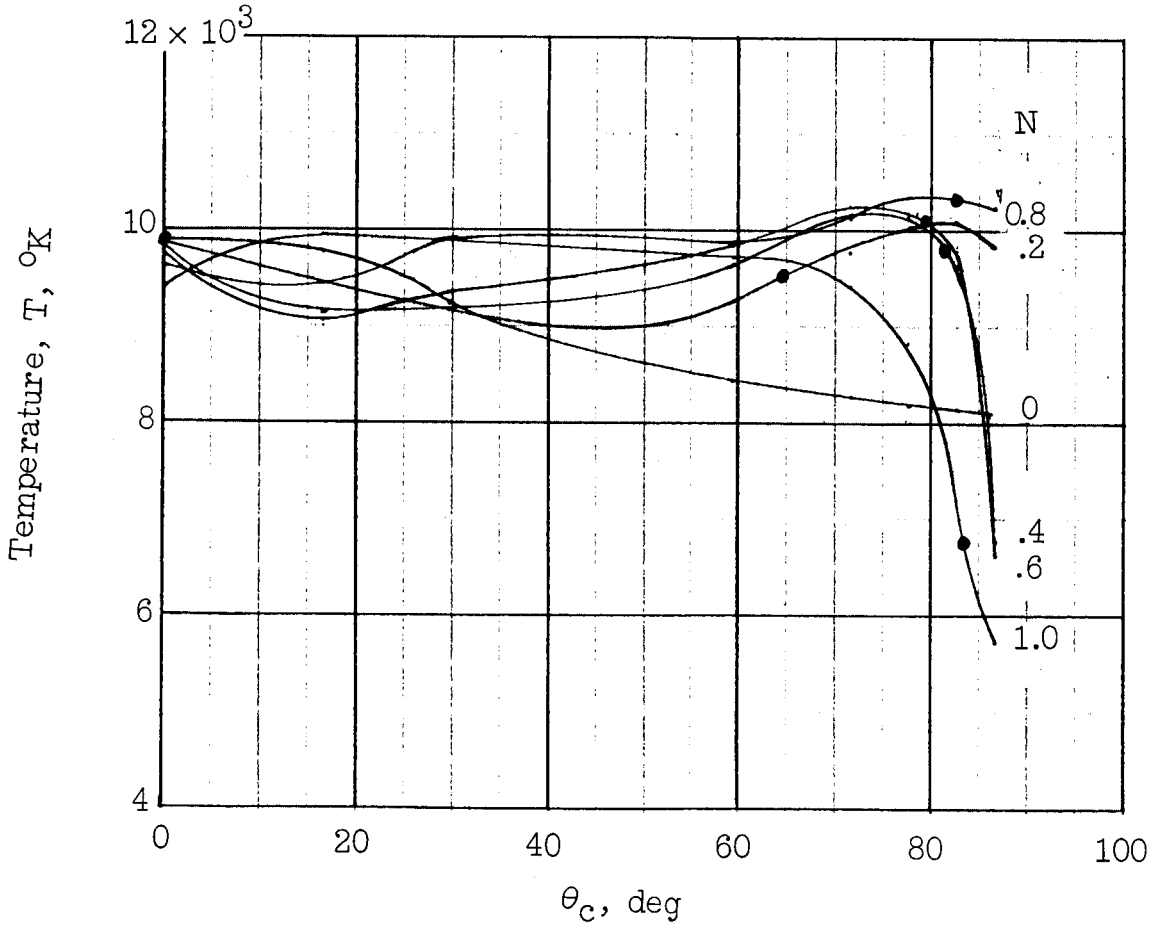

(d) Corner temperature.

Figure 6.- Continued.

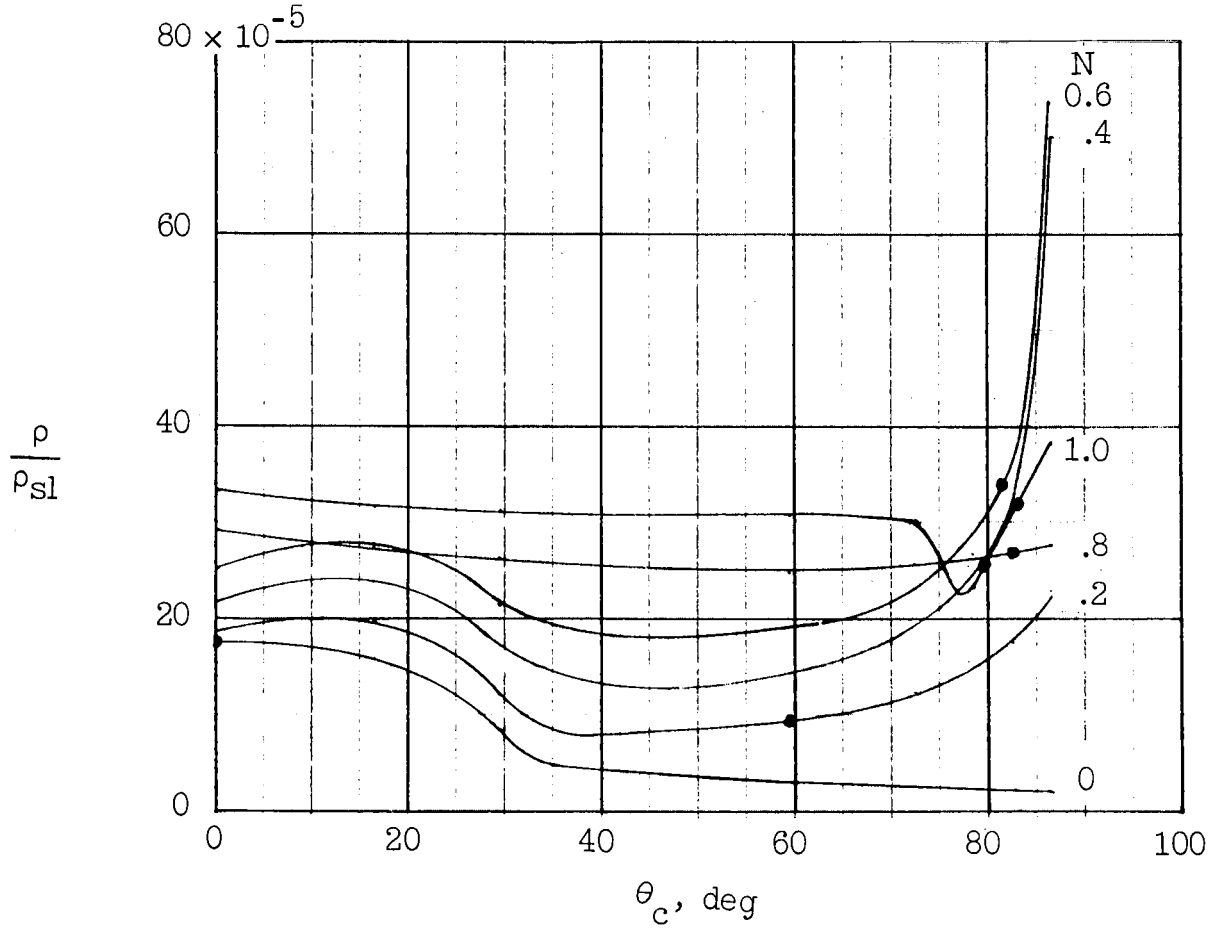

(e) Corner density.

Figure 6.- Continued.

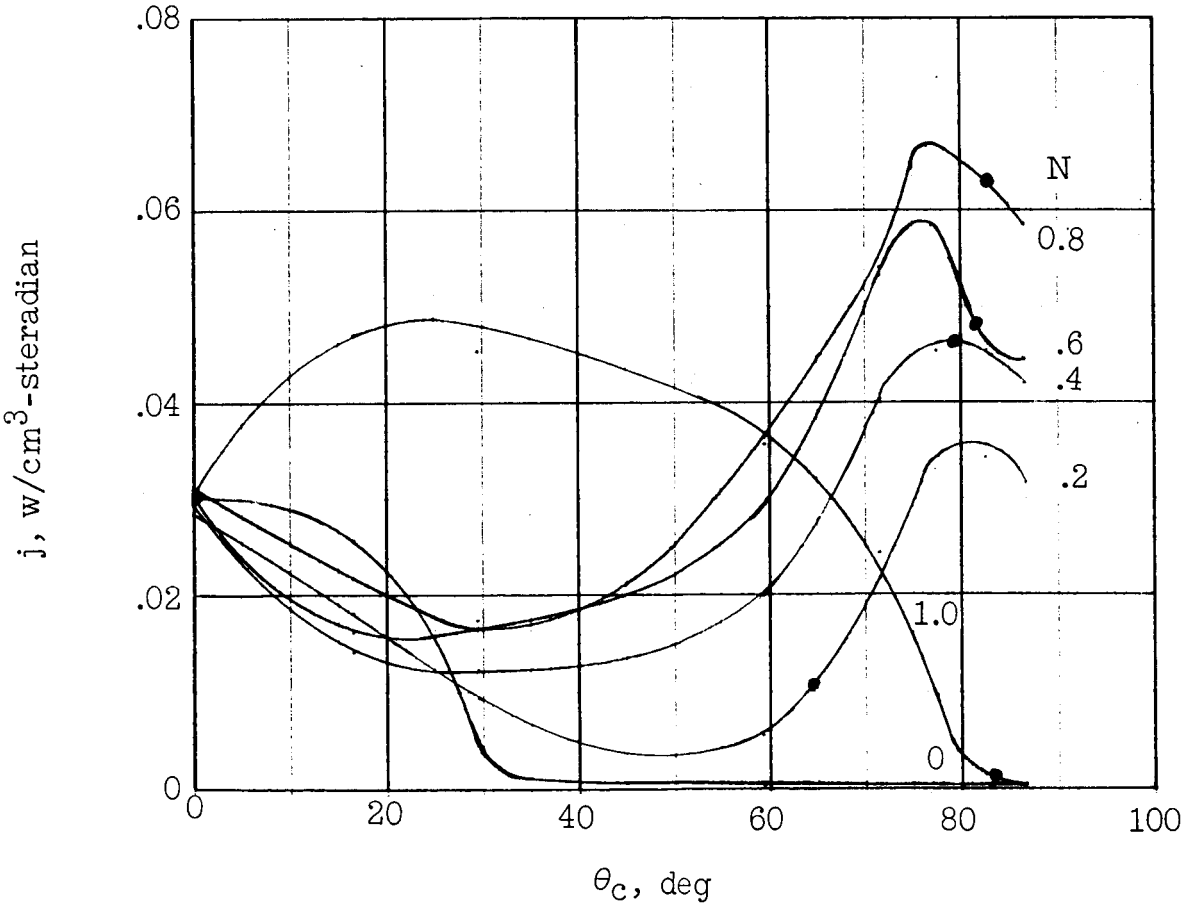

(f) Corner specific radiation intensity.

Figure 6.- Concluded.

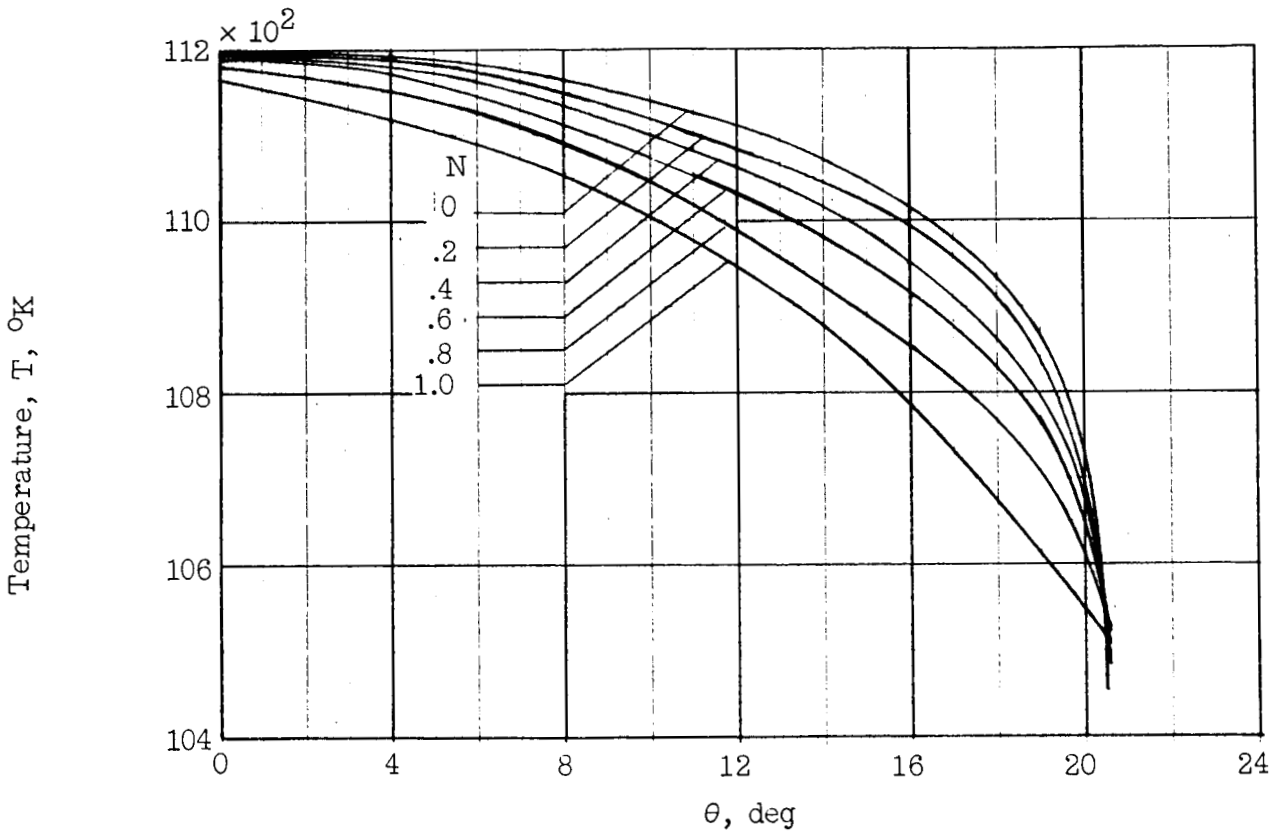

(a) Forebody temperature.

Figure 7.- Flow-field fluid properties for configuration 1. t = 19 sec; $\bar{h}$ = 218,000 ft; U_∞ = 36,700 ft/sec. (Dots denote limit of flow field viewed by forebody-corner tangency point.)

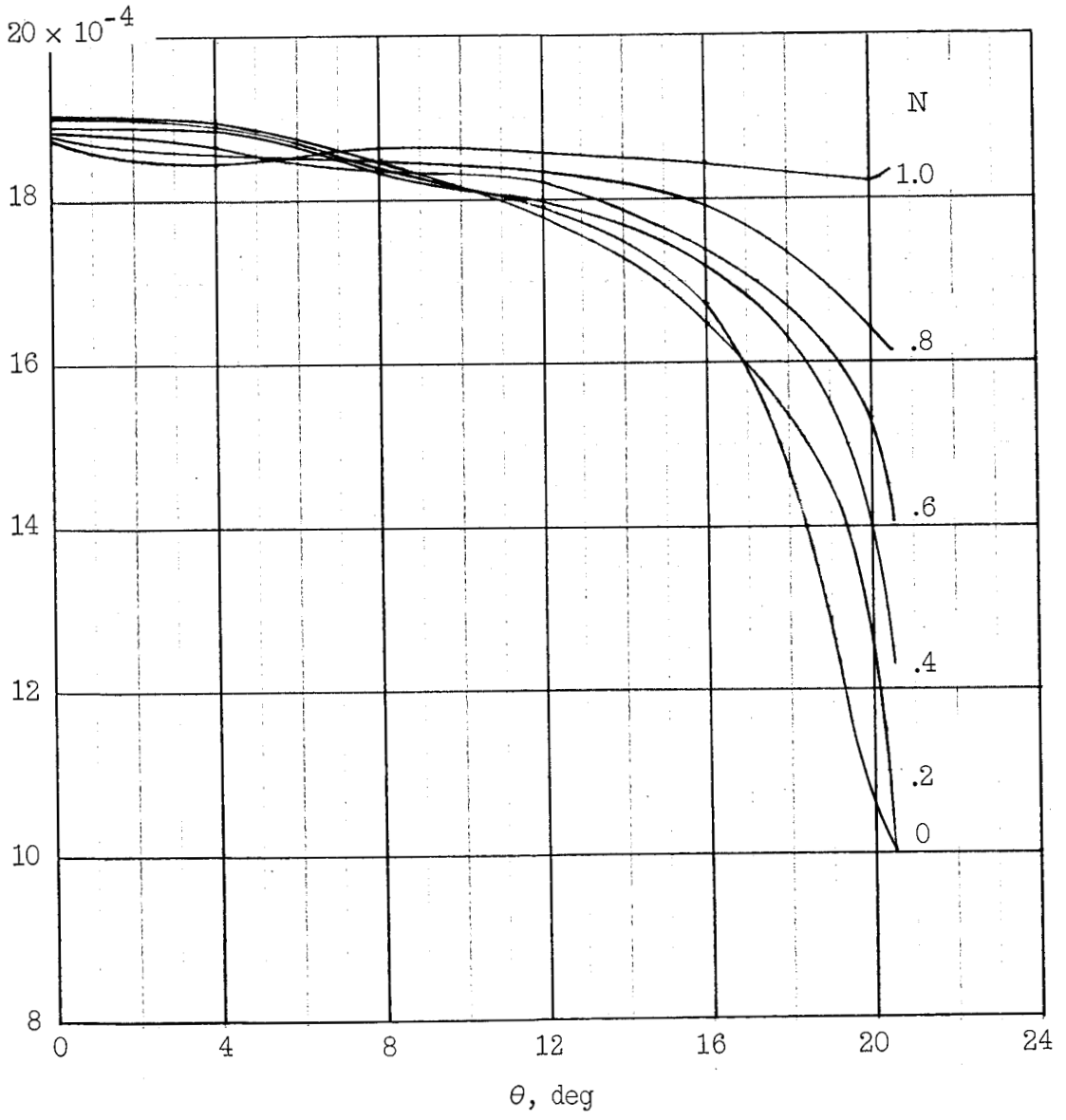

(b) Forebody density.

Figure 7.- Continued.

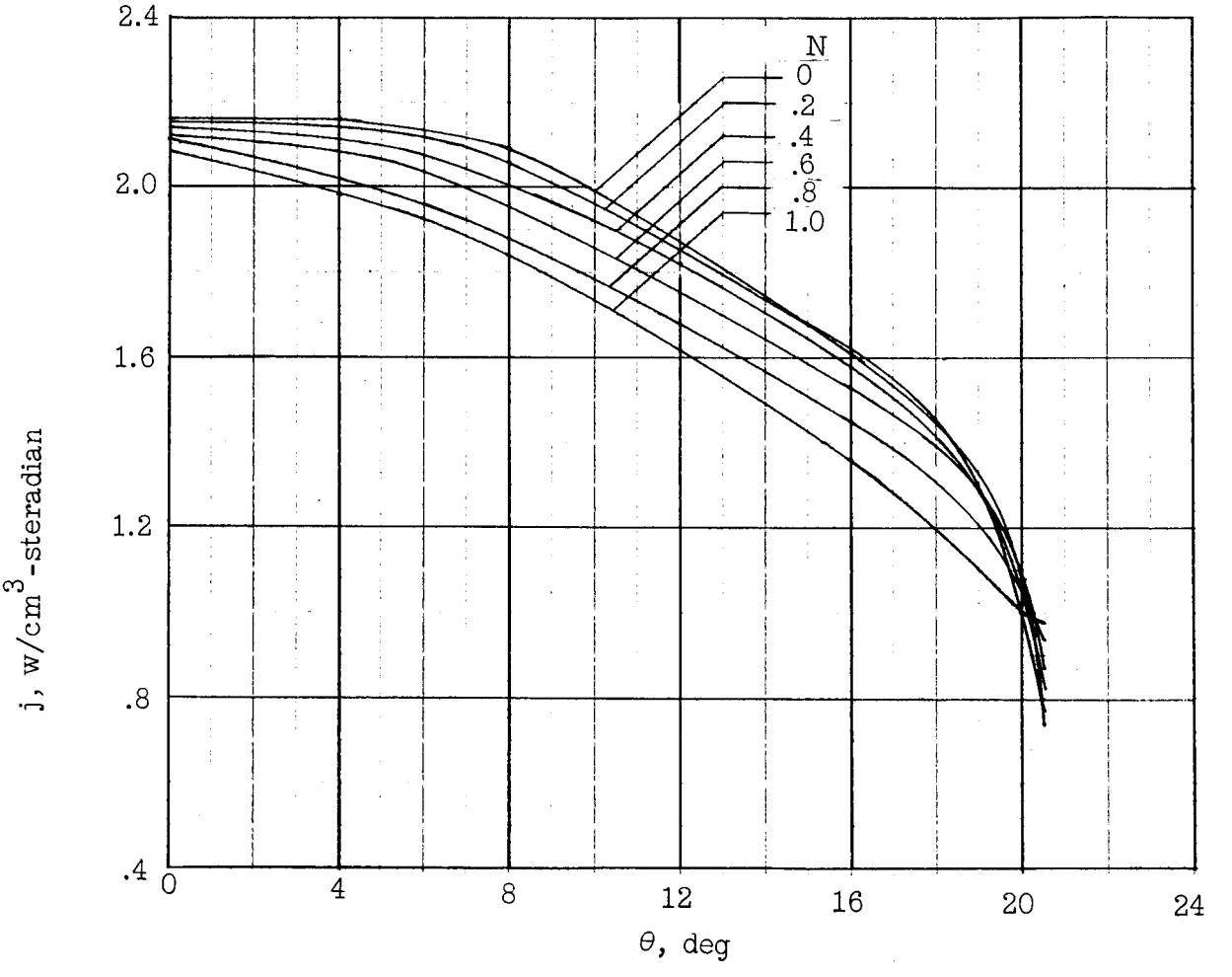

(c) Forebody specific radiation intensity.

Figure 7.- Continued.

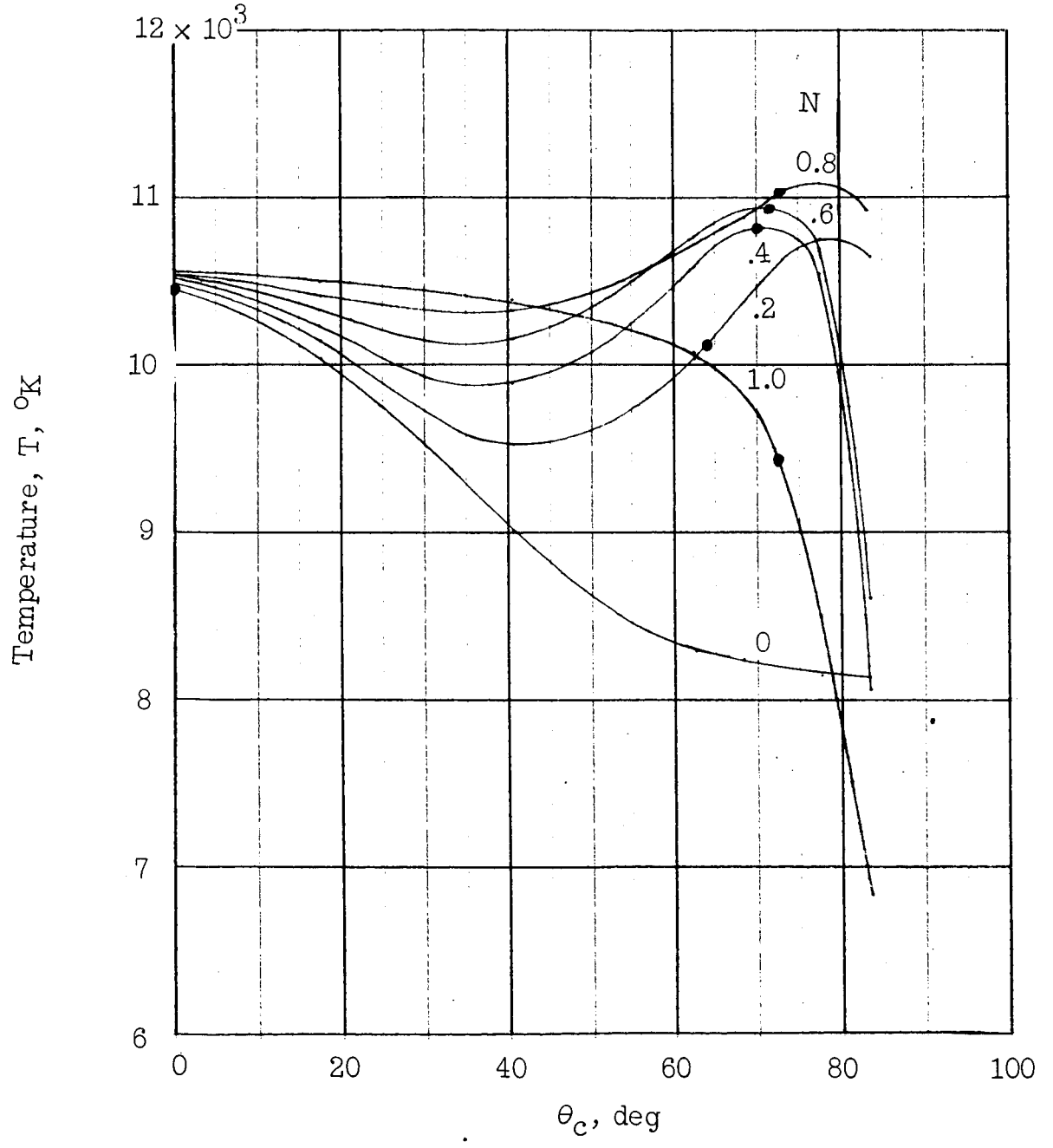

(d) Corner temperature.

Figure 7.- Continued.

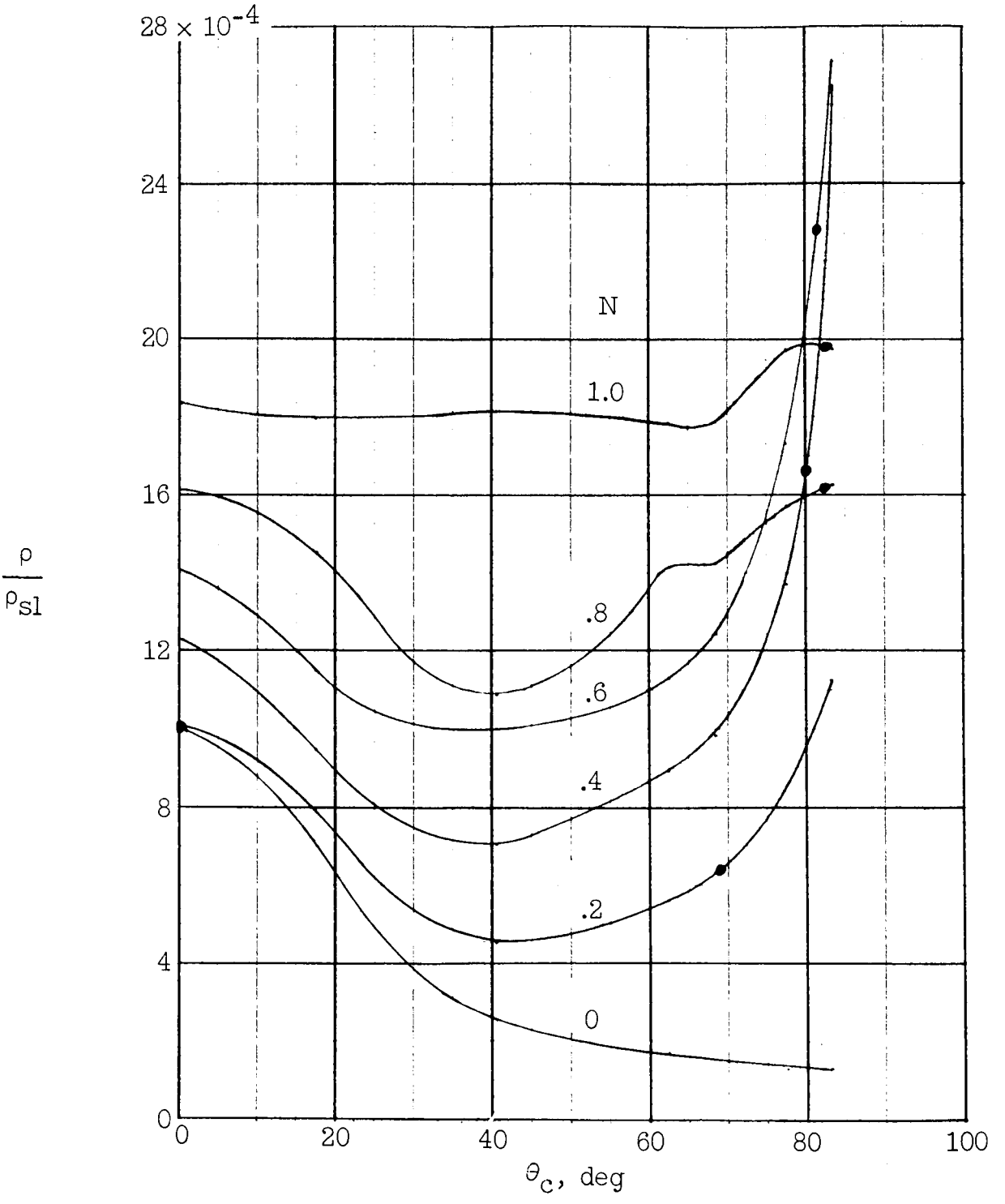

(e) Corner density.

Figure 7.- Continued.

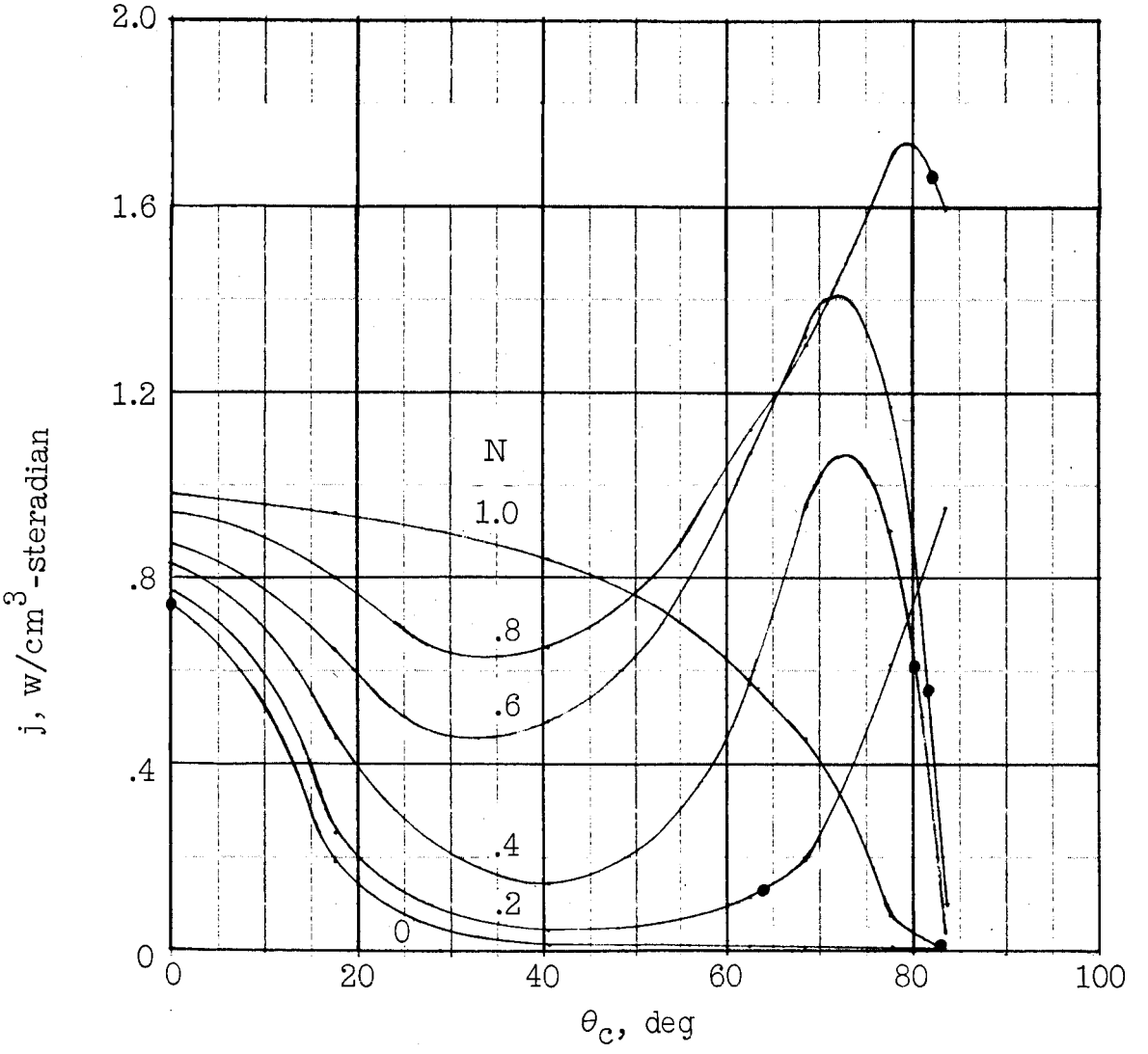

(f) Corner specific radiation intensity.

Figure 7.- Concluded.

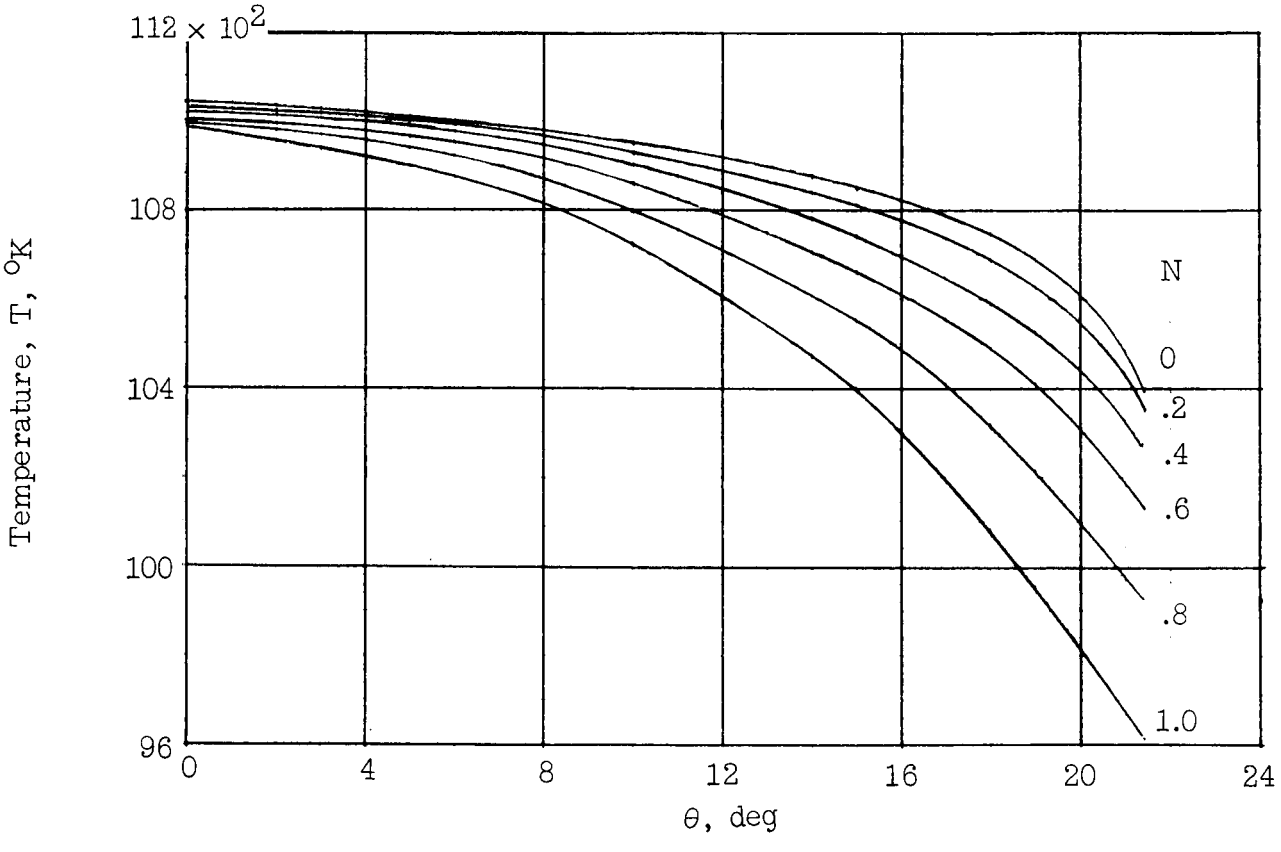

(a) Forebody temperature.

Figure 8.- Flow-field fluid properties for configuration 2. t = 25 sec; $\bar{h}$ = 166,000 ft; U_∞ = 34,800 ft/sec. (Dots denote limit of flow field viewed by forebody-corner tangency point.)

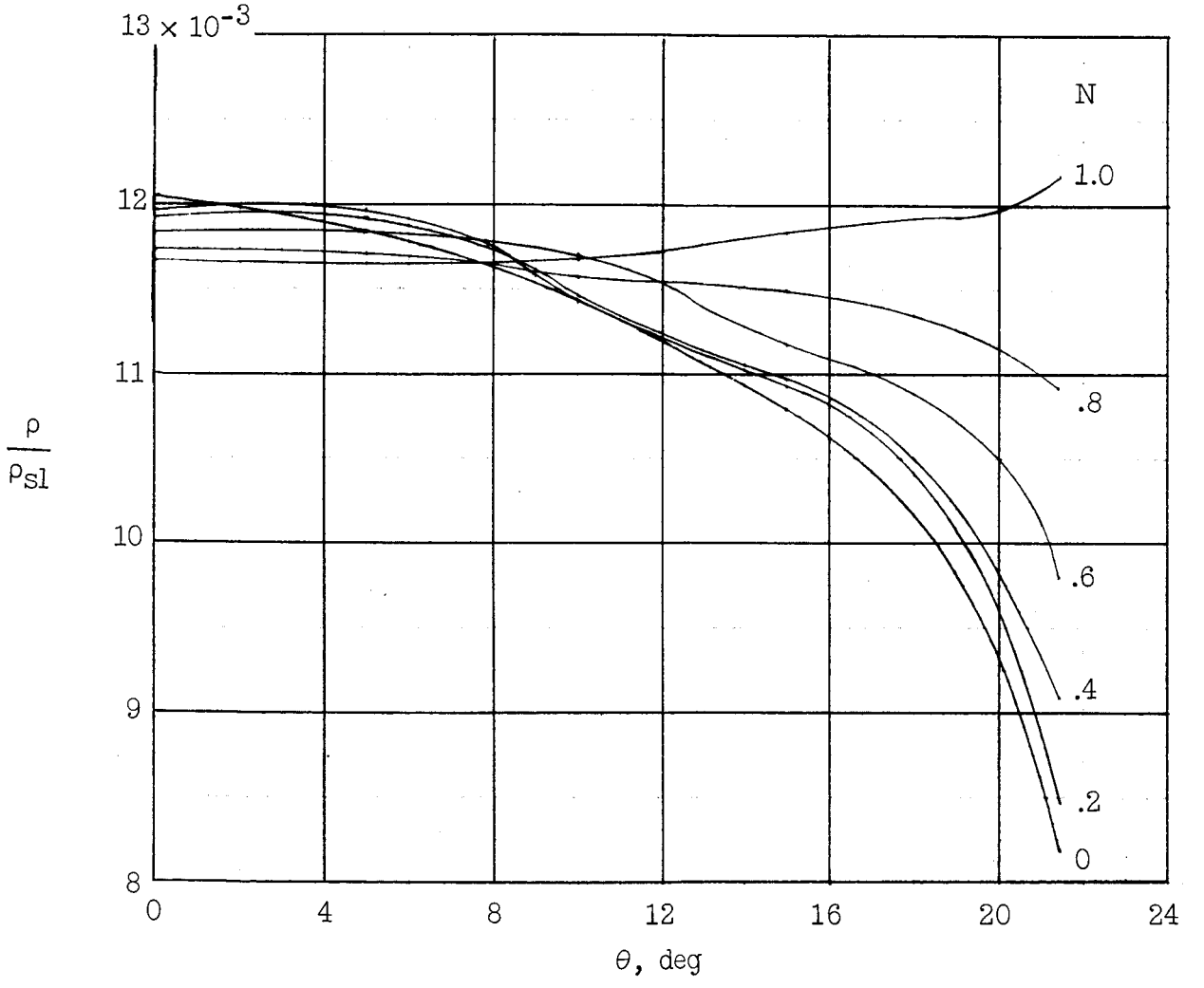

(b) Forebody density.

Figure 8.- Continued.

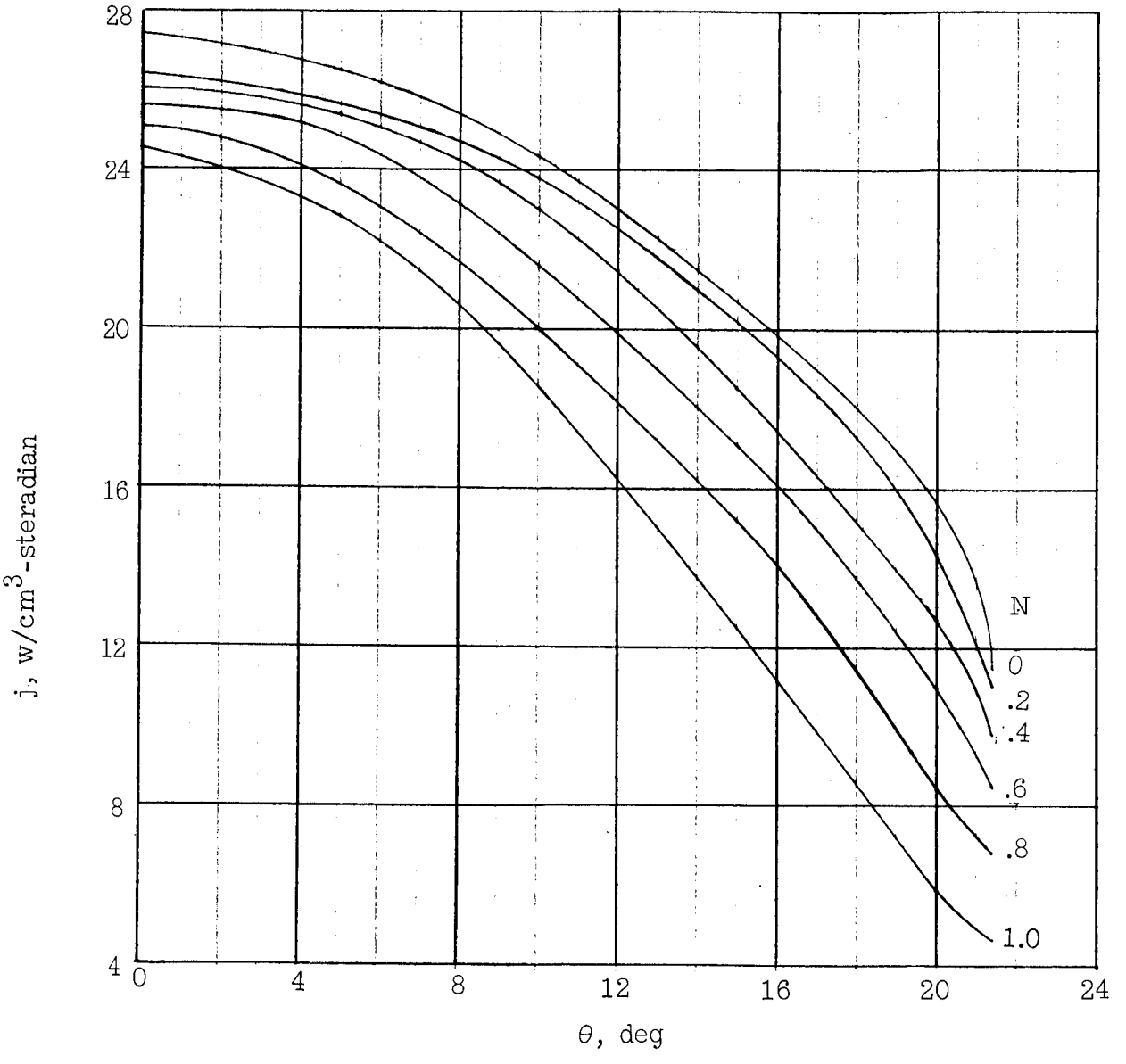

(c) Forebody specific radiation intensity.

Figure 8.- Continued.

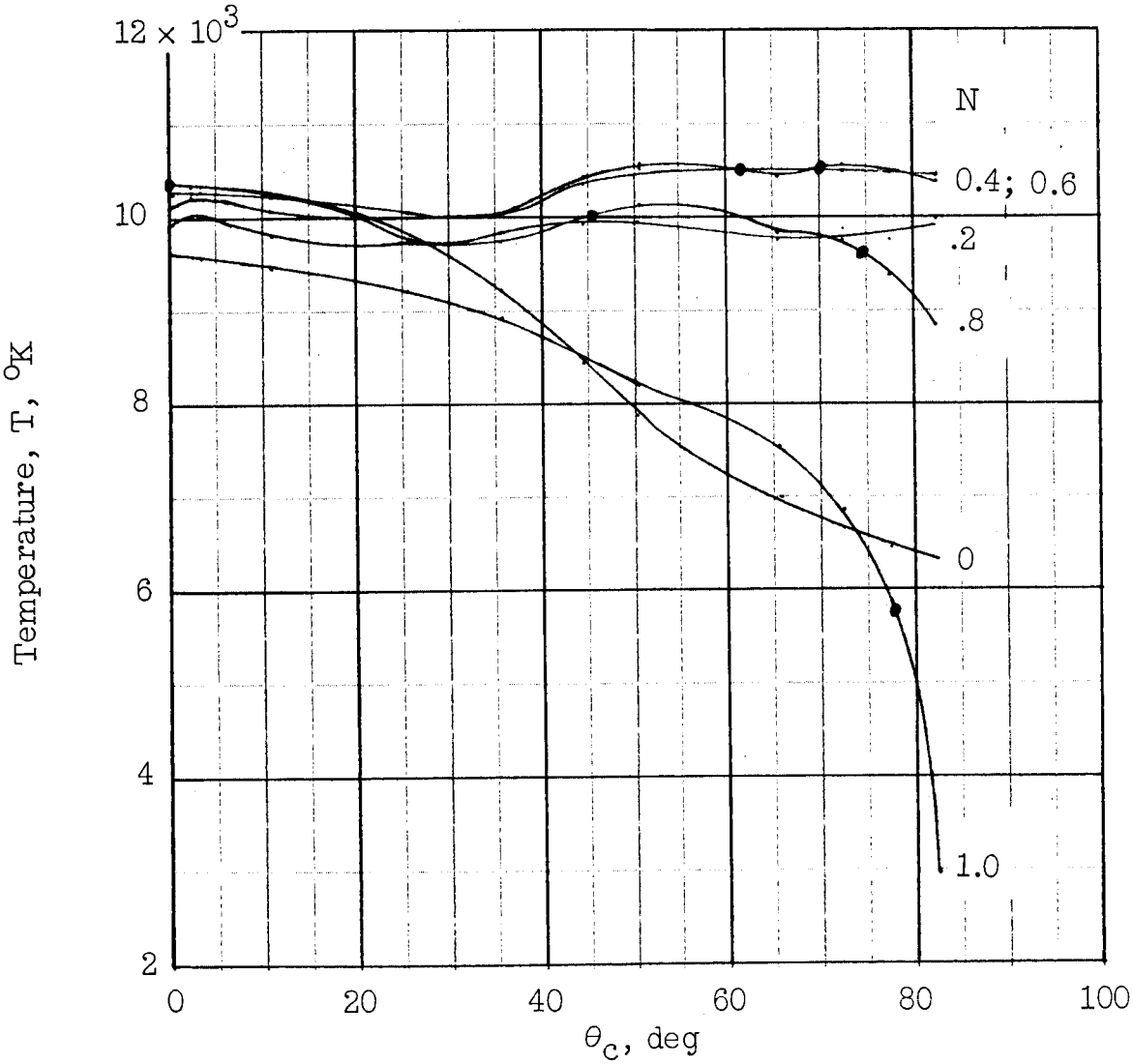

(d) Corner temperature.

Figure 8.- Continued.

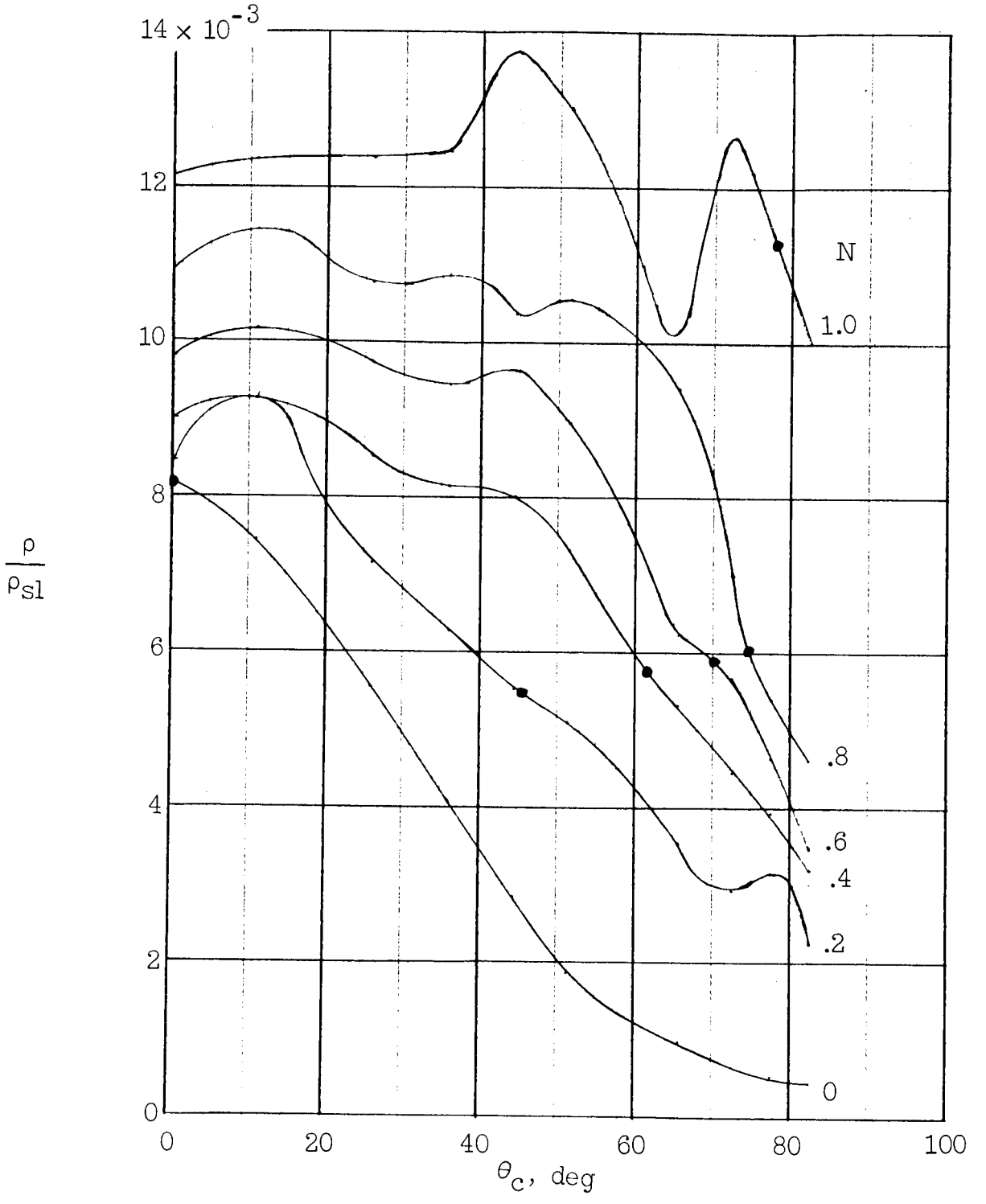

(e) Corner density.

Figure 8.- Continued.

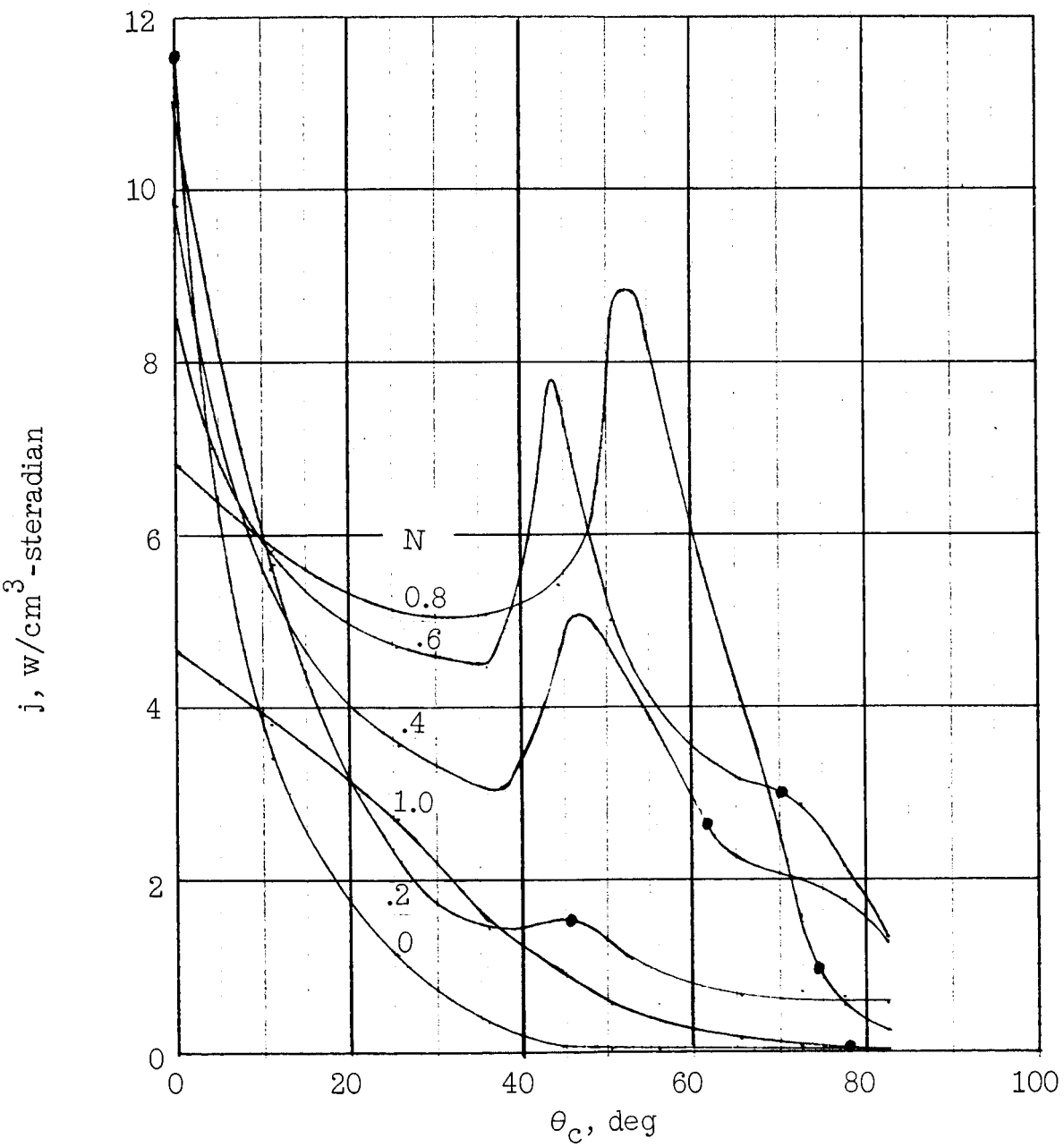

(f) Corner specific radiation intensity.

Figure 8.- Concluded.

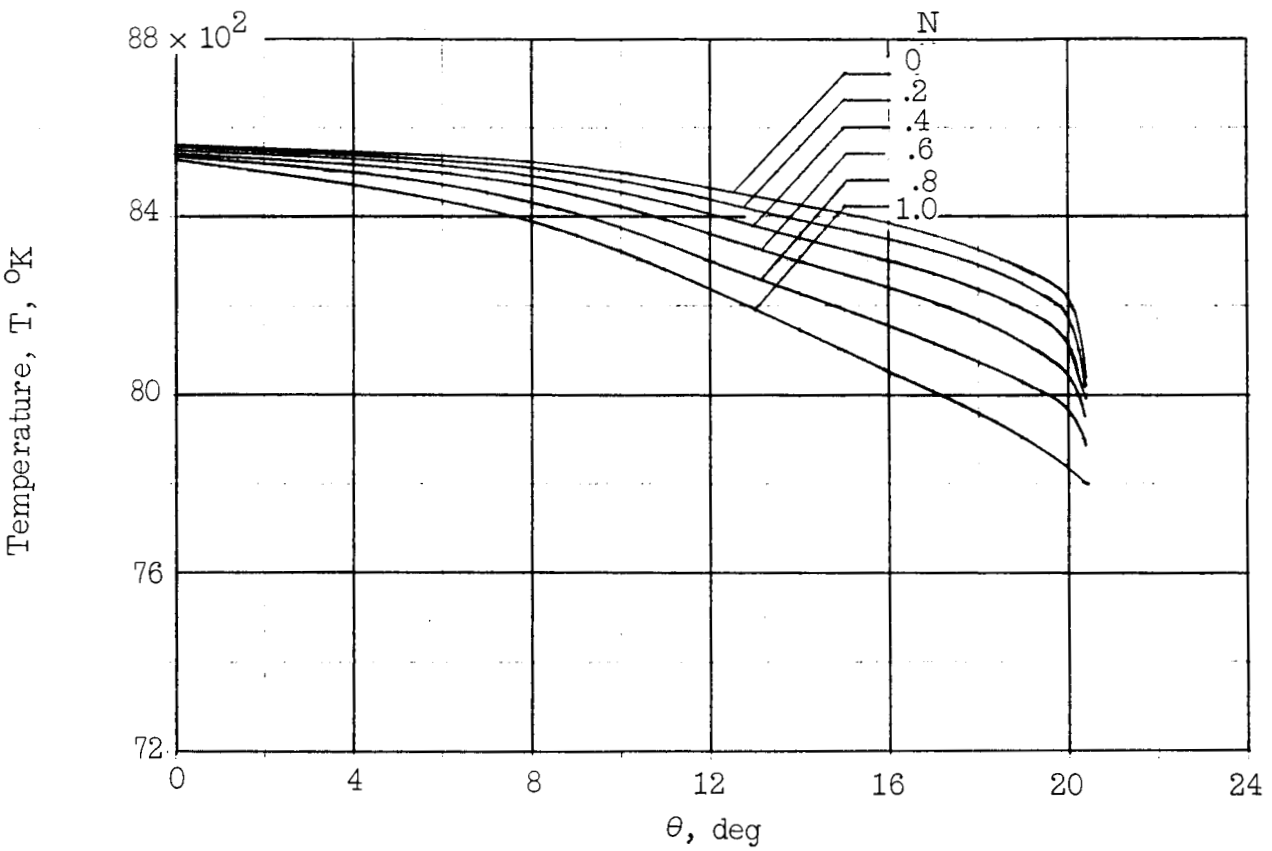

(a) Forebody temperature.

Figure 9.- Flow-field fluid properties for configuration 2. t = 27.6 sec; $\bar{h}$ = 147,000 ft; U_∞ = 30,100 ft/sec. (Dots denote limit of flow field viewed by forebody-corner tangency point.)

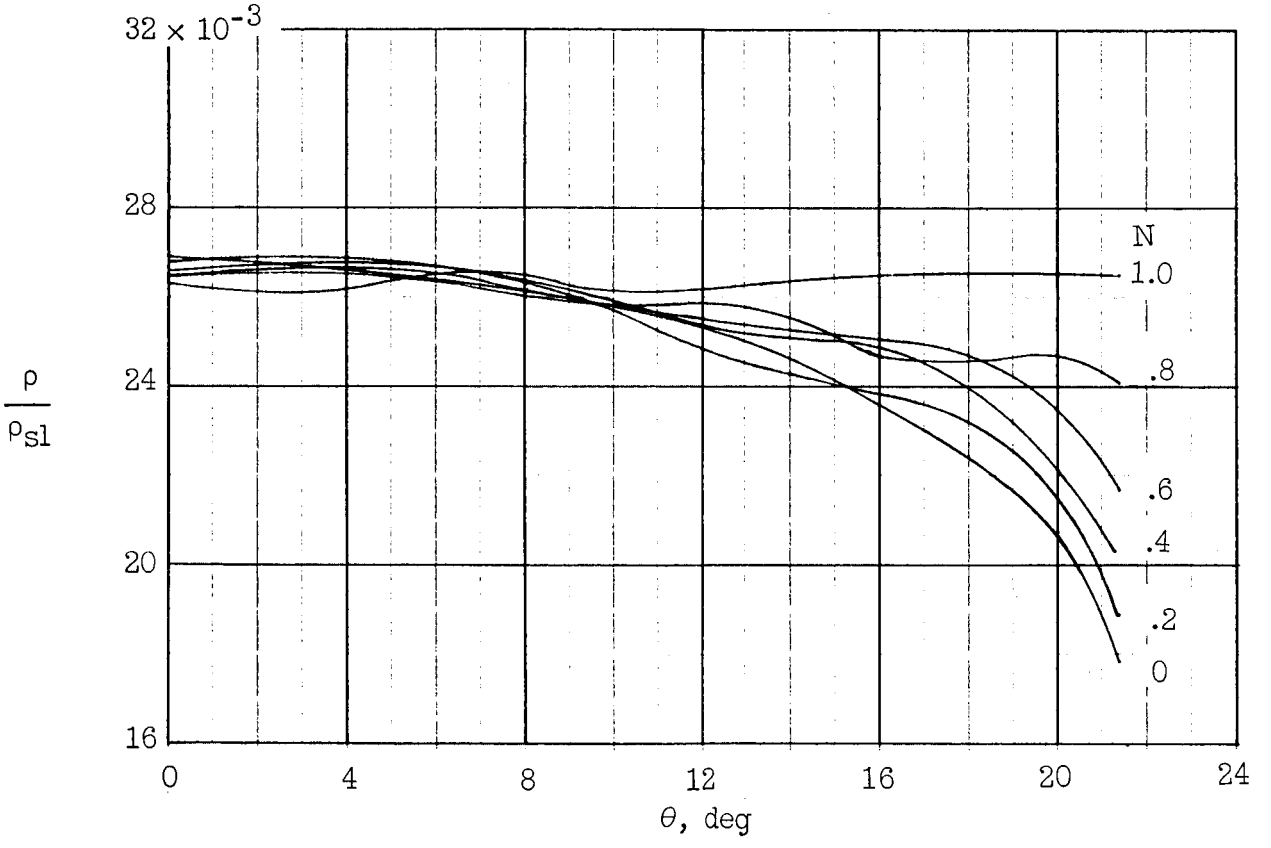

(b) Forebody density.

Figure 9.- Continued.

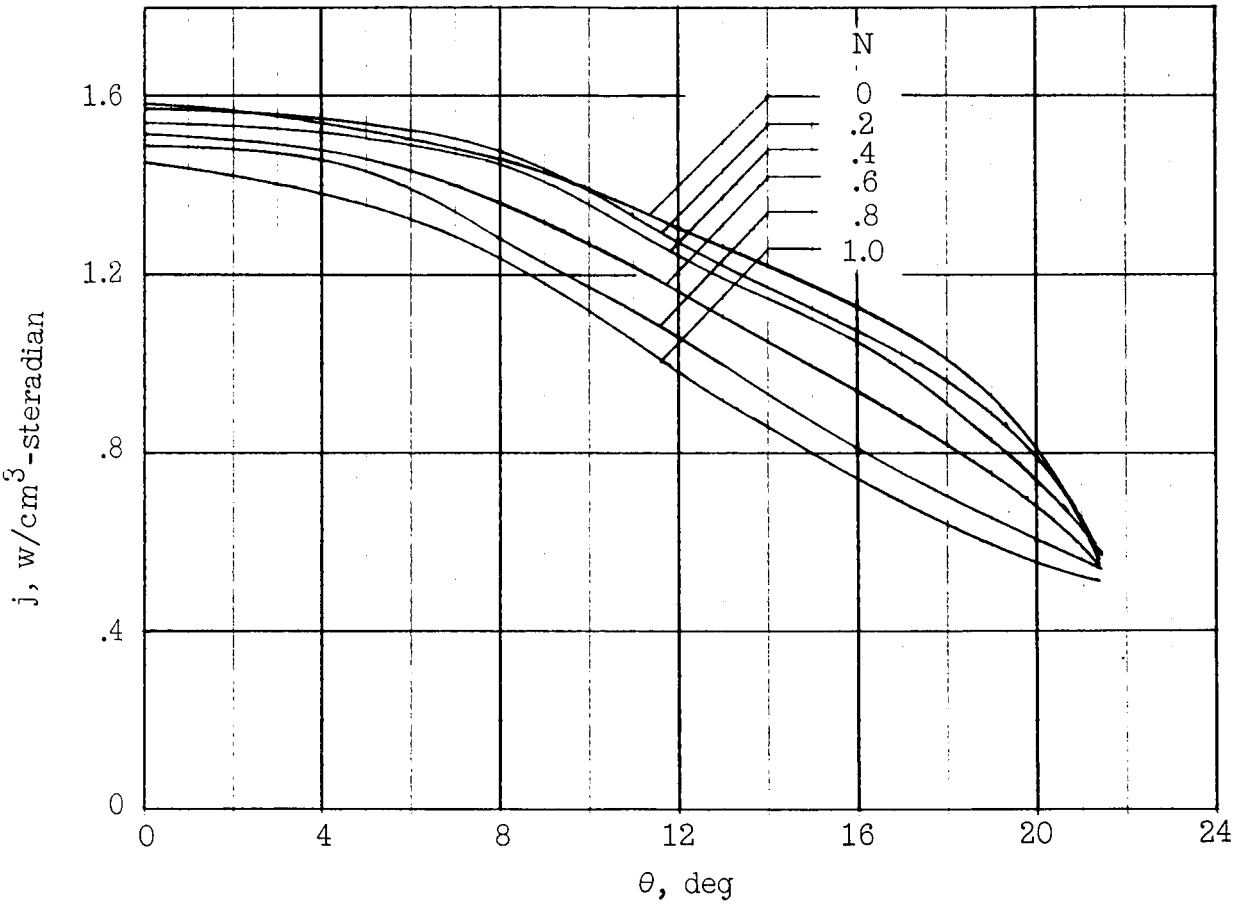

(c) Forebody specific radiation intensity.

Figure 9.- Continued.

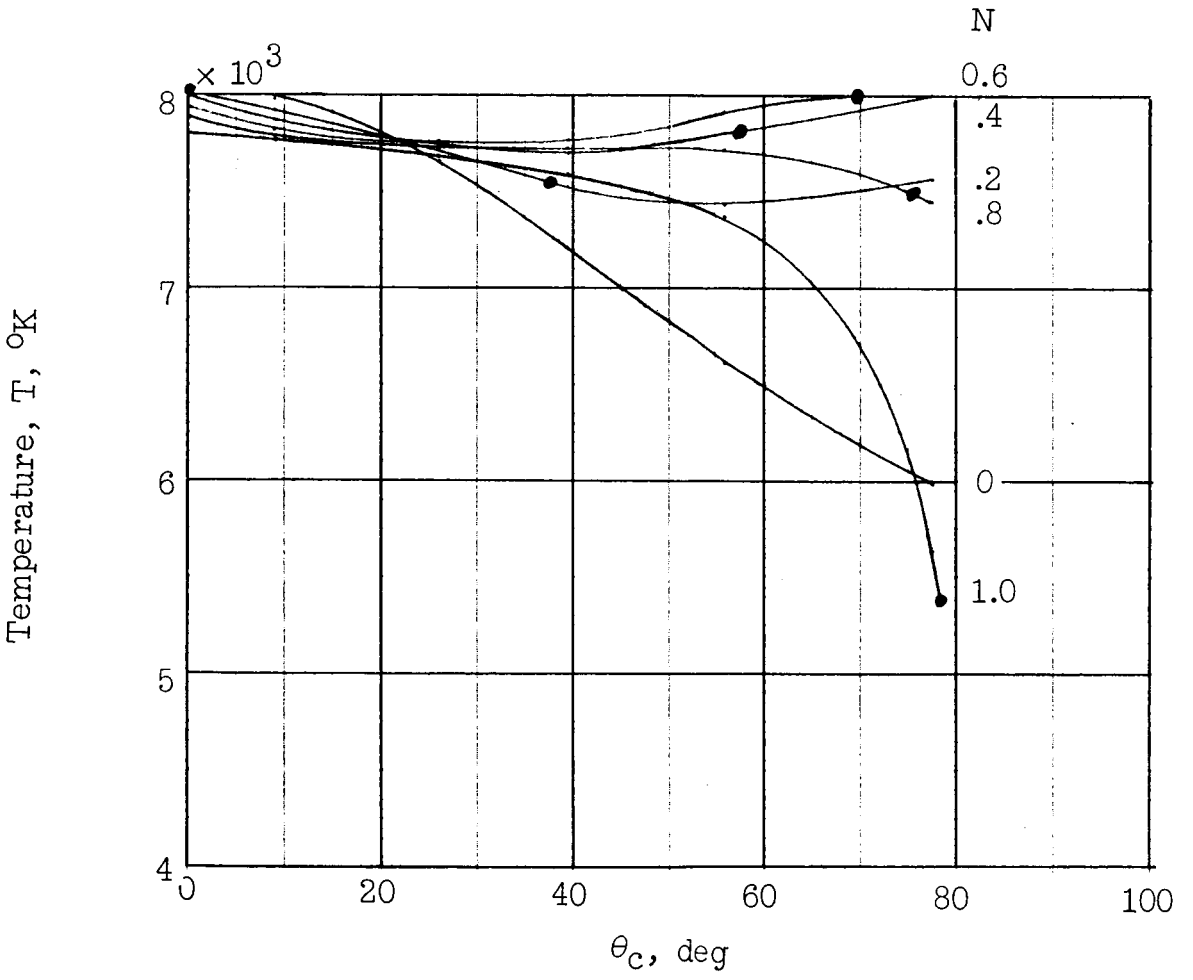

(d) Corner temperature.

Figure 9.- Continued.

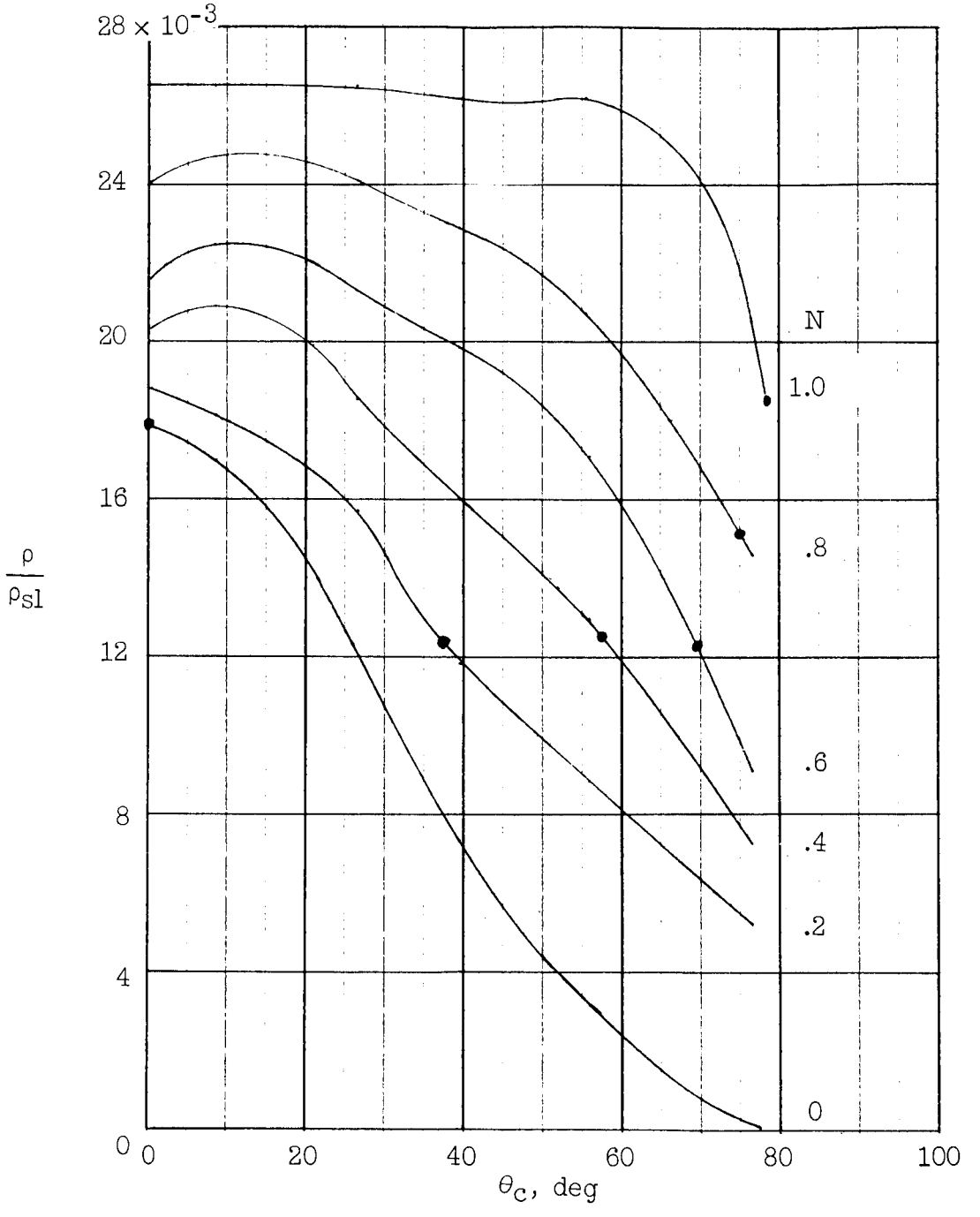

(e) Corner density.

Figure 9.- Continued.

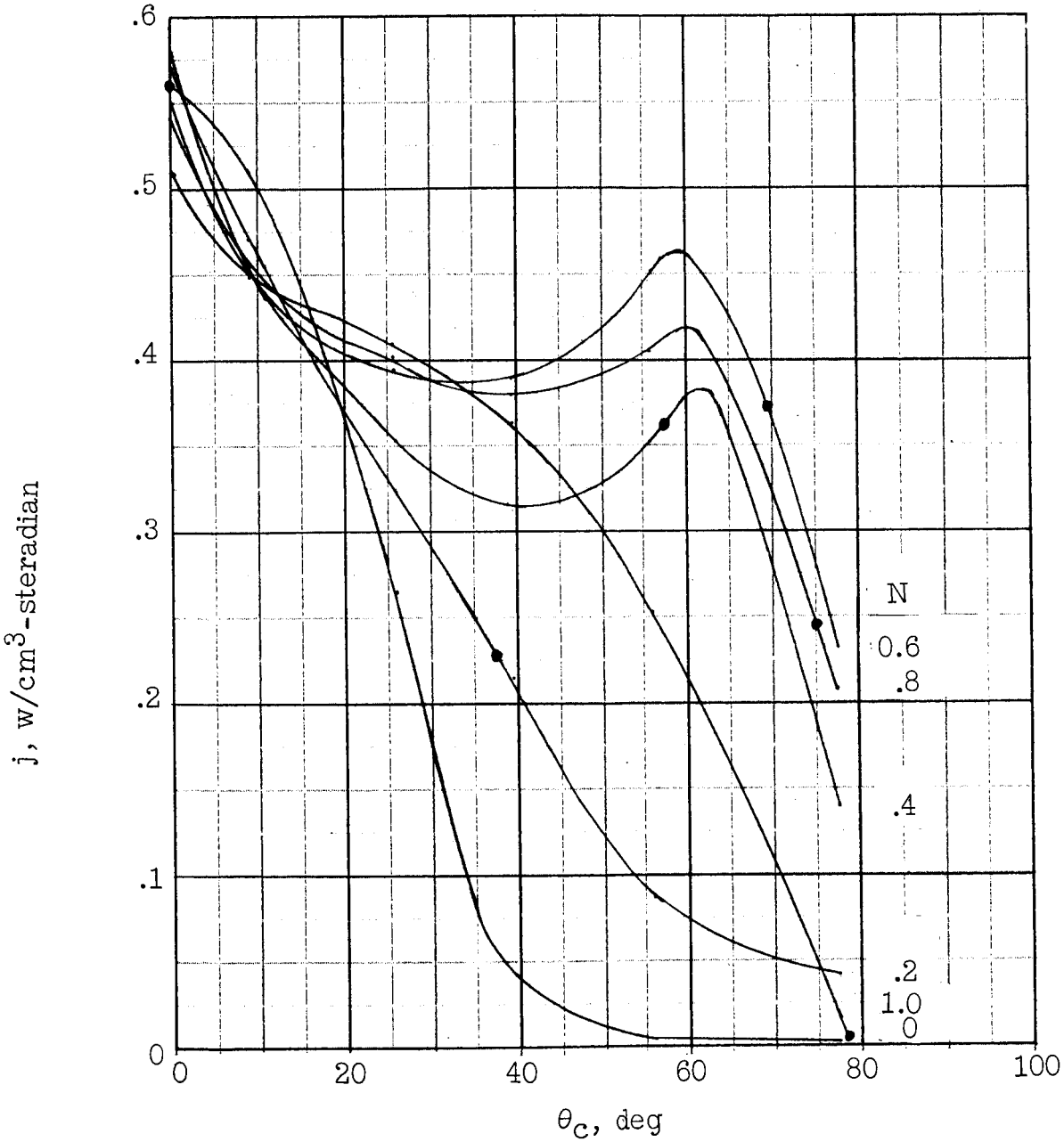

(f) Corner specific radiation intensity.

Figure 9.- Concluded.

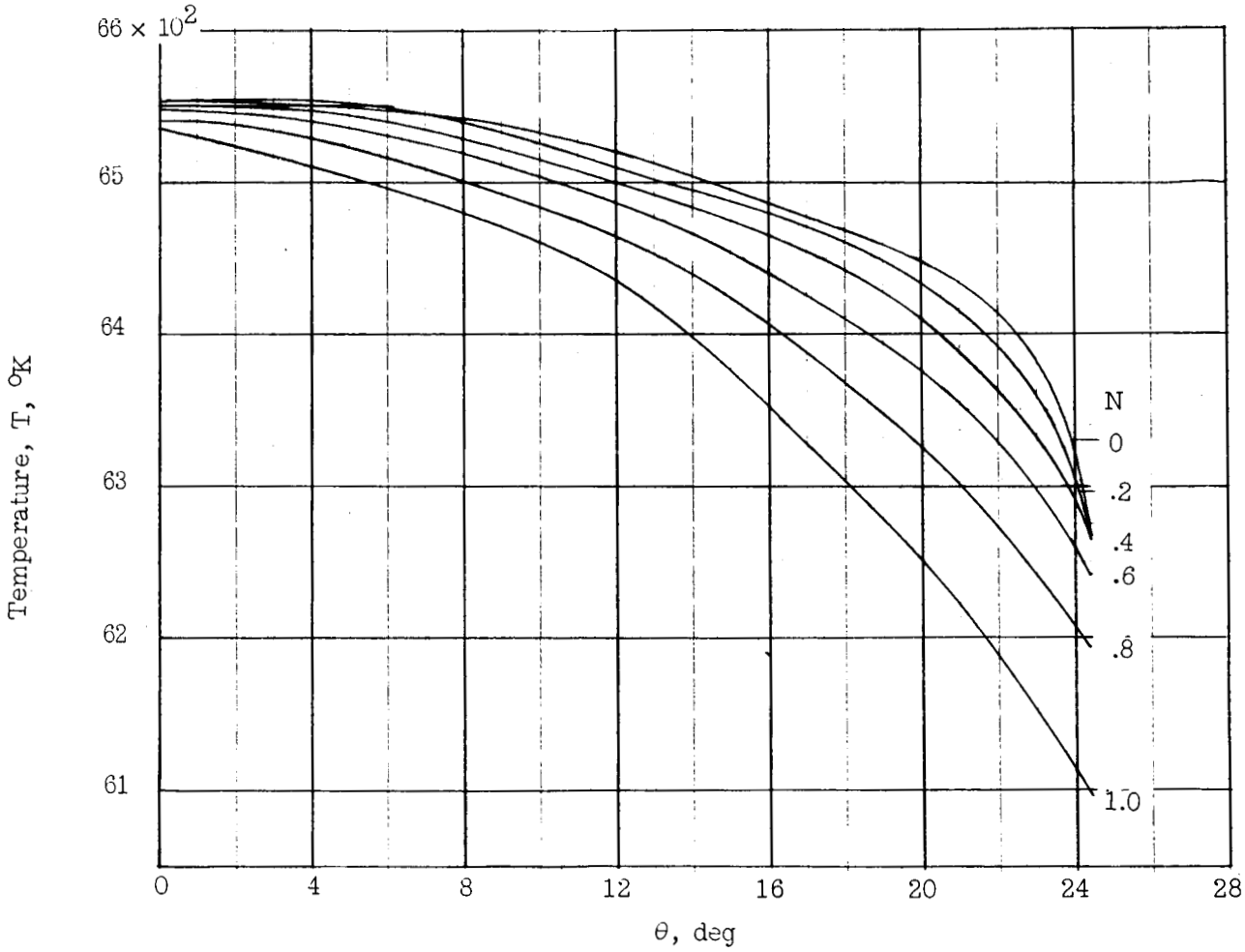

(a) Forebody temperature.

Figure 10.- Flow-field fluid properties for configuration 3. t = 32 sec; $\bar{h}$ = 120,000 ft; U_∞ = 19,500 ft/sec. (Dots denote limit of flow field viewed by forebody-corner tangency point.)

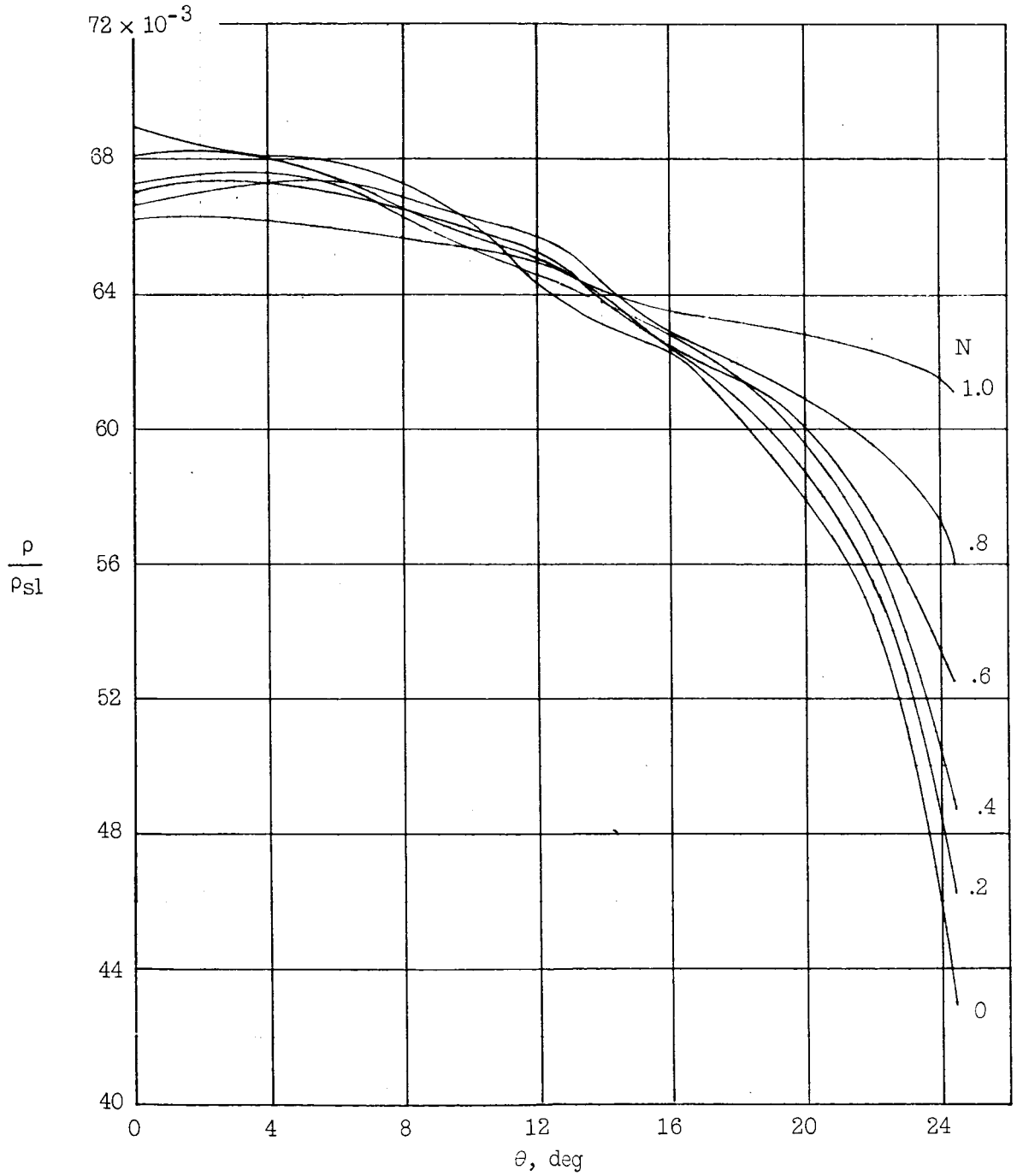

(b) Forebody density.

Figure 10.- Continued.

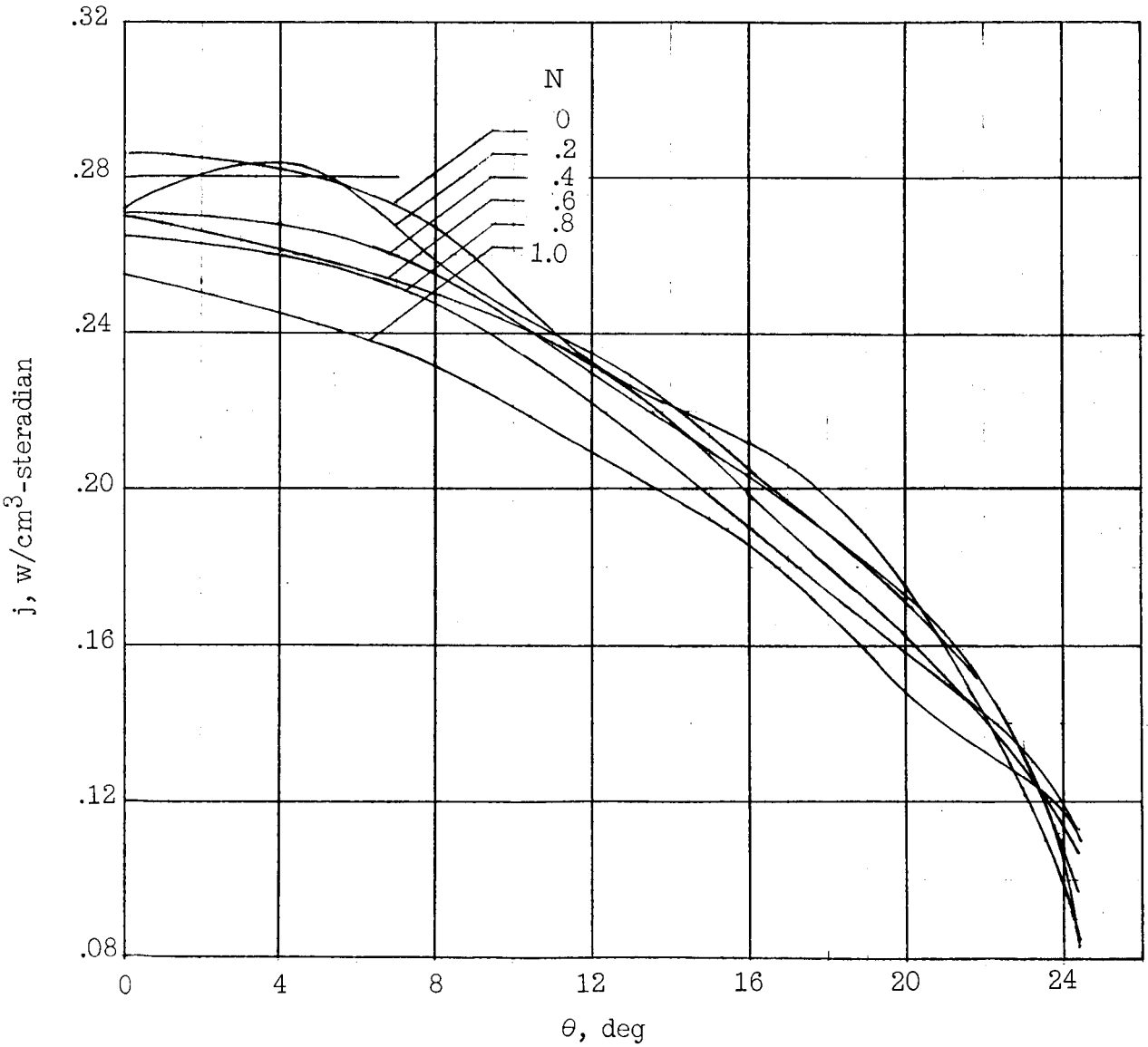

(c) Forebody specific radiation intensity.

Figure 10.- Continued.

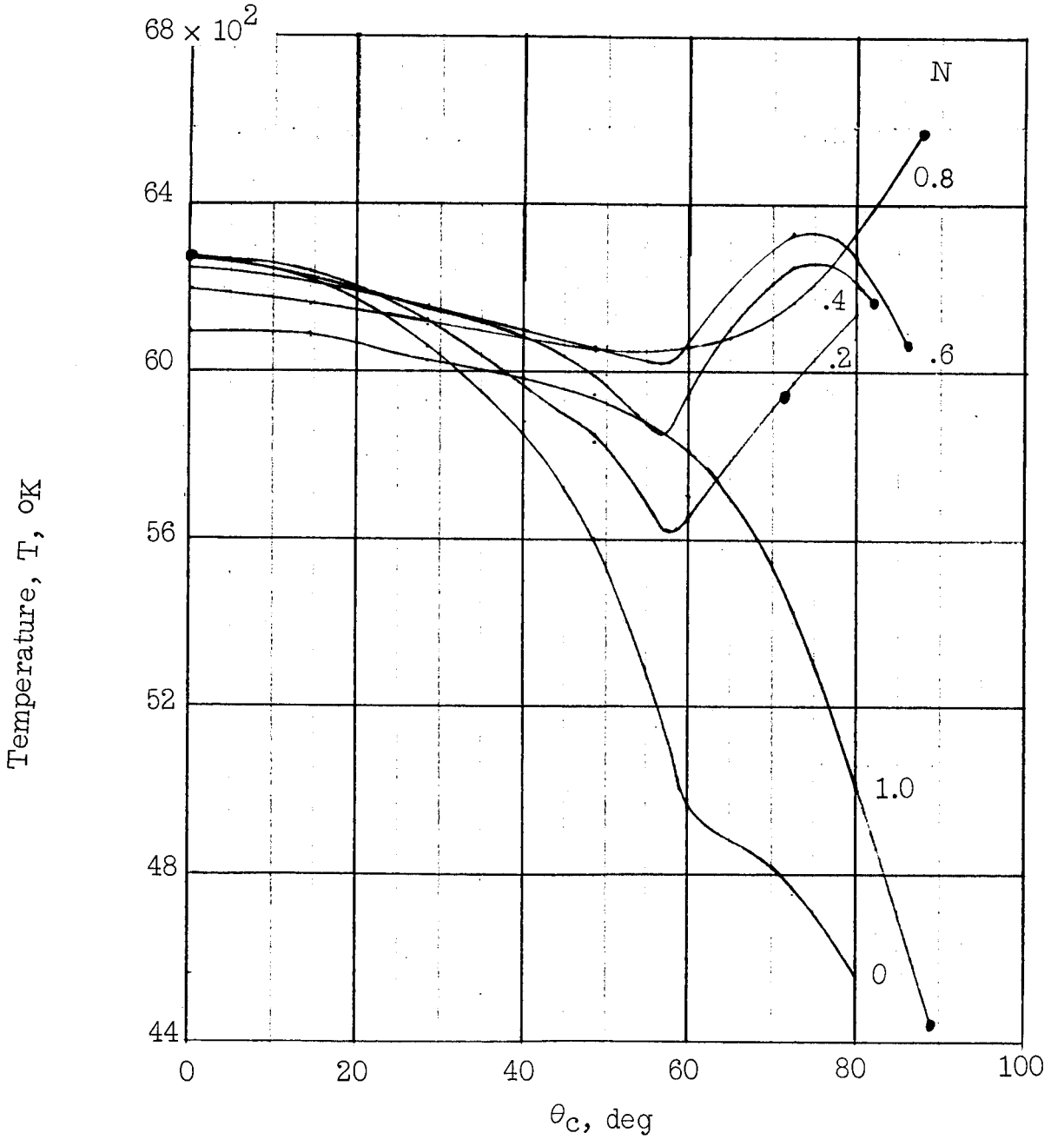

(d) Corner temperature.

Figure 10.- Continued.

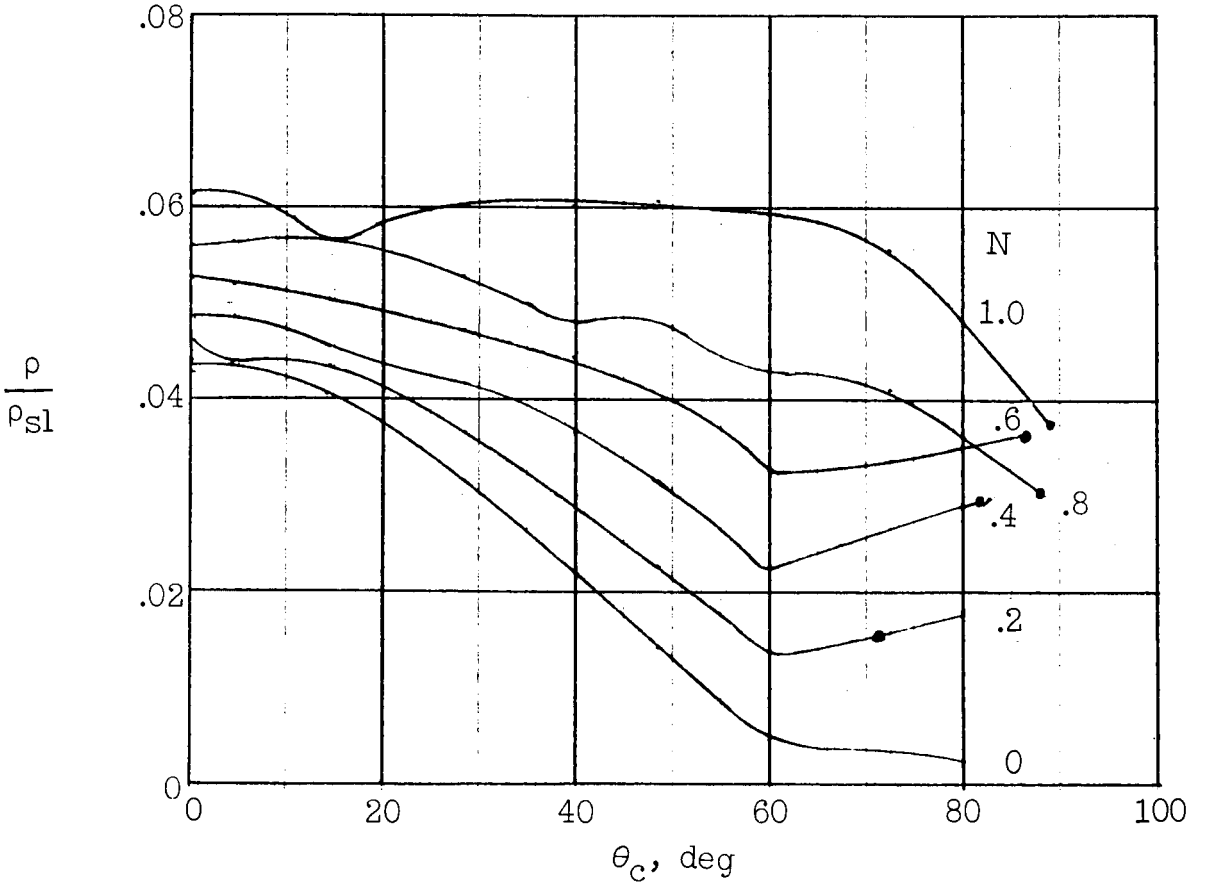

(e) Corner density.

Figure 10.- Continued.

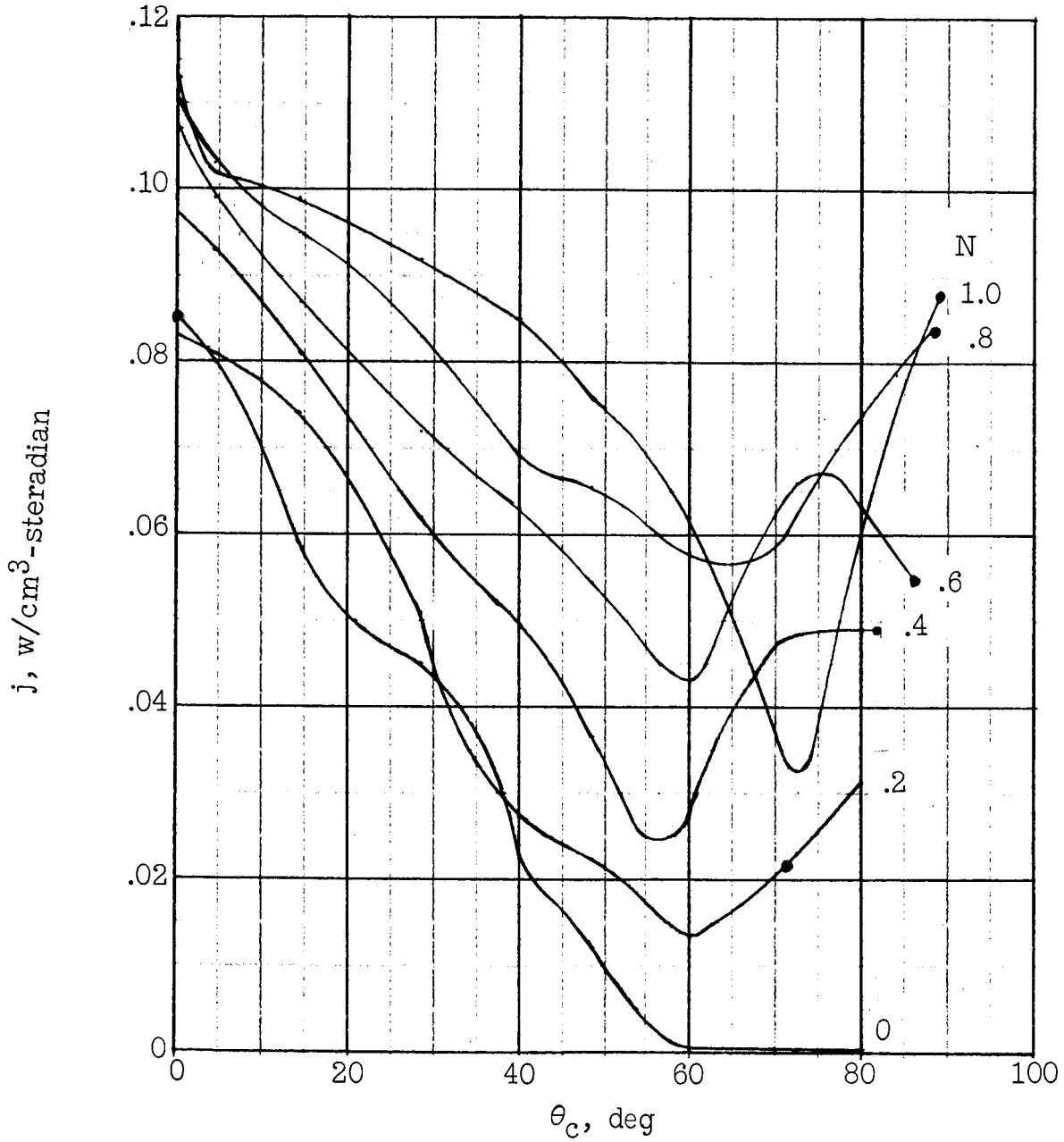

(f) Corner specific radiation intensity.

Figure 10.- Concluded.

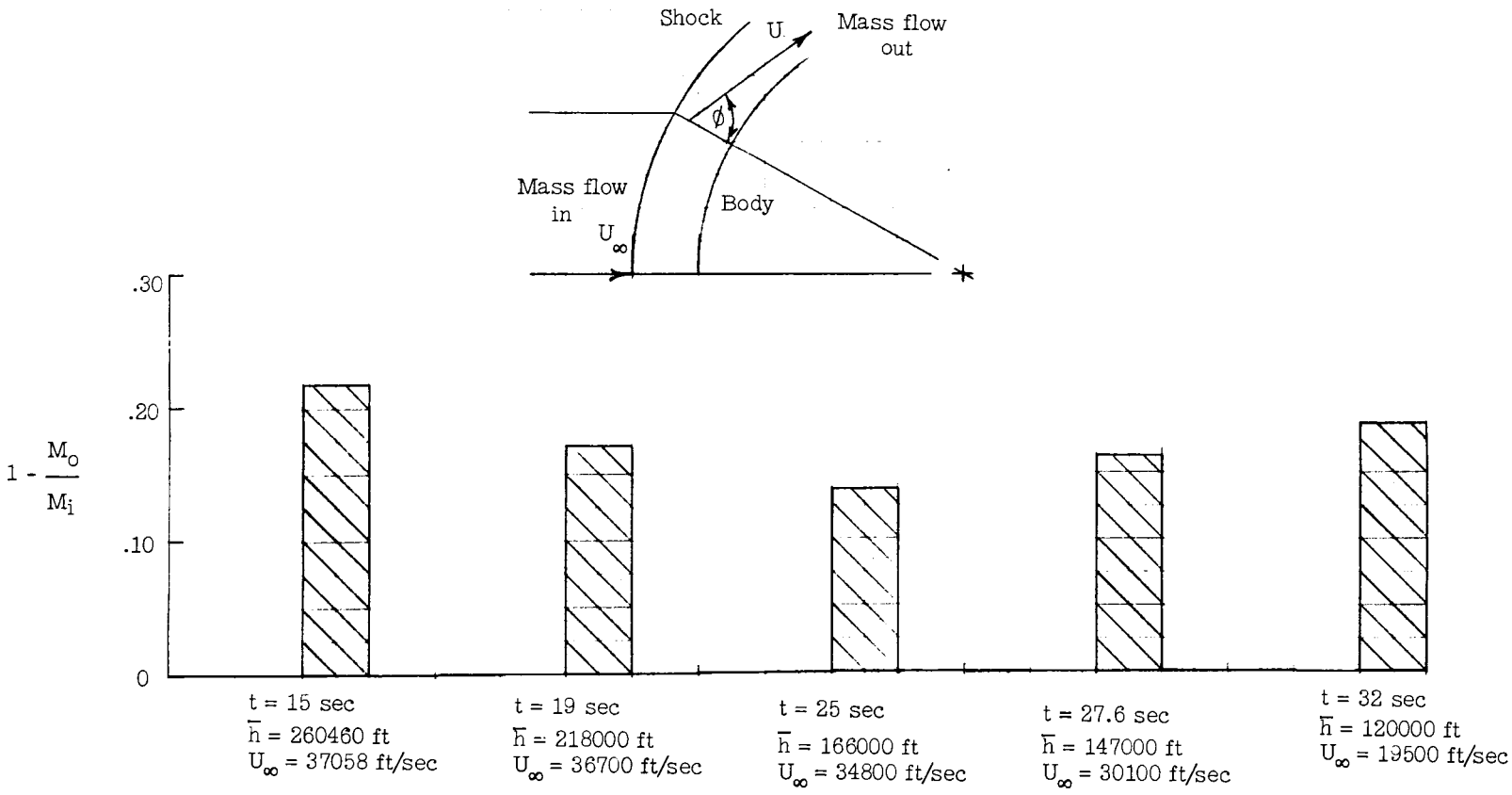

Figure 11.- Mass-flow balance for shock layer. $\theta = 15^\circ$.

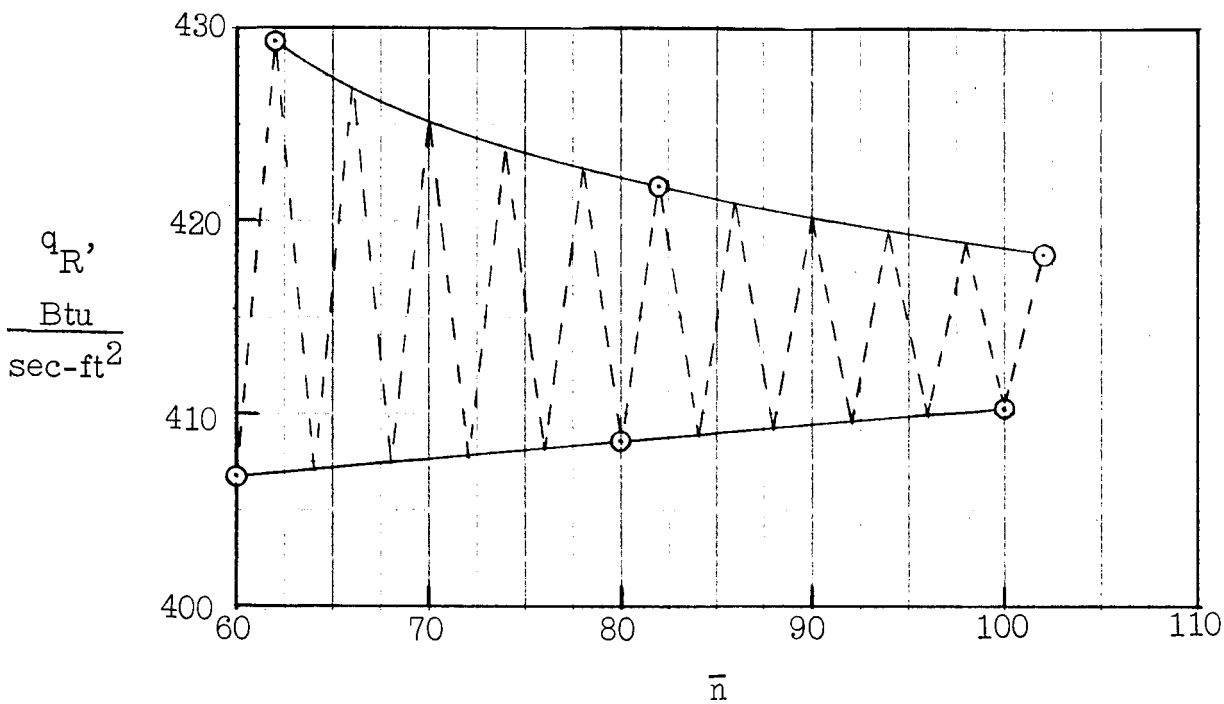

Figure 12.- Convergence of radiation heating equation. t = 25 sec; $\bar{h}$ = 166,000 ft; U_∞ = 34,800 ft/sec; θ_p = 0.

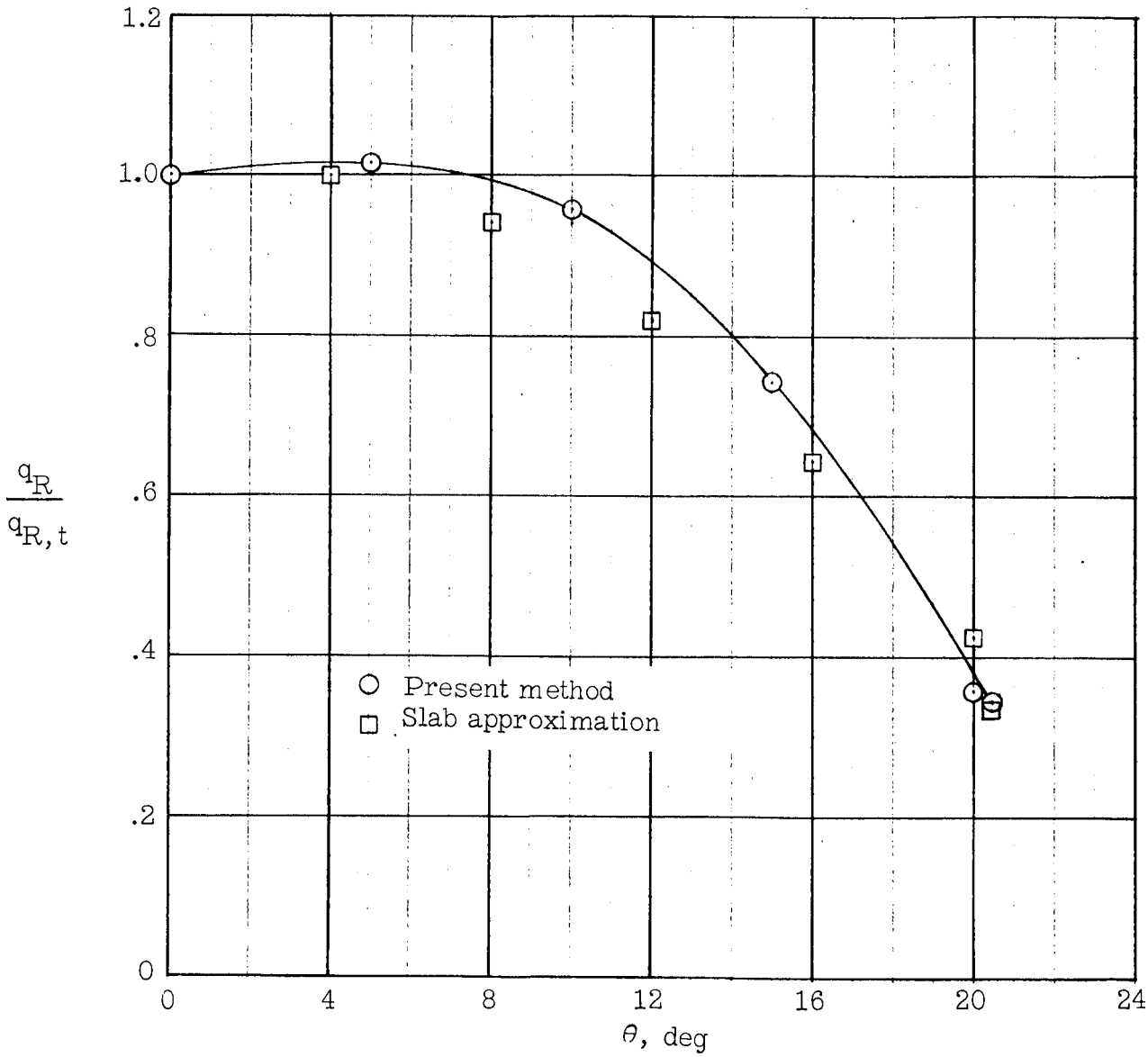

(a) t = 15 sec; $\bar{h}$ = 260,460 ft; U_∞ = 37,058 ft/sec.

Figure 13.- Radiation heat-transfer distribution.

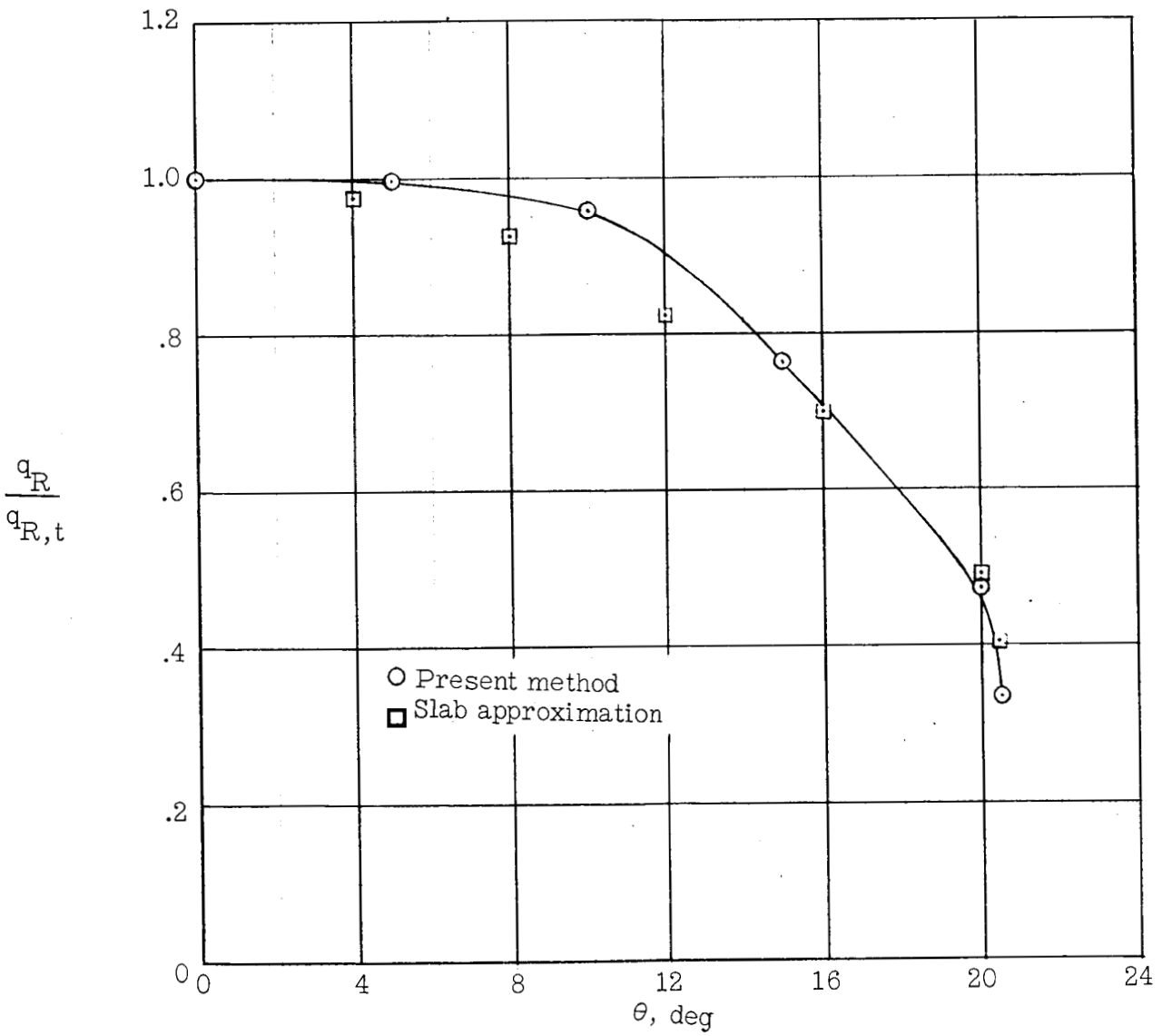

(b) t = 19 sec; $\bar{h}$ = 218,000 ft; U_∞ = 36,700 ft/sec.

Figure 13.- Continued.

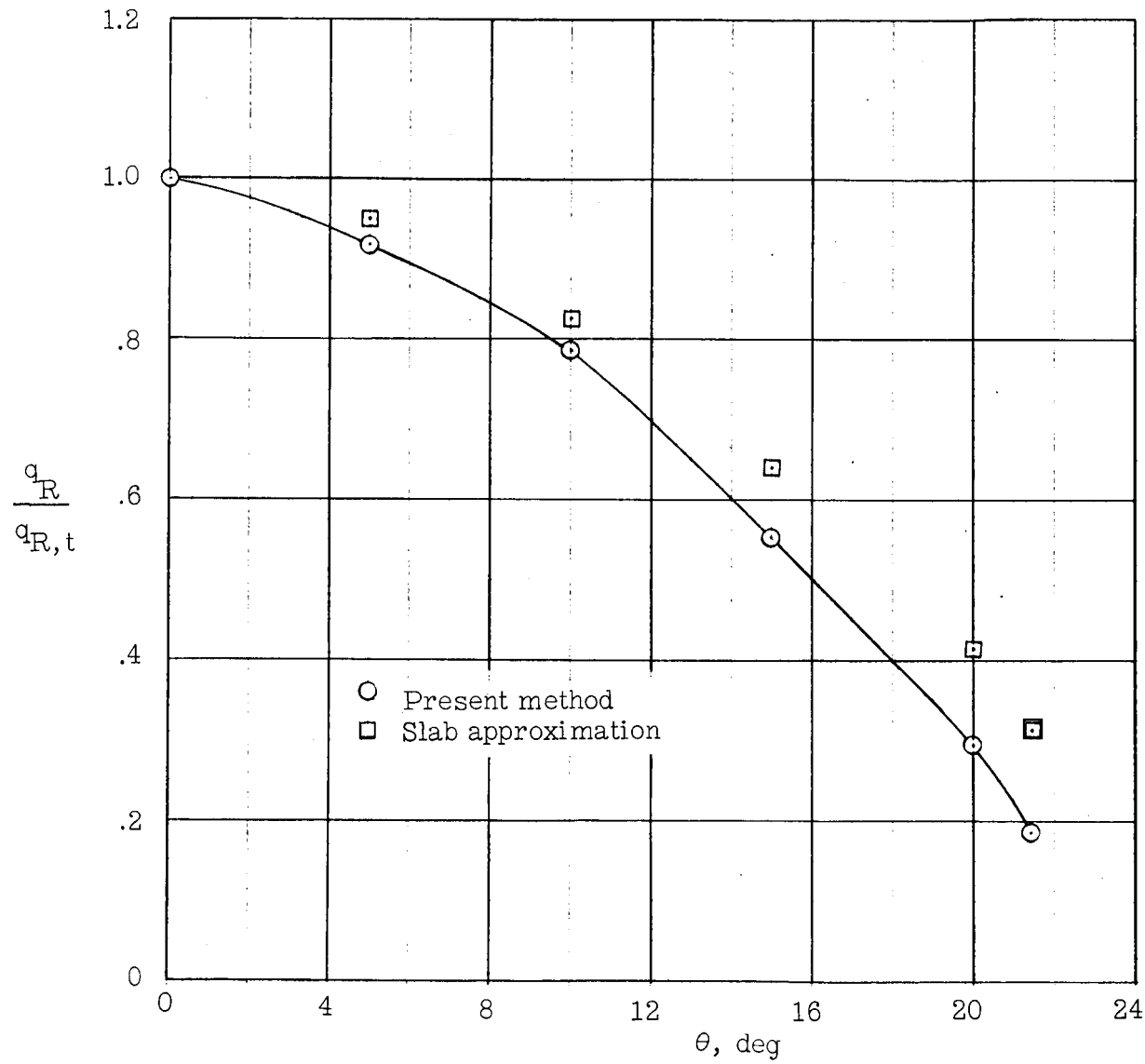

(c) t = 25 sec; $\bar{h}$ = 166,000 ft; U_∞ = 34,800 ft/sec.

Figure 13.- Continued.

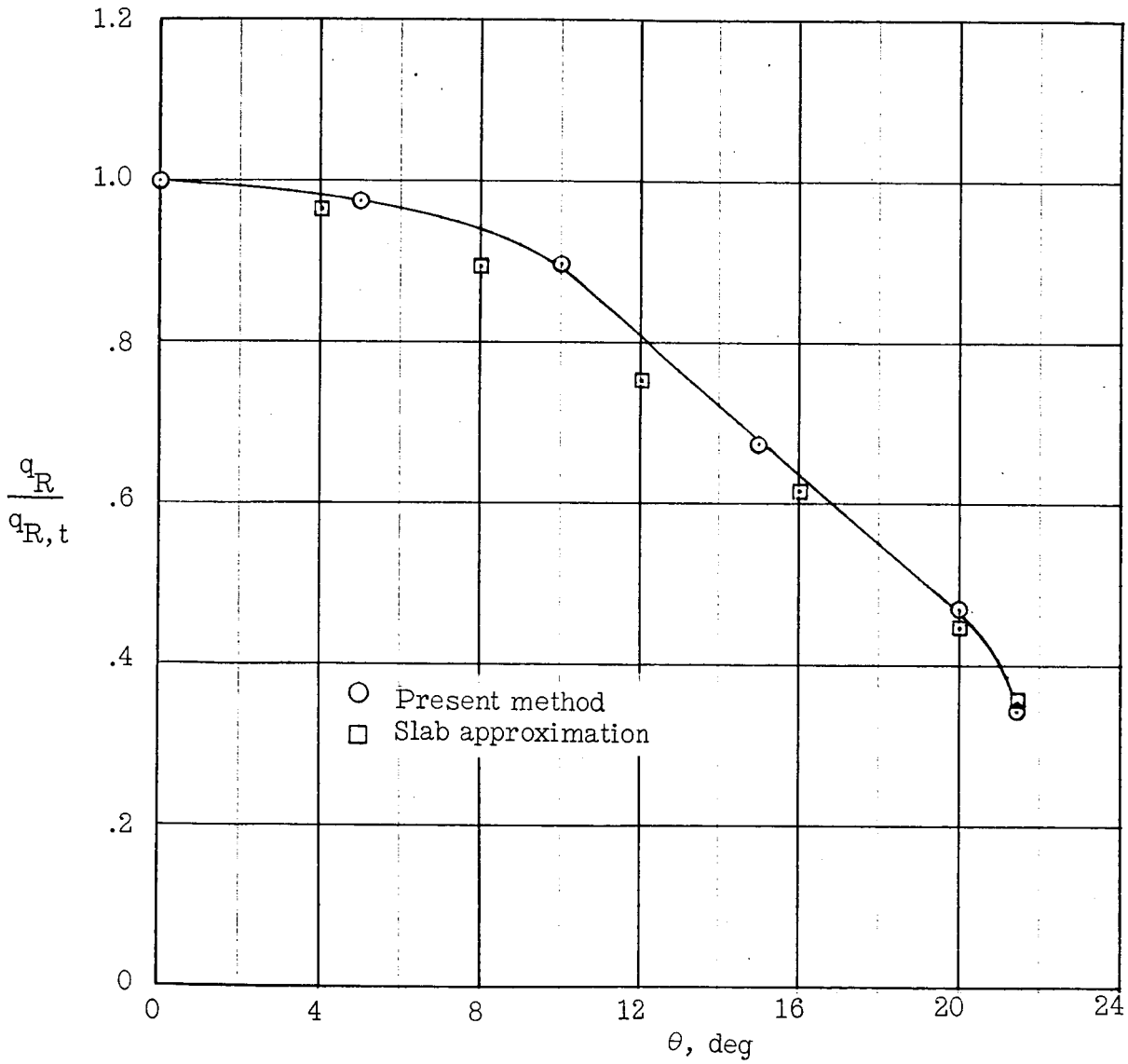

(d) t = 27.6 sec; $\bar{h}$ = 147,000 ft; U_∞ = 31,100 ft/sec.

Figure 13.- Continued.

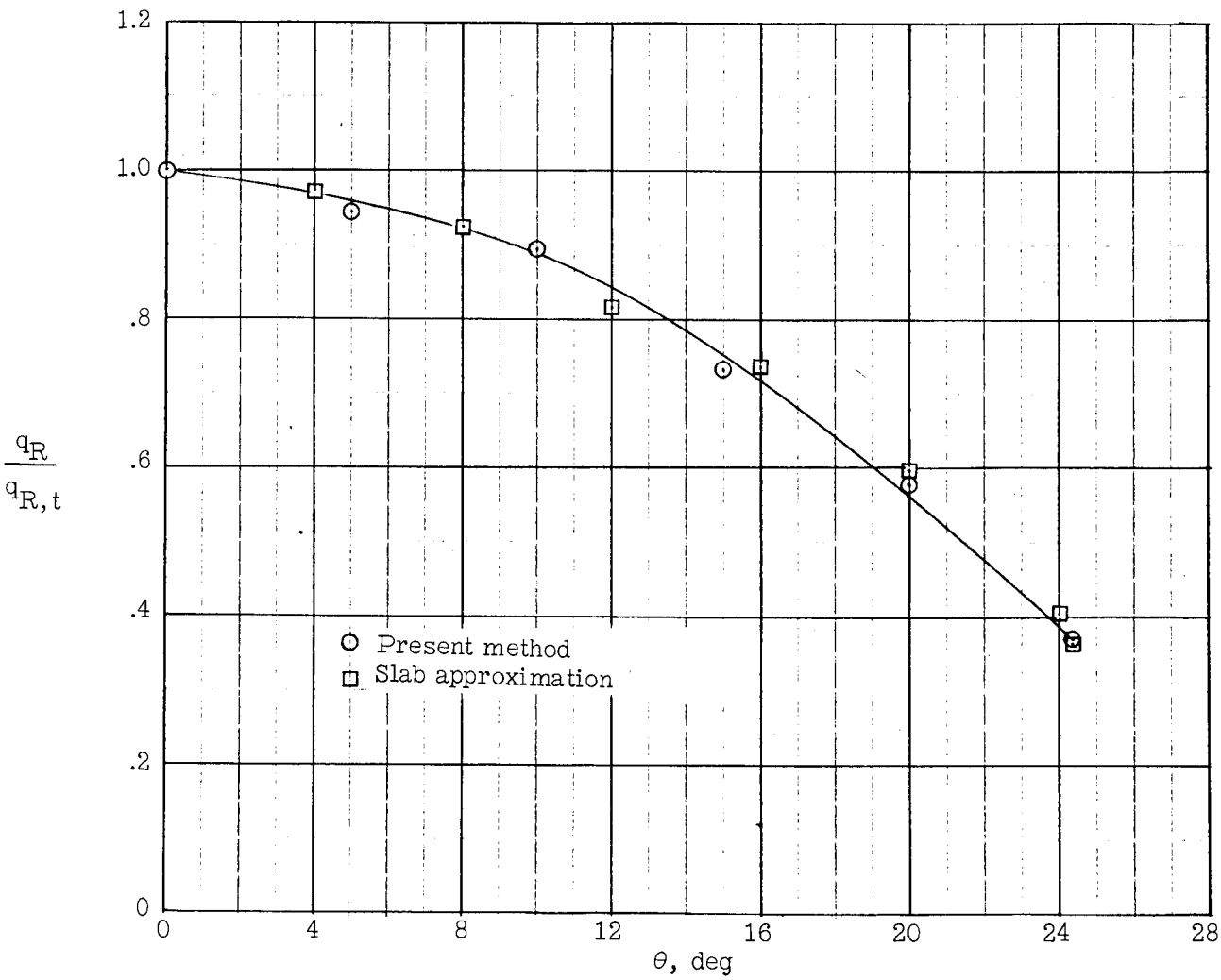

(e) t = 32 sec; $\bar{h}$ = 120,000 ft; U_∞ = 19,500 ft/sec.

Figure 13.- Concluded.

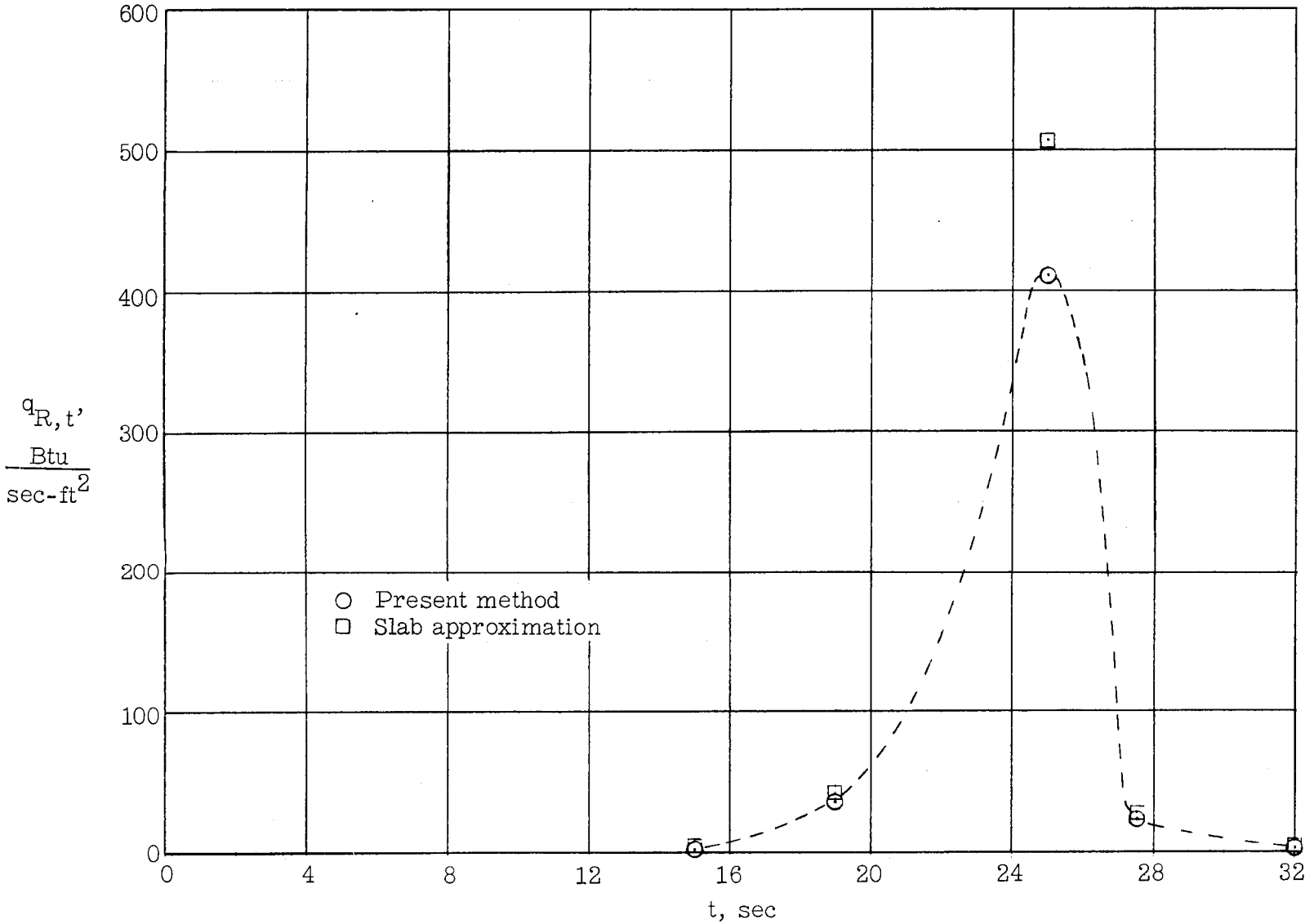

Figure 14.- Radiation heat transfer to stagnation point.

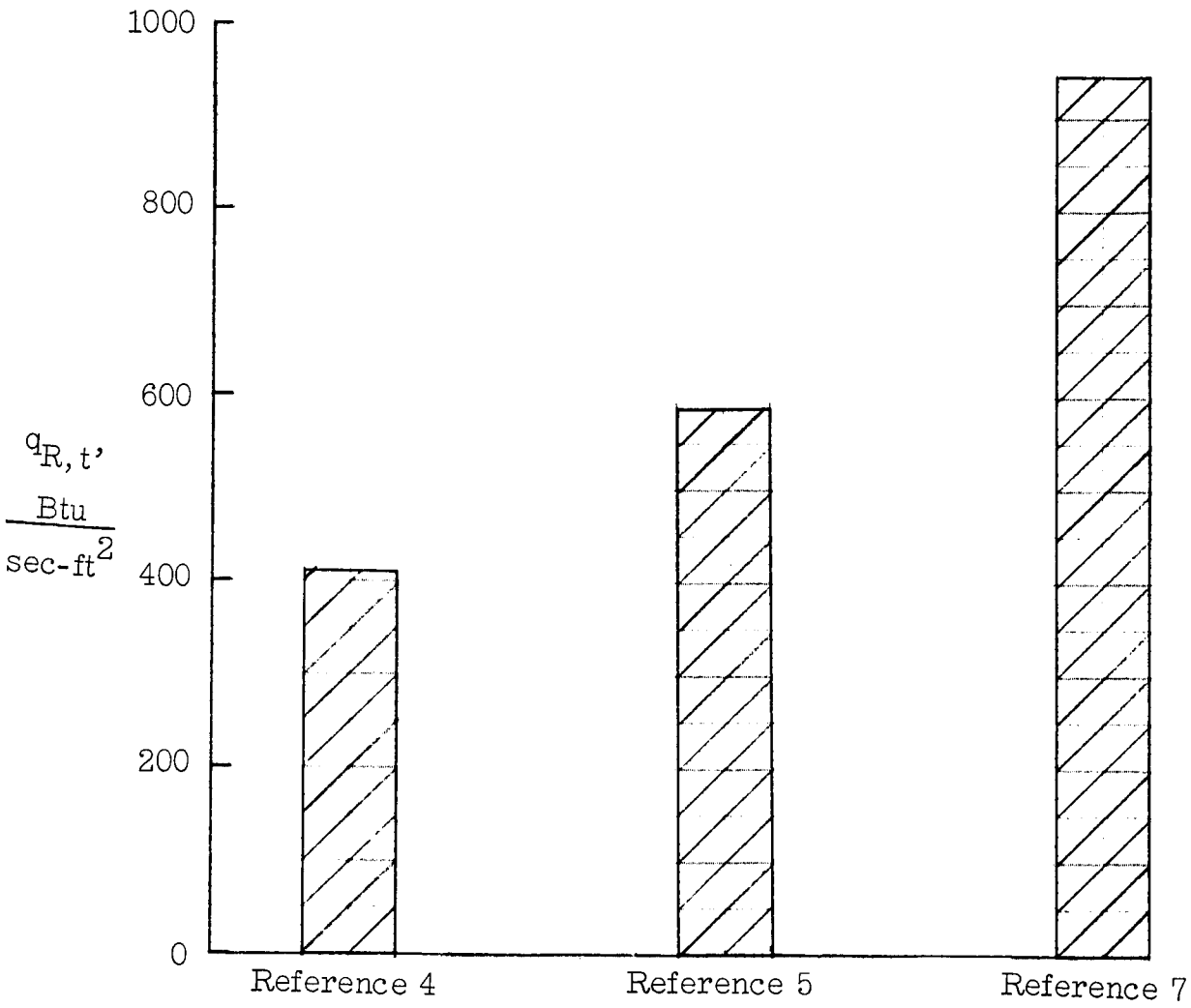

(a) Stagnation-point value.

Figure 15.- Comparison of radiation heating using various values for specific intensity. t = 25 sec; $\bar{h}$ = 166,000 ft; U_∞ = 34,800 ft/sec.

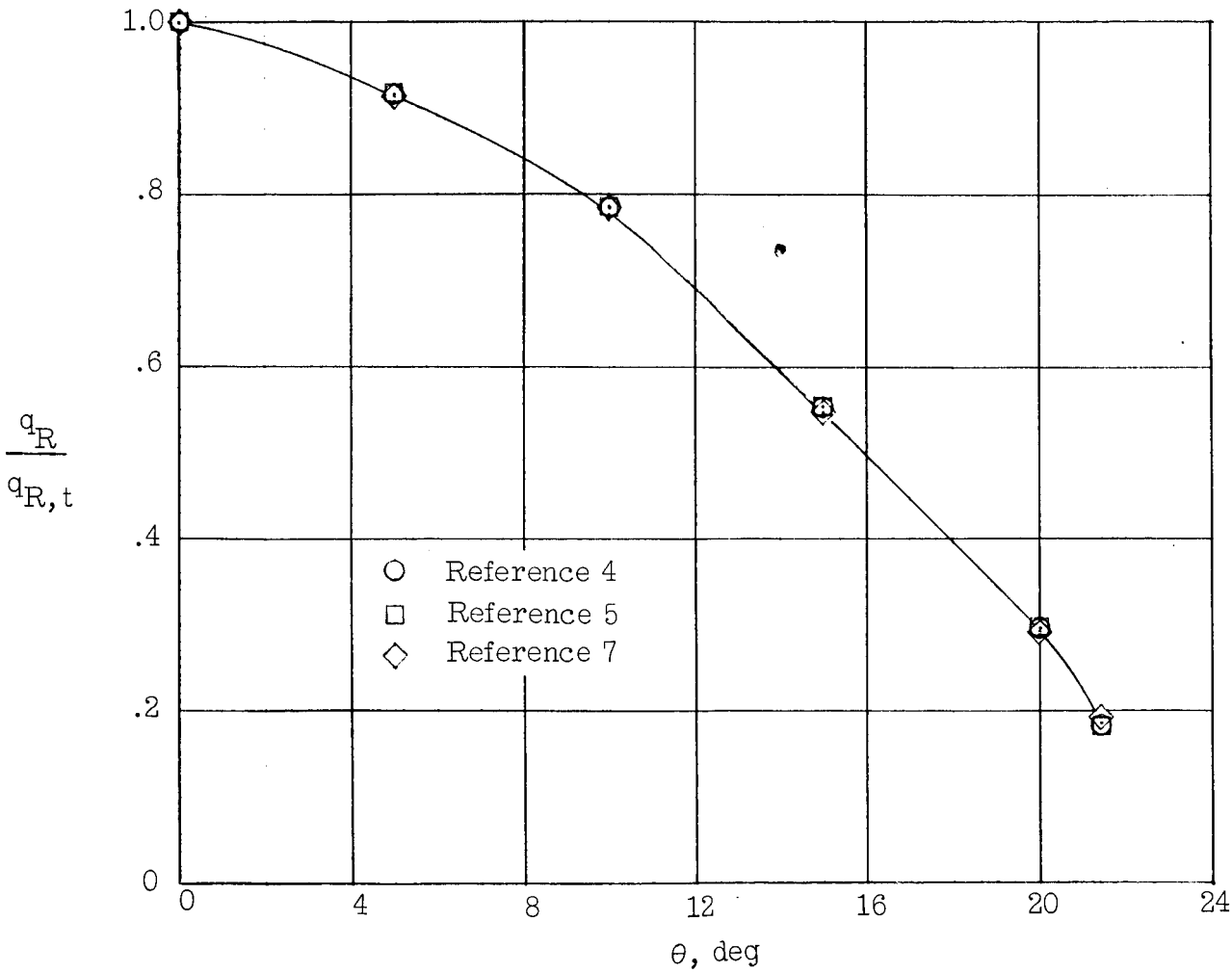

(b) Heat-transfer distribution.

Figure 15.- Concluded.

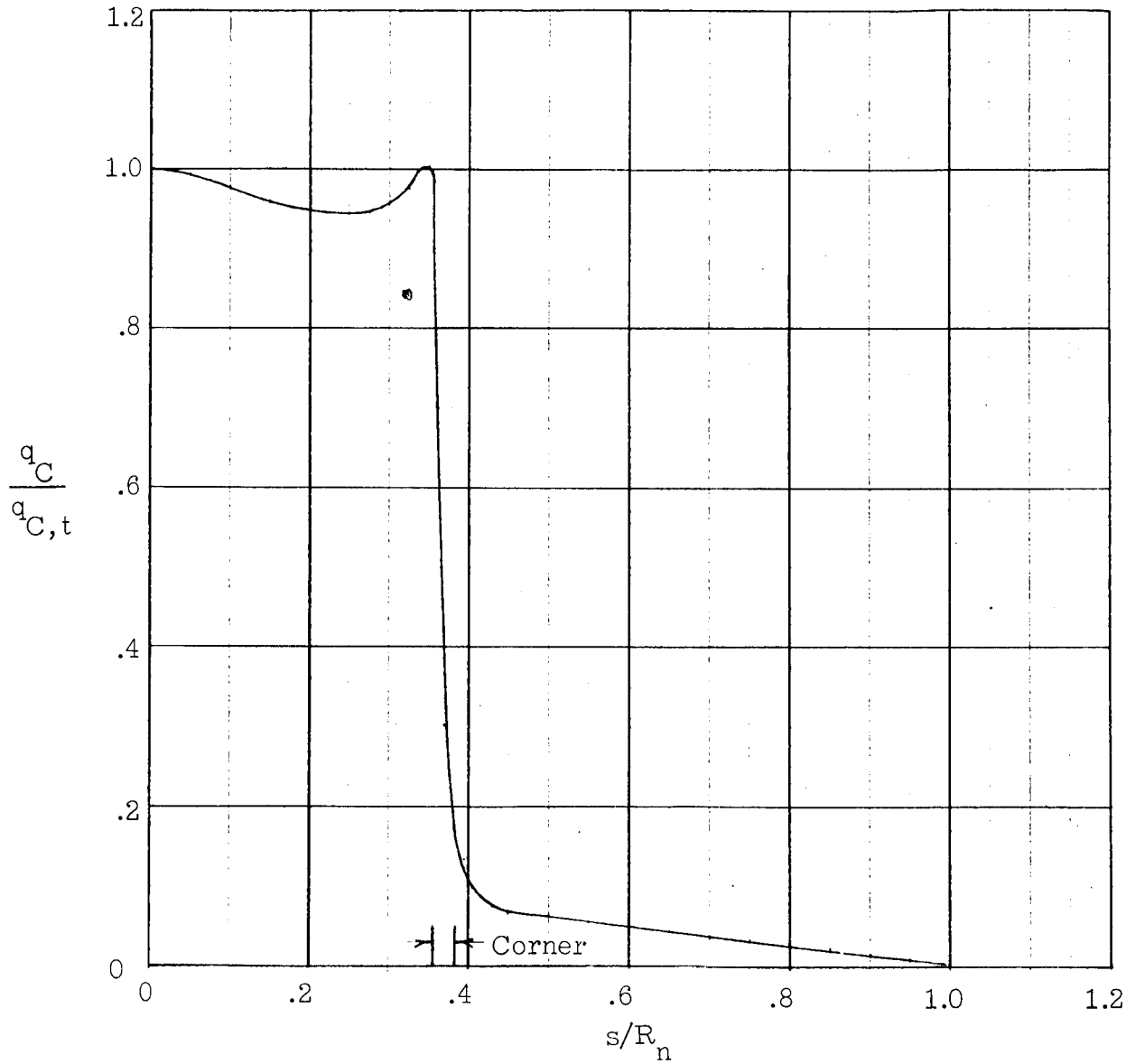

(a) $t = 15$ sec; $\bar{h} = 260,460$ ft; $U_\infty = 37,058$ ft/sec.

Figure 16.- Convective heat-transfer distribution.

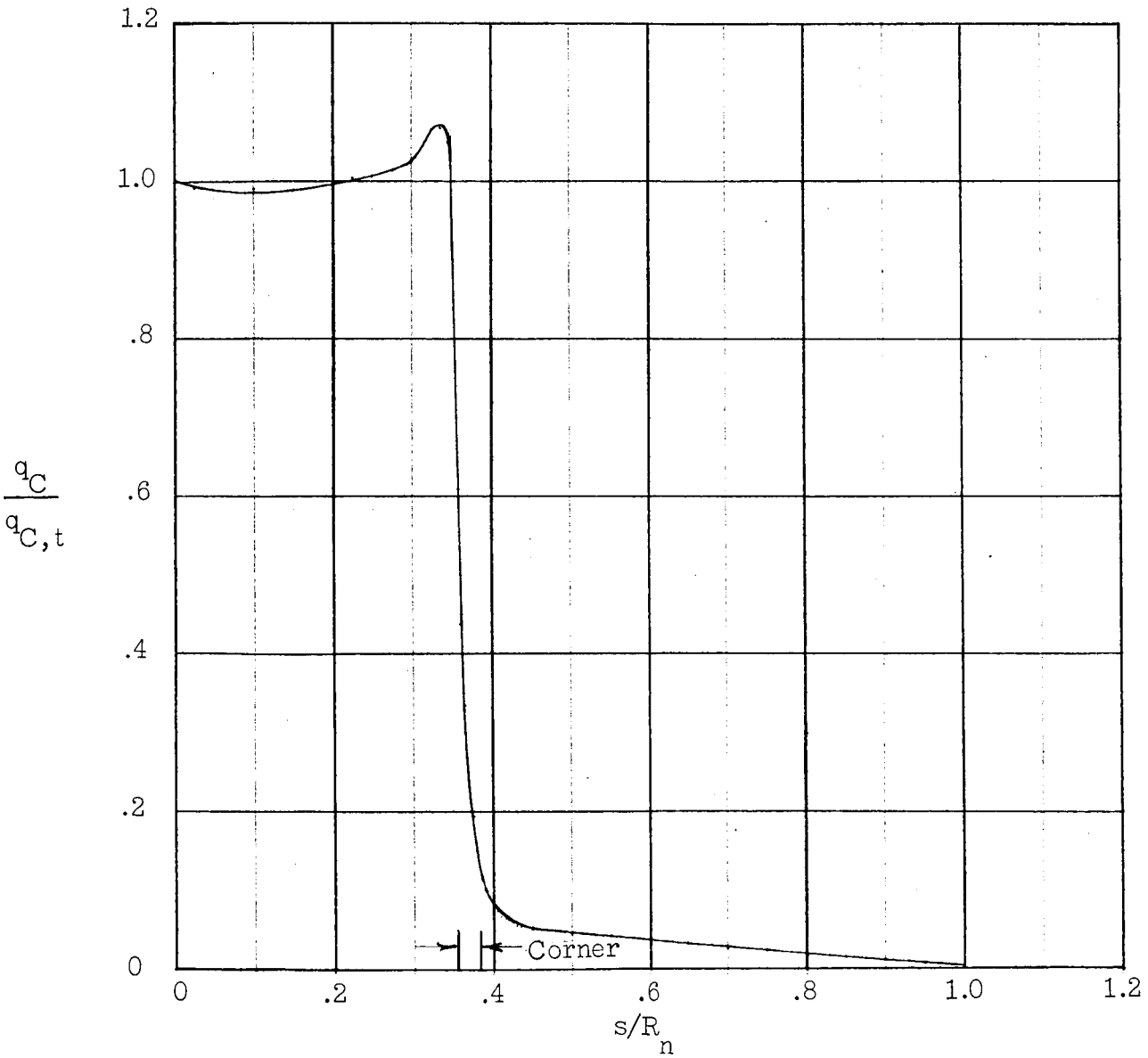

(b) $t = 19$ sec; $\bar{h} = 218{,}000$ ft; $U_\infty = 36{,}700$ ft/sec.

Figure 16.- Continued.

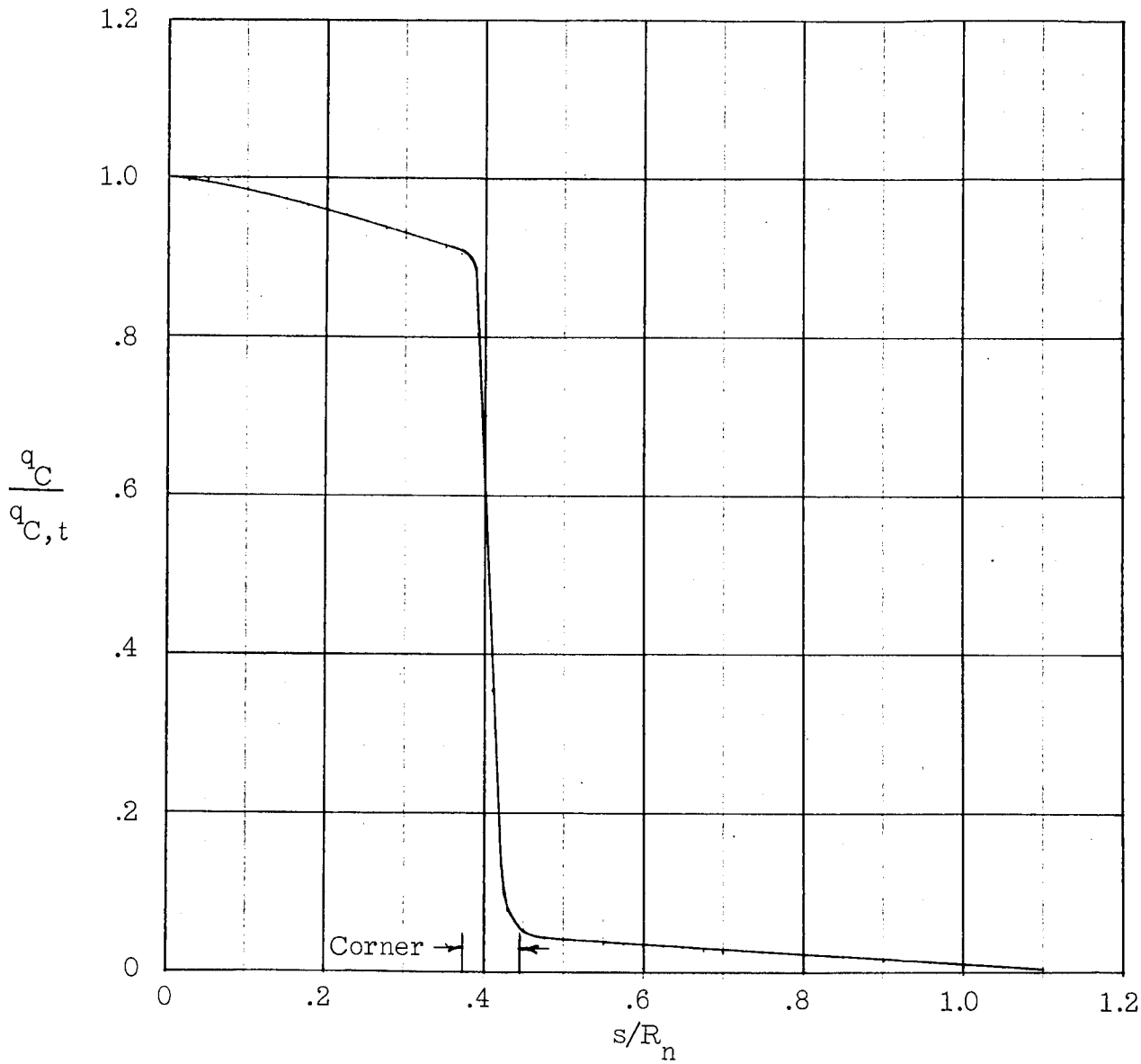

(c) t = 25 sec; $\bar{h}$ = 166,000 ft; U_∞ = 34,800 ft/sec.

Figure 16.- Continued.

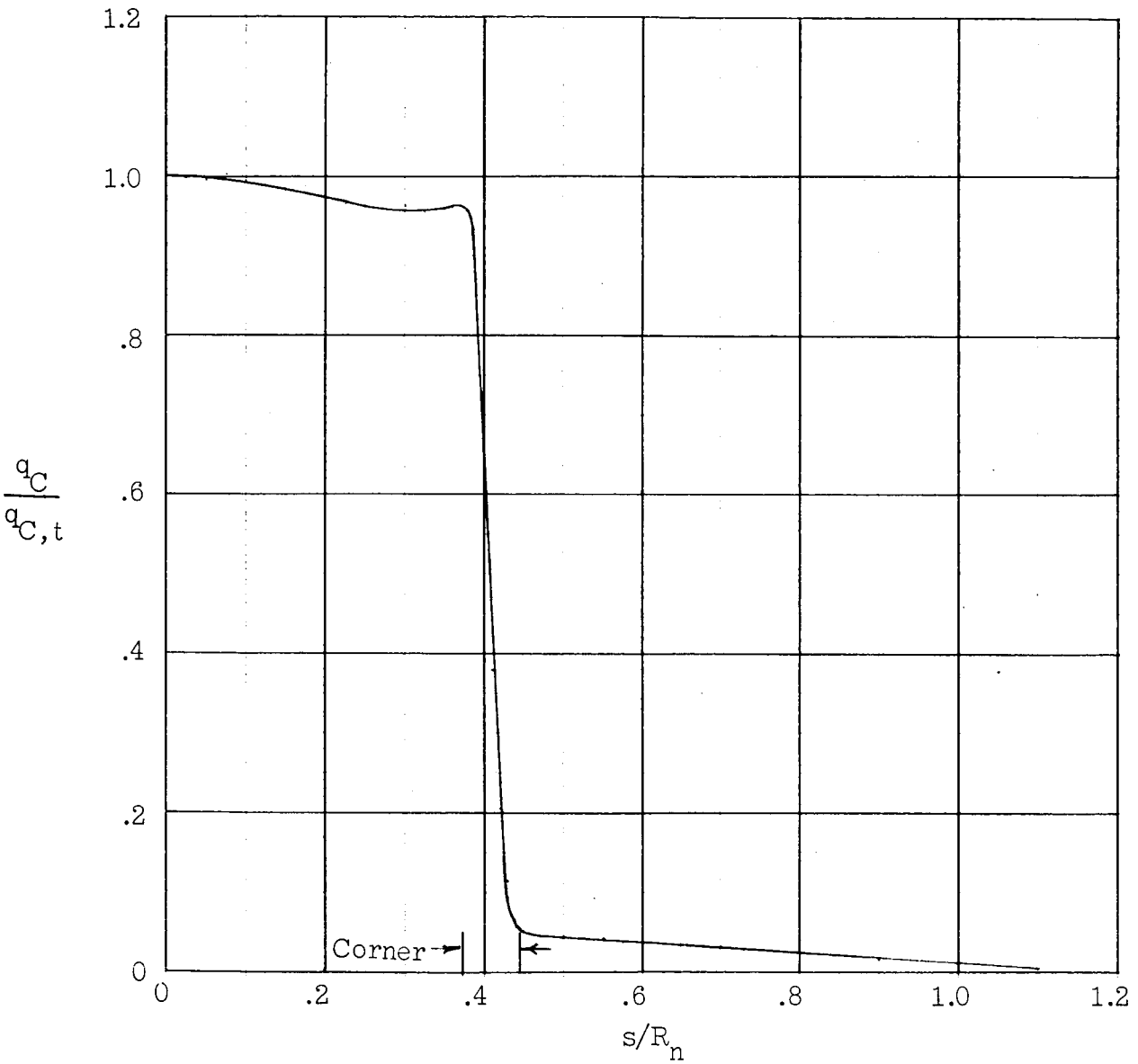

(d) t = 27.6 sec; $\bar{h}$ = 147,000 ft; U_∞ = 31,100 ft/sec.

Figure 16.- Continued.

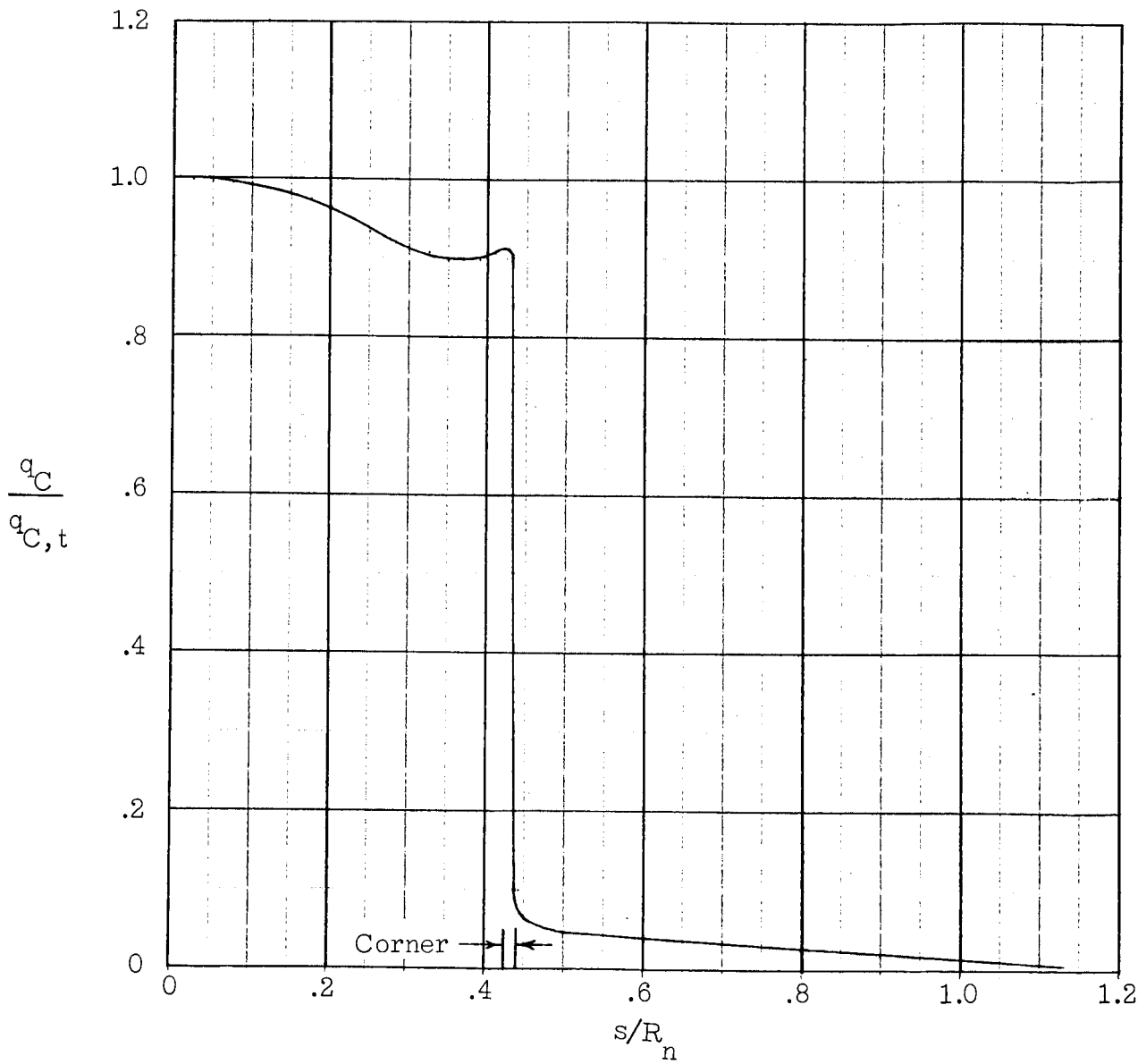

(e) t = 32 sec; $\bar{h}$ = 120,000 ft; U_∞ = 19,500 ft/sec.

Figure 16.- Concluded.

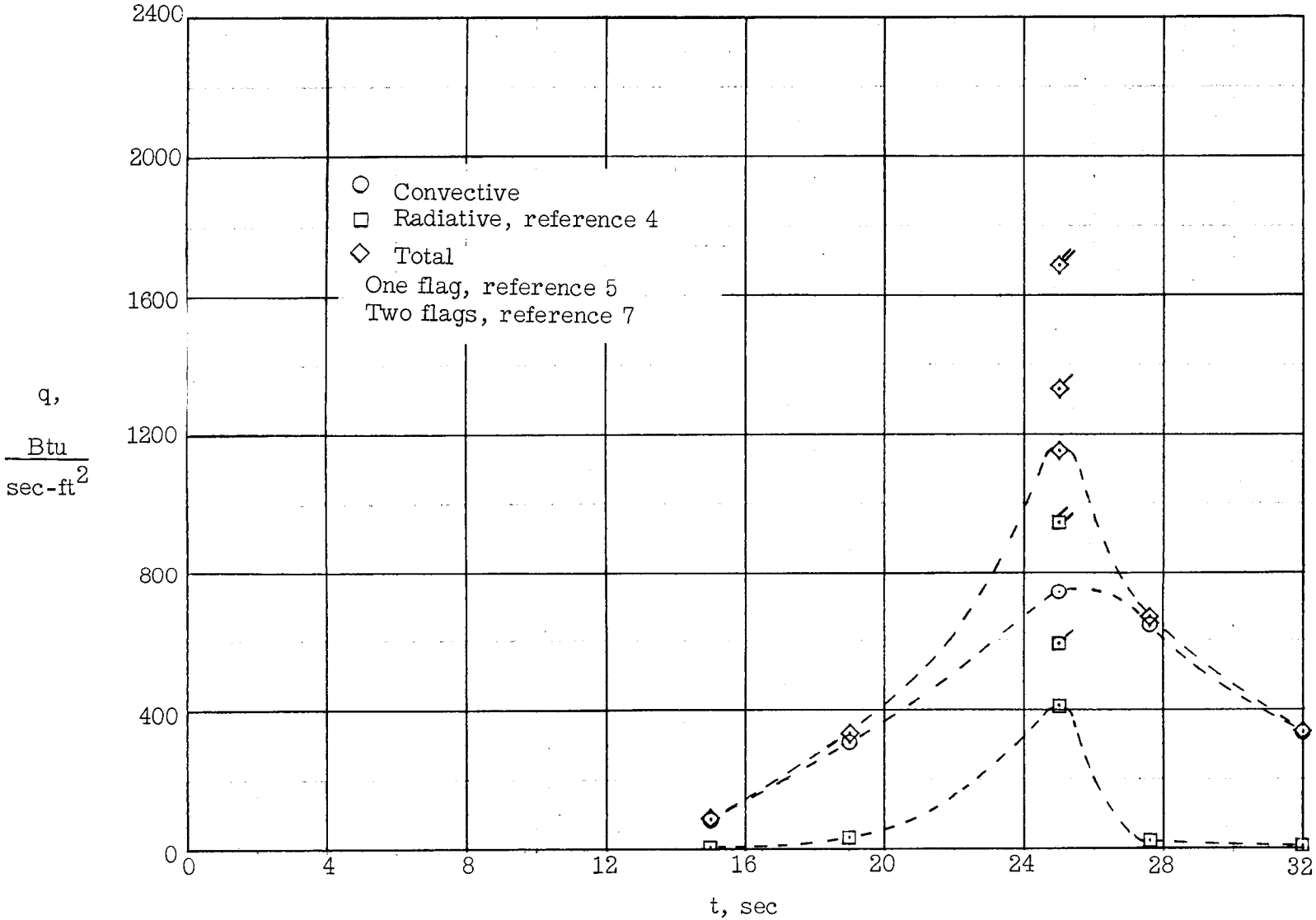

Figure 17.- Total heat-transfer rate to stagnation point.

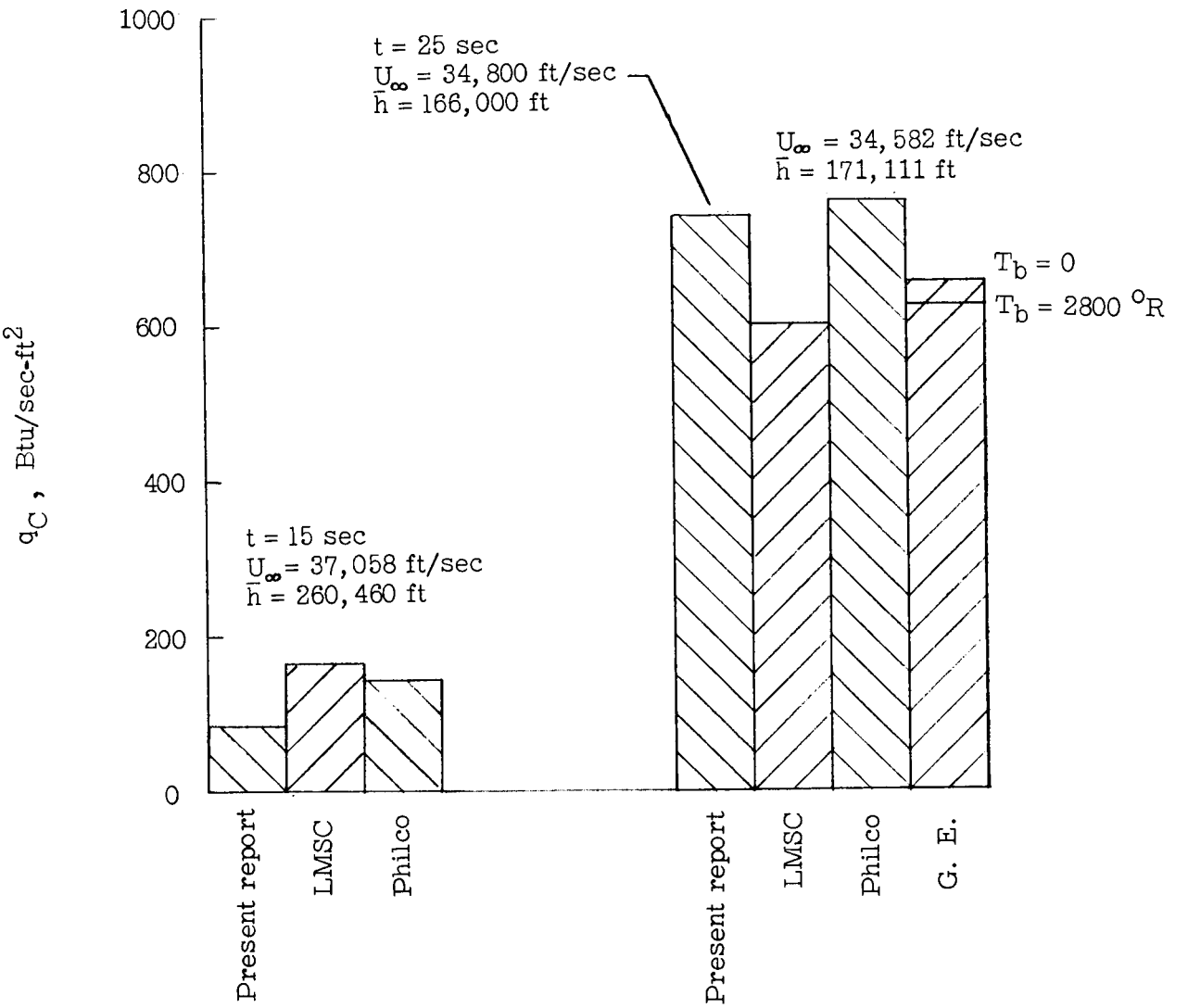

(a) Stagnation-point convective heating rate.

Figure 18.- Comparison between heating rates and heating distributions.

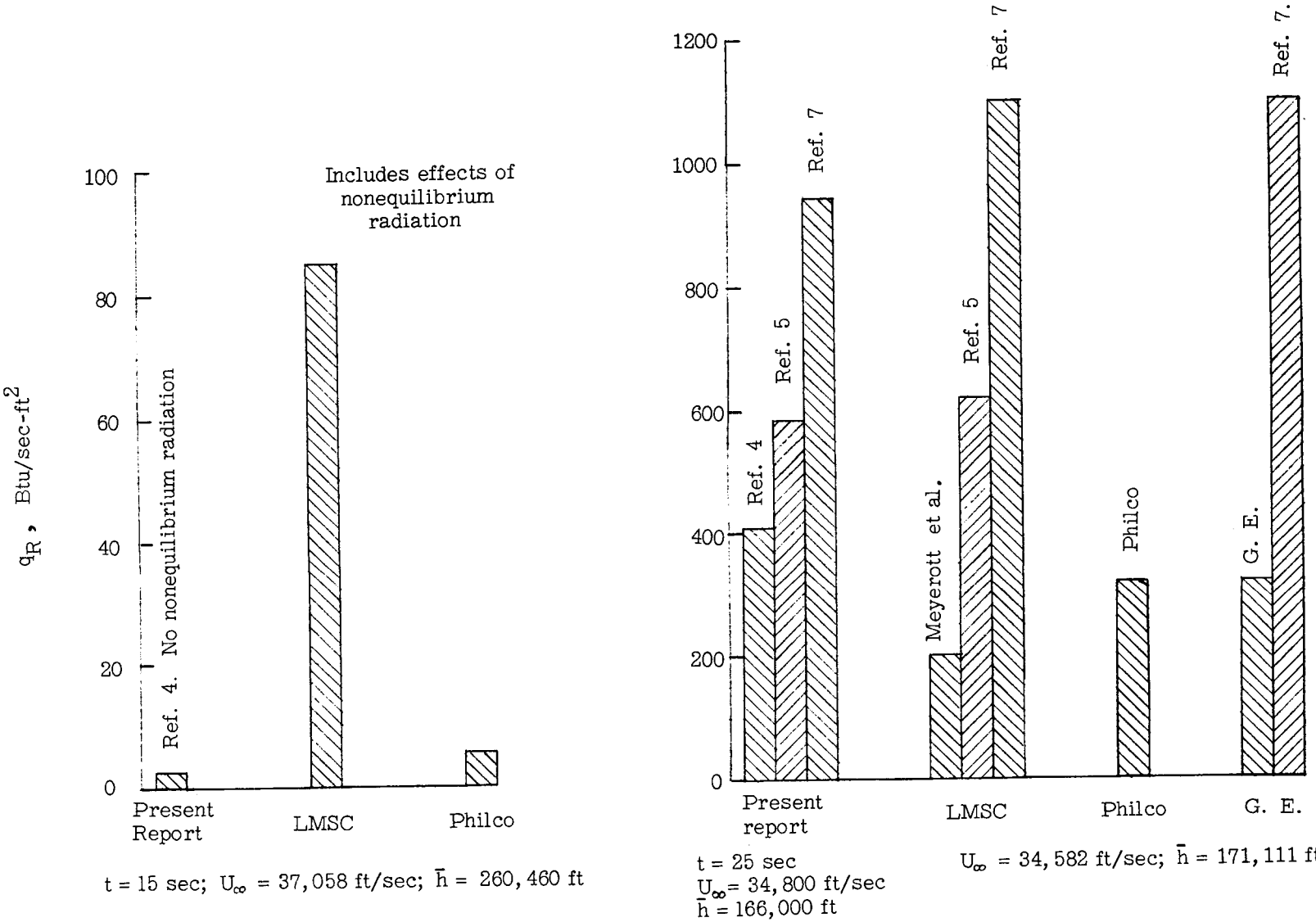

(b) Stagnation-point radiative heating rate.

Figure 18.- Continued.

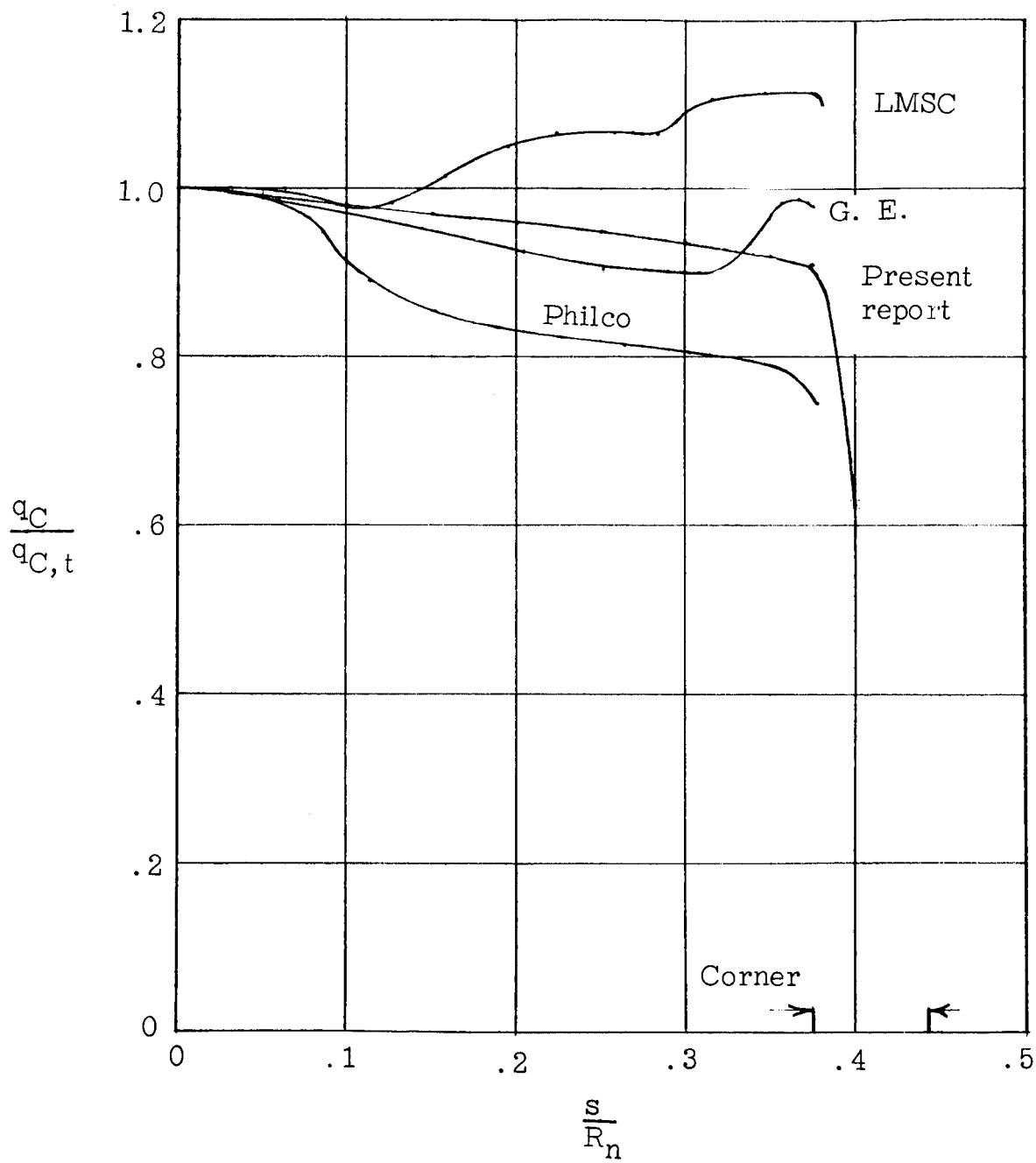

(c) Convective heat-transfer distribution.

Figure 18.- Continued.

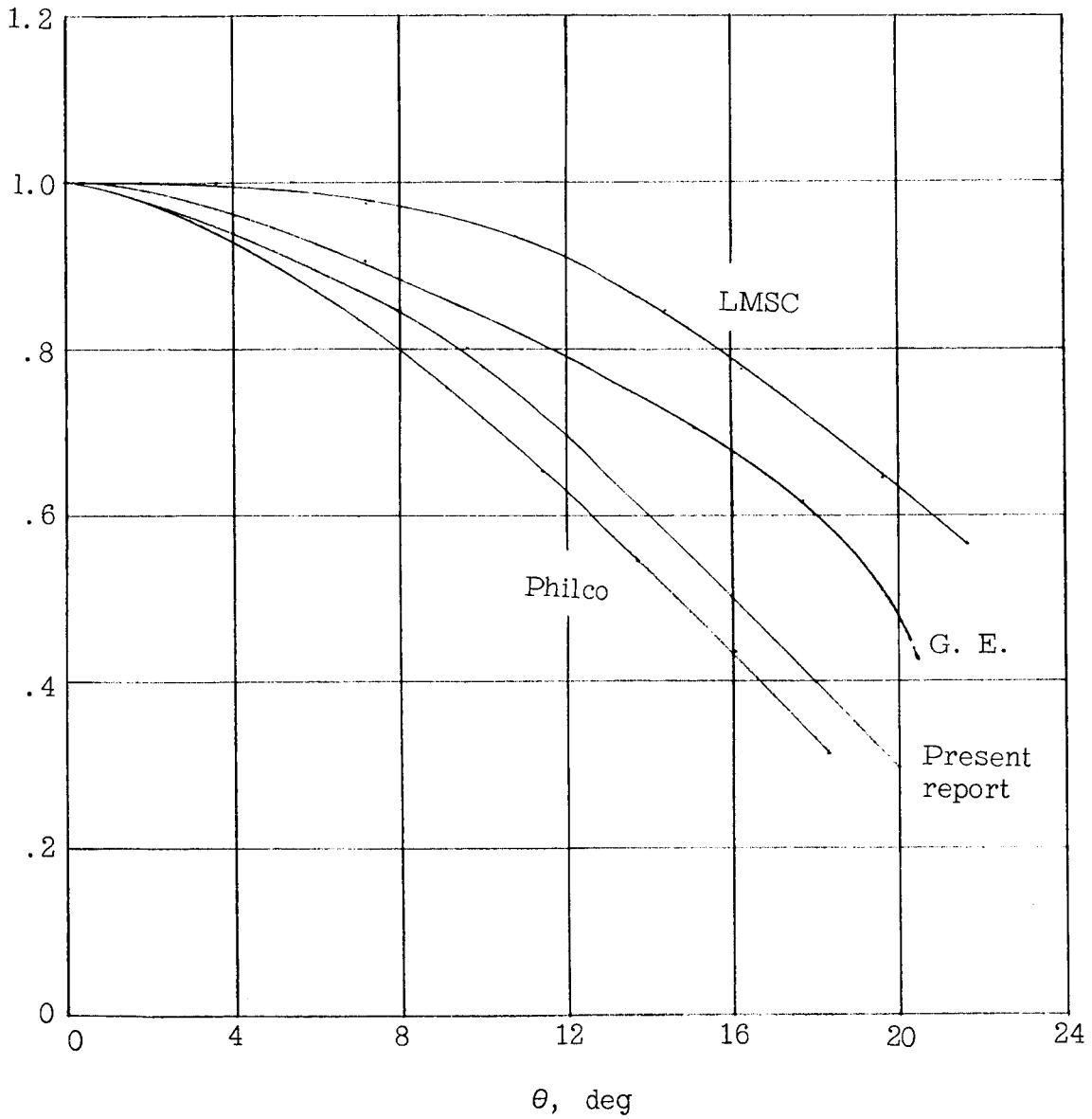

(d) Radiative heat-transfer distribution.

Figure 18.- Concluded.

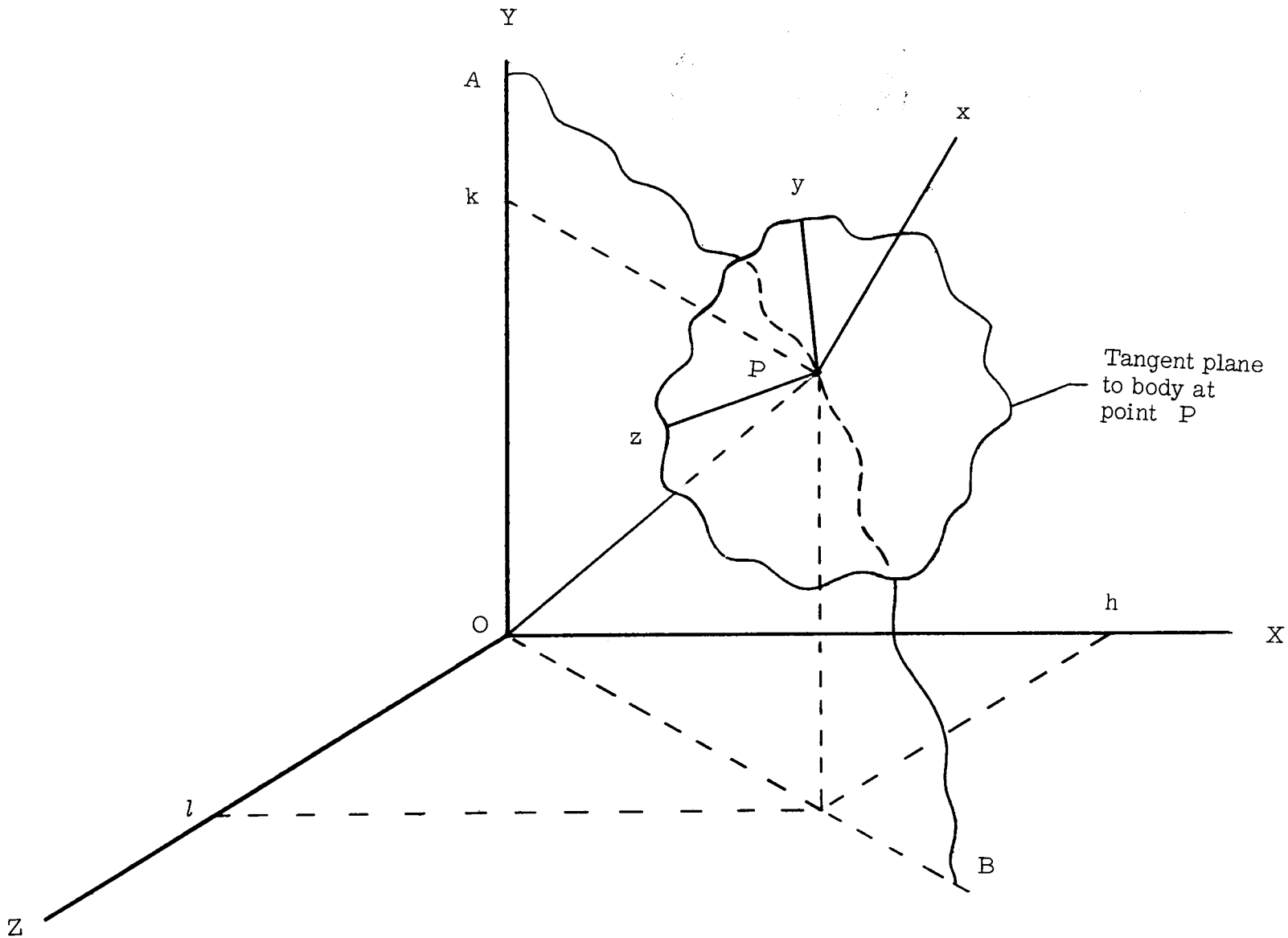

Figure 19.- Geometry of coordinate system.